

**Anisotropic behaviour of magneto-electric  
coupling in multiferroic composites**

**by**

**Steven Bourn**

A thesis submitted in partial fulfilment for the requirements for the degree of  
Doctor of Philosophy at the University of Central Lancashire

April 2018

# STUDENT DECLARATION FORM



**Type of Award**                      **Doctor of Philosophy**

**School**                                      **School of Physical Sciences & Computing**

**1.            Concurrent registration for two or more academic awards**

I declare that while registered as a candidate for the research degree, I have not been a registered candidate or enrolled student for another award of the University or other academic or professional institution

**2.            Material submitted for another award**

I declare that no material contained in the thesis has been used in any other submission for an academic award and is solely my own work

**3.            Collaboration**

I declare that this research programme was not part of a collaborative project.

**4.            Use of a Proof-reader**

No proof-reading service was used in the compilation of this thesis.

**Signature of Candidate** \_\_\_\_\_

**Print name:** \_\_\_\_\_

## Abstract

The anisotropy of the direct magnetoelectric effect in textured nickel ferrite/lead zirconate titanate strain mediated bilayer composites has been studied. The magnetic layers of these samples have been crystallographically textured in planes of the form {100}, {110} and {111}.

In this study, it is shown that the optimum bias field and the maximum magnetoelectric coupling signal can be controlled by changing the alignment of the applied magnetic field with respect to the magnetocrystalline anisotropy directions. It is also shown that the product of the optimum bias field and the maximum magnetoelectric coupling signal are proportional to the theoretical saturation magnetostriction.

The samples have been magnetically characterised using a recommissioned and developed biaxial vibrating sample magnetometer, capable of detecting the component of a sample's magnetic moment in 2 perpendicular directions and thus determining the net magnetic moment vector of the sample. Coupled with sample rotation this allows insight into the magnetic anisotropy of the sample, which has been compared with a micromagnetic model.

A specialist magnetoelectric coupling rig has also been developed to allow application of DC and AC magnetic fields to a sample simultaneously.

As part of the magnetic anisotropy study, a modified torque magnetometry method has been developed to enhance the identification of the anisotropy directions in magnetically soft samples, as well as a method by which torque

magnetometry can be approximated using the in-field direction component of magnetisation as measured using a standard vibrating sample magnetometer.

# Contents

1. Introduction .....	1
1.1. Nickel Ferrite .....	3
1.2. Magnetic Anisotropy in Nickel Ferrite.....	4
1.3. Magnetostriction of Nickel Ferrite .....	6
1.3.1. NFO_100.....	11
1.3.2. NFO_110.....	12
1.3.3. NFO_111.....	13
1.4. Piezoelectricity.....	14
1.5. Multiferroic composites and the magnetoelectric effect.....	16
1.6. Sample Details.....	20
1.7. Structure of this Thesis.....	21
2. Development of magnetic and magnetoelectric measurement devices and methods.....	24
2.1. Vibrating Sample Magnetometry .....	25
2.2. Sensitivity Profiles of the bi-axial VSM .....	27
2.2.1. Theoretical .....	27
2.2.2. Experimental.....	29
2.3. Precession and its reduction by modification to the UCLan VSM .....	33
2.3.1. Precession reduction methodology.....	33
2.4. Experimental Control .....	36

2.5.	Measurement Techniques .....	38
2.5.1.	The Magnetic Hysteresis (M-H) loop .....	39
2.5.2.	Easy Axis Distribution Measurements .....	40
2.5.3.	Torque Magnetometry using a Vibrating Sample Magnetometer ..	42
2.6.	Development of a Magnetolectric Measurement Device .....	45
2.6.1.	Requirements/Construction .....	45
2.6.2.	ME Coupling Measurements .....	48
3.	Development of An Alternate Method of Simulating Torque Curves Using A Standard VSM.....	52
3.1.	In-field Methodology Development .....	56
3.2.	Testing of the Methodology Using In-Field Rotation Curves .....	58
4.	Micromagnetic Modelling .....	66
4.1.	Magnetic Moment from Angular Momentum.....	66
4.2.	Bohr Magneton and Gyromagnetic Ratio.....	66
4.3.	Magnetic Moment of an Isolated Electron.....	68
4.4.	Precession and Continuum Magnetisation.....	68
4.5.	Landau-Lifshitz Equation.....	70
4.6.	Landau-Lifshitz-Gilbert Equation .....	71
4.7.	Effective Field Contributions .....	73
4.7.1.	Magnetostatic Term.....	73
4.7.2.	Direct Exchange .....	74

4.7.3.	Magnetocrystalline Anisotropy.....	75
4.7.4.	The Magnetoelastic Effect.....	78
4.8.	Micromagnetic Modelling Software – Boris.....	79
4.9.	Hysteresis loop showing bulk NFO is magnetically hard .....	83
4.10.	Torque Magnetometry.....	85
5.	Anisotropy measurements of the Magnetoelectric effect in NiFe <sub>2</sub> O <sub>4</sub> /PbZrTiO <sub>3</sub> bilayers.....	88
5.1.	Magnetic Characterisation of Nickel Ferrite samples.....	89
5.2.	Determination of the Magneto-Electric coupling as a function of sample rotation.....	90
5.3.	The Effects of Magnetostriction.....	95
5.4.	The Effect of Varying applied AC Field.....	106
6.	Conclusions.....	110
	Appendix A.....	126
	Publication .....	129

## List Of Figures and Tables

Figure 1 - Crystal structure of nickel ferrite showing the tetrahedral A sites ( $T_d$ ) and the octahedral B sites ( $O_d$ ).....	4
Figure 2 - Showing the Anisotropy axis directions for the NFO_100, NFO_110 and NFO_111 discs. With black for hard axes, red for medium and blue for easy. In the case of the NFO_111 disc, the anisotropy energy is approximately that of a medium axis but is present in all directions. (i.e isotropic).....	6
Figure 3 - Spherical polar coordinates .....	8
Figure 4 - Showing the directions in which the crystal axes occur in the NFO samples. In the (a) the relation ship between the crystal axes and the crystallographic directions is demonstrated. (b), (c) and (d) represent the planes of the NFO_100, NFO_110 and NFO_111 samples respectively. It is important to note that the angles between the crystal axes and the plane in the NFO_111 case are equal for all three crystal axes. ....	10
Figure 5 - Saturation magnetostriction as a function of sample rotation for discs cut in $\{100\}$ , $\{110\}$ and $\{111\}$ . Note that the magnetostriction is presented negated so that it is in terms of contraction rather than extension.....	12
Figure 6 - Schematic representation of piezoelectricity in a material with spontaneous polarisation (A) without stress and (B) under strain. The white and black circles represent negatively and positively charged ions respectively. ....	15
Figure 7 - Schematic of a hysteresis loop for Ferromagnetic or Ferroelectric materials .....	16
Figure 8 - Schematic of the ME effect where H is the applied magnetic field, E applied electric field, M is magnetisation and P is the polarisation. The thick down arrows represent the direct effect of an applied stimulus and the thin diagonal lines represent the induced ME effects.....	17
Figure 9 - Schematic of NFO/PZT bilayers, showing how the electrical contacts are connected to either side of the PZT layer. ....	20
Figure 10 - X-Ray Diffraction spectra for the NFO_100, NFO_110 and NFO_111 samples.....	21
Figure 11 - Schematic representation of a standard VSM .....	26
Figure 12 - Coil configuration of the biaxial VSM at UCLan .....	27
Figure 13 - Coil Dimensions of a single coil. The position <b>P</b> defines the coordinate system used when considering the response to a sample at that point.....	28

Figure 14 - Comparison of Nickel dot, Iron Oxide and theory to demonstrate minimal convolution effects.....	30
Figure 15 - Normalised Response curves for Parallel (a-c) and Transverse coils (d-f), with the measured curves (a & d), Theoretical (b & e) and a comparison on a single cross section (c & f) for each set.....	31
Figure 16 - Simple two coil system showing coil axis orientated in parallel-to-field direction.....	32
Figure 17 - Schematic demonstration of the method for reducing the precession of the sample during rotation. (a) Ideal arrangement, zero precession. (b) Misaligned sample with respect to the rotation axes, large precession. (c) Sample shifted into alignment with rotational axes, minimised precession.....	34
Figure 18 - Schematic showing the vibrator head assembly, (a) before modifications where made, and (b) after the x-y stage has been fitted to allow for precession reduction.....	35
Figure 19 - Magnitude of the moment vector as a VHS tape sample is rotated. Showing reduced precessional effects. ....	36
Figure 20 - Front Panel of the hysteresis routine developed in LABview. This is the main user-interface used for hysteresis measurements. ....	37
Figure 21 - A typical hysteresis loop for a hard sample, denoting saturation magnetisation, $M_s$ , remanent magnetisation $M_r$ and the coercivity $H_c$ .....	39
Figure 22 - Easy axis distribution measurement on a uniaxial VHS sample. ....	42
Figure 23 - The geometry of the biaxial measurement.....	43
Figure 24 - Torques, $L_a$ , (due to an in-plane applied field $H_a$ ) and $L_k$ (due to the anisotropy field $H_k$ ) acting on the magnetization vector $M$ . As each torque is equal and opposite, the magnetization is in an equilibrium position.....	44
Figure 25 - Showing how $M \perp$ reduces at high fields.....	45
Figure 26 - DC field as a function of input voltage for the 4" Newport magnet ..	46
Figure 27 - Schematic of the ME rig showing the sample position, contact wires for measuring the piezoelectric response and the Helmholtz coils for producing the small ac magnetic field.....	47
Figure 28 - AC Field as function of input amplitude for the helmholtz coils.....	48
Figure 29 - Typical ME response as a function of applied DC magnetic field .....	49
Figure 30 - Typical ME Coupling signal as a function of applied AC field.....	50
Figure 31 - Torque curves derived from the transverse magnetisation of the NFO_100 sample. The sample is originally saturated before the field is reduced to	

the required value. A measurement of the moment is made every 4°. The intercepts with the abscissa with positive and negative gradients indicate the hard and medium axes of the sample, respectively. Each axis is separated from the previous by approximately 45° as expected from the theory. The field was decreased by 100 Oe between each measurement. ....54

Figure 32 - Geometry of biaxial measurements, showing sample rotation angle  $\theta$ , and the magnetisation angle  $\phi$ .....56

Figure 33 - **(a)** A schematic switching field distribution (SFD). When an applied field ( $H_a$ ) is applied any moment with a switching field less than  $H_a$  (shown as the shaded area) is considered “switched” and those with a greater switching field are considered “un-switched.” **(b)** How the switched and un-switched components interact with the field as the sample is rotated. The unswitched components rotate with the sample whilst the switched components remain in the direction of the applied field.....57

Figure 34 - Torque curves derived from the in-plane magnetisation of the NFO\_100 showing good agreement with the bi-axial method of Figure 29 for the position of the intercepts with the abscissa. This gives confidence in the new method as a means of identifying the anisotropy axes of a material. Note the loss of definition at small fields.....59

Figure 35 - In-field magnetisation as a function of sample rotation for the NFO\_110 sample. The sample is initially saturated before the field is reduced to the required value. The turning points are labelled E for easy axis, M for medium axis and H for hard axis.....60

Figure 36 - Schematic representation of the M-H loops measured when the field is aligned along an easy (blue) and hard (black) axis. When the sample is rotated from an easy to a hard axis at a fixed field lower than saturation ( $H_a$ ) the magnetisation will change from  $M_e$  to  $M_h$ . This gives rise to the peaks and troughs in Figure 35.....61

Figure 37 - Comparison of the in-field method (data points, which refer to the left axis) with the bi-axial VSM (Lines, which refer to the right axis) for the NFO\_110 sample. The good agreement of the intercepts with the abscissa and the relative amplitude of the peaks gives confidence in the applicability of the new method. The different symbols and line types represent measurements being taken at different applied field values, ranging from 0.25 kOe to 0.5 kOe. ....62

Figure 38 - Torque measurements on the NFO\_111 sample using (a) conventional transverse method and (b) the newly developed in-field method note the curve closest to the “sweet spot” is shown .....64

Figure 39 - Precession of the magnetic moment  $\mu$  around the magnetic field  $B$ 68

Figure 40 - (a) loss-less precession of magnetisation around a magnetic field. (b) damped precession around a magnetic field, showing damping torque ( $L_{damp}$ ) direction. ....70

Figure 41 - Schematic of the in-plane uniaxial anisotropy energy, with the easy and hard axes highlighted .....	76
Figure 42 - Schematic representation of the cubic anisotropy energy in the x-y plane, showing the biaxial nature of this plane. The Easy and Hard axes marked are for this plane.....	78
Figure 43 - Boris micromagnetic package during a hysteresis simulation on a NFO_110 disc. The command line is shown top-left with a real-time display of the magnetisation bottom-right. ....	79
Table 1 - Symmetry direction polar and azimuthal angles for NFO samples.....	82
Figure 44 - Modelled Hysteresis curve for NFO_110 sample .....	83
Figure 45- Saturation (a) and Remanent (b) states in a simulated polycrystalline sample. The colour indicates the direction of magnetisation, with blue being left-aligned and red being right-aligned. In the saturated state the majority of grains are aligned in a single direction. When the field is removed the magnetisation of some grains rotates to be antiparallel with their neighbours due to long-range demagnetising effects. ....	84
Figure 46 - Magnetocrystalline Anisotropy Energy of the three simulated NFO discs .....	86
Figure 47 - Positive-field hysteresis loops along the three principle axes in the NFO_110 sample. The inset is a full field hysteresis loop of an easy direction in the same sample. In all cases $H_c = 10 Oe$ .....	89
Figure 48 - Magneto-Electric coupling signal as a function of applied DC field in the NFO_110 sample for the three principal crystallographic directions. ....	91
Figure 49 - Peak ME coupling as a function of sample rotation for the NFO_110 sample.....	93
Figure 50 - Peak ME coupling as a function of sample rotation for the NFO_110 sample. with an ac field of 4 Oe.....	94
Figure 51 - Polar plots of the Peak DC field (a) and Peak ME coupling signal (b) for NFO_110.....	95
Figure 52 - Schematic representation of magnetostriction as a function of applied magnetic field.....	96
Figure 53 - Schematic showing the derivative of the function in Figure 8. Of particular importance are the peak field $H_{peak}$ and the peak height $d\lambda dh_{peak}$ . ....	98
Figure 54 - The product of the DC ME peak height and field for thje NFO_110 sample for both positive and negative fields. The theoretical line is fit to the positive field curve.....	101

Figure 55 - Results for the NFO\_100 sample as a function of sample rotation:(a) The Optimum dc bias field, (b) the peak ME coupling signal and (c) The product of the DC ME peak height and field for the NFO\_100 sample for both positive and negative fields. The theoretical line is fit to the positive field curve. .... 102

Figure 56 - Results for the NFO\_111 sample as a function of sample rotation:(a) The Optimum dc bias field, (b) the peak ME coupling signal and (c) The product of the DC ME peak height and field for the NFO\_100 sample for both positive and negative fields. The theoretical line is fit to the positive field curve. .... 103

Figure 57 - Magnetoelectric coupling as a function of applied AC field for the principal axes in the NFO\_110 sample ..... 107

Figure 58 - ME coefficient as a function of angle for the NFO\_110 sample..... 108

Figure 59 - ME Coefficient as a function of angle for the NFO\_100 (a) and NFO\_111 (b) samples..... 108

## Acknowledgements

As with all things, it would be remiss to call this project a solitary effort. To do so would be a grave insult to all those who, intentionally or not, kept the project and the author running smoothly.

Principal amongst these must stand my (nearly) tireless supervisory team, Tim Mercer, Phil Bissell and Serban Lepadatu. Without whom I would certainly never have reached this point. Tim and Phil's knowledge of the arcane world that is the UCLan magnetic materials research lab has saved days, weeks and perhaps even months of work that would have been spent re-inventing the wheel without them, and Serban's knowledge of the even more arcane world of micro-magnetic modelling without which this project would be sorely lacking.

My thanks go out to the rest of the JHI also, particularly my fellow postgraduate students, whether basement dwellers or those in the lofty heights, without whom the past years would have been an incredibly lonely time, albeit far more sane.

Special thanks to Melvin Vopson of the University of Portsmouth for providing the samples for this project.

I must also thank my family, particularly my "engineering consultants" Robert and Sean Bourn.

Finally many, many thanks to Kathryn Ashworth, probably the main reason I've avoided a straitjacket.

# 1. Introduction

Multiferroic materials exhibiting two or more ferroic order parameters, such as ferroelectricity, ferromagnetism and ferroelasticity, have the potential for application in multifunctional devices ranging from magnetic random access memory (MRAM) through to sensors and energy harvesting [1-4]. Coupling between ferroic orders increases the number of functionalities, such as the Magnetolectric (ME) effect where an applied magnetic field causes an electrical polarisation known as the *direct* ME effect, or an applied electric field induces magnetisation, the *converse* ME effect.

There are two main classes of magnetolectric materials, single-phase and multi-phase. Single-phase magnetolectric materials are chemically homogenous and isotropic compounds [5] however they have small ME responses described by the linear ME coefficient,  $\alpha$ , topping out at  $36.7 \text{ psm}^{-1}$  for  $\text{TbPO}_4$ . The largest ME responses are found in multiferroic composites, which consist of physically separated magnetic and electric phases [6], such as the early particulate  $\text{BaTiO}_3/\text{CoFe}_2\text{O}_4$  produced by van Suchtelen, van den Boomgard *et al*, which achieved ME voltage coefficients defined as  $dE/dH = \epsilon_0\epsilon\alpha$  of up to  $130 \text{ mV cm}^{-1} \text{ Oe}^{-1}$  corresponding to  $\alpha = 720 \text{ ps m}^{-1}$ . Some of the simplest multiferroic composites are created by mechanically bonding magnetostrictive and piezoelectric layers into a strain-mediated bilayer composite. These have ME voltage coefficients up to 36 times that of particulate composites [7] and are the subject of this study.

Multiferroics with crystallographically orientated magnetic layers have been used to enable and enhance voltage-induced magnetisation switching [8]; utilising the so-called *converse* ME effect. This effect has also been analysed theoretically [9] in a proposed magnetoresistive device. Some studies have also been done on the effects of texturing the piezoelectric layer [2] in which textured piezoelectrics show enhanced piezoelectric response that can be used to enhance the magnetoelectric coefficient of composites.

To date, the effects of orientation in the magnetic layer on the *direct* ME coupling have not received attention; with no literature found reporting the effect of texturing on the electrical response at different alignments within a magnetic field. This change with respect to the magnetic anisotropy forms the main part of the investigation reported here. In particular, polycrystalline and textured NiFe<sub>2</sub>O<sub>4</sub> (Nickel Ferrite or NFO) thick films bonded with PbZrTiO<sub>3</sub> (PZT) to form NFO/PZT bilayers are studied in this thesis. Full details of these samples are detailed later in this chapter. It is shown that the ME response may be tuned simply by changing the alignment of the magnetic field. This gives potential for a device to be optimised for direction specific applications such as energy harvesting from AC losses from cables. It may also provide a new technique that enables multiple ME responses within a single device to be realised by simple variation of the applied field direction.

In this chapter, the concepts of magnetostriction and piezoelectricity are introduced in the context of nickel ferrite and PZT respectively. We also consider in more detail the nature of multiferroic materials and explore some of the proposed applications for ME composites in particular.

## 1.1. Nickel Ferrite

The ferrites are double oxides of iron and another metal [10] and are the source of the term ferrimagnetism. Unlike ferromagnetic materials not all the uncompensated spins align parallel giving rise to a smaller total moment in ferrimagnets [11]. The ferrites are further divided into cubic and hexagonal forms. Nickel ferrite is a cubic ferrite and so has a crystal structure related to that of the mineral spinel,  $\text{MgO} \cdot \text{Al}_2\text{O}_3$  [12] which is shown in Figure 1 [13].

This spinel structure is complex with eight formula units, or 56 ions per unit cell. The 32 oxygen ions form a face-centered cubic arrangement and the metal ions fill gaps in-between. Two kinds of spaces are available for the metal ions: tetrahedral “A sites” surrounded by 4 oxygen ions and octahedral “B sites” neighboured by 6 oxygen ions. Not all of the available sites are occupied, with only 8 of 64 A sites and 16 of 32 B sites normally occupied. In ferrites, if the B sites are solely occupied by Fe ions it is called a “normal spinel” structure, while if the Fe ions are distributed evenly between A and B sites it is an “inverse spinel” structure. Nickel ferrite is of the latter form.

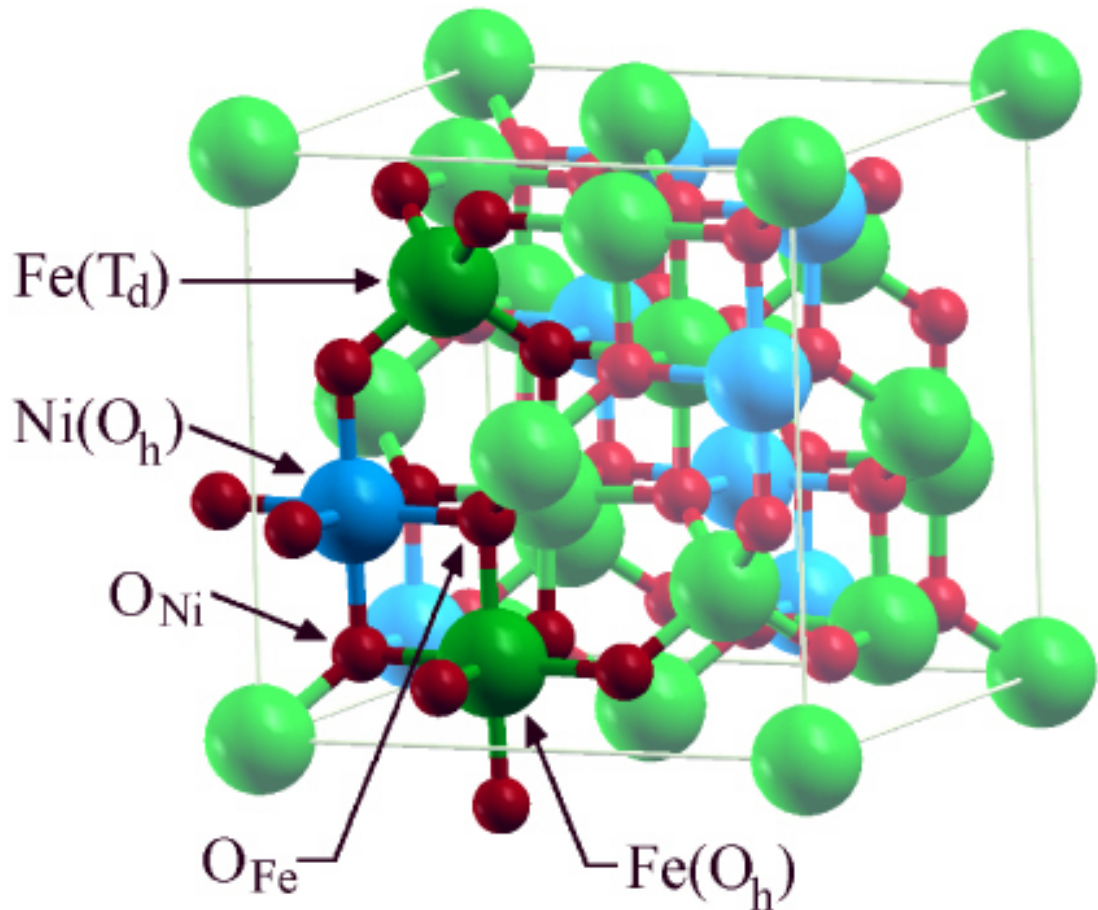


Figure 1 - Crystal structure of nickel ferrite showing the tetrahedral A sites ( $T_a$ ) and the octahedral B sites ( $O_a$ )

Ferrimagnetism arises in ferrites because the exchange interaction between A and B sites is negative. In nickel ferrite, the Fe ions' magnetic moments, evenly distributed between the two types of site, cancel each other out leaving only the contribution from the nickel ions. This gives rise to the small net remanent magnetisation in terms of the Bohr magneton,  $\mu_B$  of approximately  $2 \mu_B/\text{molecule}$  [14].

## 1.2. Magnetic Anisotropy in Nickel Ferrite

The cubic ferrites, including nickel ferrite, exhibit cubic magnetocrystalline anisotropy in a similar manner to pure nickel. That is to say with  $\langle 111 \rangle$  easy directions,  $\langle 100 \rangle$  hard directions and intermediary  $\langle 110 \rangle$  medium axes.

The anisotropy energy due to cubic magnetocrystalline anisotropy, in a direction described by the direction cosines  $\alpha_1, \alpha_2$  and  $\alpha_3$  to the crystal axes, is given by

$$E = K_0 + K_1(\alpha_1^2\alpha_2^2 + \alpha_2^2\alpha_3^2 + \alpha_3^2\alpha_1^2) + K_2(\alpha_1^2\alpha_2^2\alpha_3^2) + \dots \quad (1-1)$$

Where  $K_n$  is the  $n$ th order anisotropy constant, expressed in  $\text{Jm}^{-3}$ . Conventionally, anisotropy constants above the 2<sup>nd</sup> order are small enough to be ignored and sometimes the  $K_2$  are ignored as well for the same reason. The first term,  $K_0$  is independent of angle, and so it is often ignored as well. For nickel ferrite, Smith and Jones [15] give the anisotropy constants as:

$$K_1 = -7 \times 10^3 \text{ Jm}^{-3} \text{ and } K_2 = -50 \text{ Jm}^{-3}.$$

It is these negative anisotropy constants which give rise to the <111> easy axes. In Chapter 4 we fully evaluate the theoretical anisotropy energy of each of our three samples using micro-magnetic modelling and it is shown that the <111> directions correspond to energy minima, the defining characteristic of an easy axis.

This means that a disc cut in a plane of the form {100} will exhibit a “bi-axial” anisotropy with two hard axes in the plane and perpendicular to each other as shown in Figure 2. A further set of medium “biaxial” axes also lie in the plane and

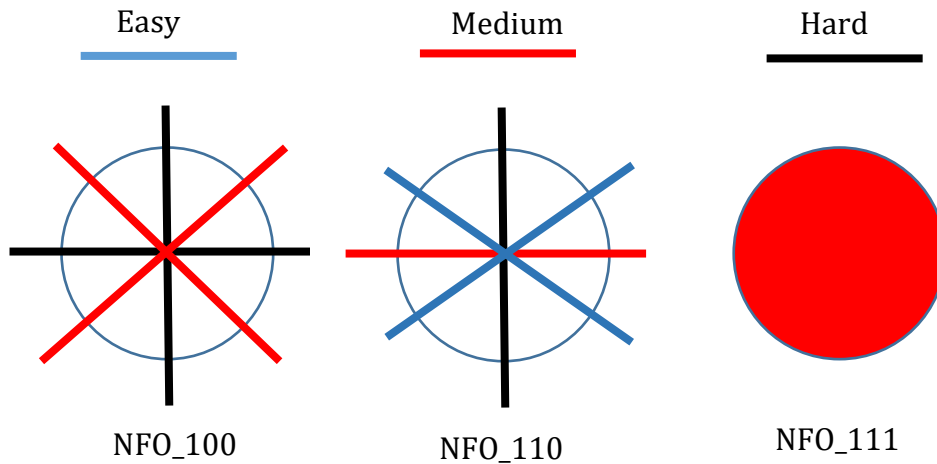


Figure 2 - Showing the Anisotropy axis directions for the NFO\_100, NFO\_110 and NFO\_111 discs. With black for hard axes, red for medium and blue for easy. In the case of the NFO\_111 disc, the anisotropy energy is approximately that of a medium axis but is present in all directions. (i.e isotropic)

are at  $45^\circ$  to the set of hard axes as also shown in Figure 2. The disc cut in a plane of the form  $\{110\}$  has a more complicated structure with alternating hard, easy, medium and easy axes in the plane. In this case, the hard and medium axes are expected to be perpendicular but the easy axes are not at  $45^\circ$  to either, falling approximately  $35^\circ$  ( $\tan^{-1}(\frac{1}{\sqrt{2}})$ ) with respect to the medium axis, and is the angle between the body-diagonal and the adjacent plane of the cubic structure. Finally the  $\{111\}$  disc is expected to be almost entirely isotropic in the plane. Again this is demonstrated in Chapter 4

### 1.3. Magnetostriction of Nickel Ferrite

Magnetostriction is the term used to describe the change of dimensions of a substance when a magnetic field is applied [16]. The fractional change in length,  $\frac{\Delta l}{l}$  is simply a strain, and to distinguish it from mechanically induced strain due to an applied stress,  $\epsilon$ , the magnetically induced strain is given the symbol  $\lambda$ :

$$\lambda = \frac{\Delta l}{l}. \quad (1-2)$$

As this study is concerned with the anisotropy of the ME response due to the magnetostriction, it is important to develop a theoretical understanding of  $\lambda$  as a function of rotation within an applied field. In this section three equations are developed corresponding to the three crystallographic orientations of our sample set. The magnetostriction as a function of applied field is complicated, requiring consideration of domain wall motion and the magnetocrystalline anisotropy of a substance. Chikazumi describes this process for crystals magnetised in the  $\langle 100 \rangle$ ,  $\langle 110 \rangle$  and  $\langle 111 \rangle$  directions [17]. Further, a magnetised sample will undergo an additional strain, known as the Form Effect. This occurs as the sample deforms to reduce its magnetostatic energy, which is shape dependent. In essence the distortion is to reduce the demagnetising field in the sample.

A more useful and accessible metric is the saturation magnetostriction. For cubic crystals the saturation magnetostriction in a given direction,  $\lambda_{si}$  defined in terms of the saturation magnetostriction in the  $\langle 100 \rangle$  and  $\langle 111 \rangle$  directions,  $\lambda_{100}$  and  $\lambda_{111}$  respectively, as [18]:

$$\lambda_{si} = \frac{3}{2} \lambda_{100} \left( \alpha_1^2 \beta_1^2 + \alpha_2^2 \beta_2^2 + \alpha_3^2 \beta_3^2 - \frac{1}{3} \right) + 3 \lambda_{111} (\alpha_1 \alpha_2 \beta_1 \beta_2 + \alpha_2 \alpha_3 \beta_2 \beta_3 + \alpha_3 \alpha_1 \beta_3 \beta_1), \quad (1-3)$$

Where  $\alpha_n$  are the direction cosines of the applied field to the crystal axes and  $\beta_n$  are the direction cosines to the magnetostriction we are interested in. In spherical polar coordinates the direction cosines are defined as:

$$\alpha_1 = \cos\theta \sin\phi \quad (1-4)$$

$$\alpha_2 = \sin\theta \sin\phi \quad (1-5)$$

$$\alpha_3 = \cos\phi \quad (1-6)$$

where  $\theta$  is the azimuthal angle and  $\phi$  is the polar angle as shown in Figure 3.

In general, we are interested only in the magnetostriction in the field direction such that  $\alpha_1 = \beta_1, \alpha_2 = \beta_2$  and  $\alpha_3 = \beta_3$  and so that we get:

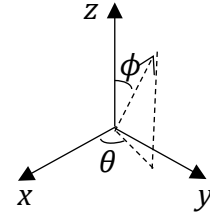


Figure 3 - Spherical polar coordinates

$$\lambda_{si} = \frac{3}{2} \lambda_{100} \left( \alpha_1^4 + \alpha_2^4 + \alpha_3^4 - \frac{1}{3} \right) + 3 \lambda_{111} (\alpha_1^2 \alpha_2^2 + \alpha_2^2 \alpha_3^2 + \alpha_3^2 \alpha_1^2) \quad (1-7)$$

Further reduction can be achieved using the relation:

$$(\alpha_1^2 + \alpha_2^2 + \alpha_3^2) = (\alpha_1^4 + \alpha_2^4 + \alpha_3^4) + 2(\alpha_1^2 \alpha_2^2 + \alpha_2^2 \alpha_3^2 + \alpha_3^2 \alpha_1^2) \quad (1-8)$$

Yielding:

$$\lambda_{si} = \lambda_{100} + 3(\lambda_{111} - \lambda_{100})(\alpha_1^2 \alpha_2^2 + \alpha_2^2 \alpha_3^2 + \alpha_3^2 \alpha_1^2) \quad (1-9)$$

We use this “two constant equation” to determine the saturation magnetostriction. The two constant equation (1-9) is evaluated in terms of the “sample rotation angle,”  $\psi$  in a particular plane. For example in the {100} plane the sample is rotated in the  $x$ - $y$  plane such that  $\psi = \theta$  as can be seen in Figure 3.

The magnetostriction, being a strain, is a dimensionless ratio and is a small-scale effect. For example in iron [17]:

$$\lambda_{100} = 20.7 \times 10^{-6}, \quad \lambda_{111} = -21.2 \times 10^{-6}$$

And in nickel [17]:

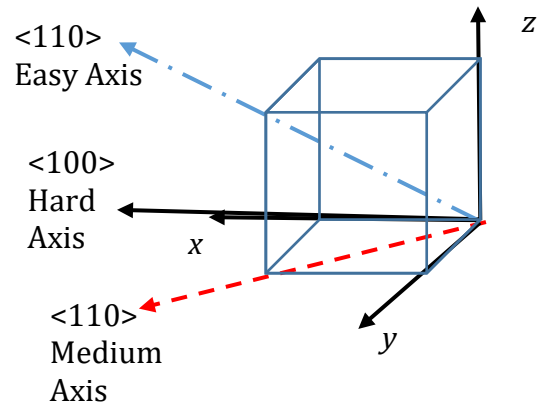
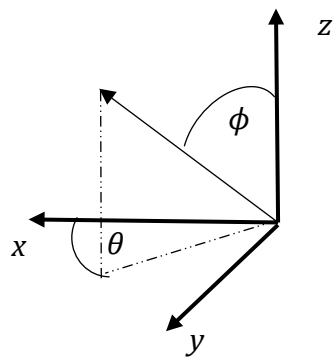
$$\lambda_{100} = -45.9 \times 10^{-6}, \quad \lambda_{111} = -24.3 \times 10^{-6}$$

Smith and Jones [15] measured the magnetostriction in nickel ferrite to be:

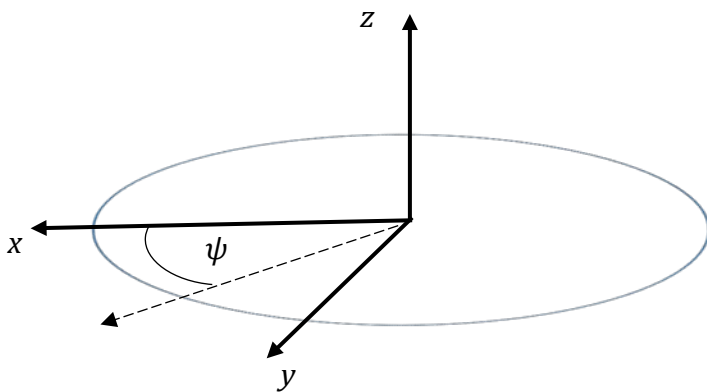
$$\lambda_{100} = -45.9 \times 10^{-6}, \quad \lambda_{111} = -21.6 \times 10^{-6}$$

Where a negative magnetostriction implies the substance contracts in the direction of an applied field.

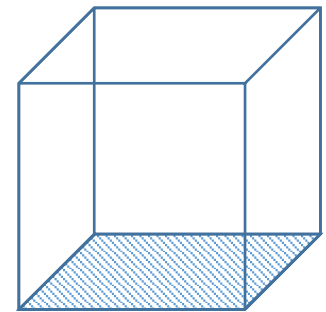
We now consider our samples, which are cut in planes of the form {100}, {110} and {111} as shown in Figure 4.



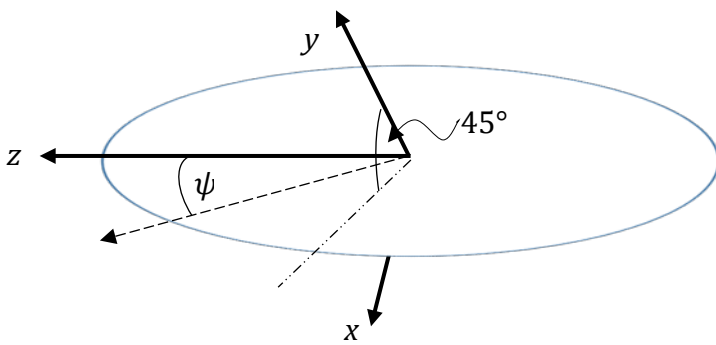
(a)



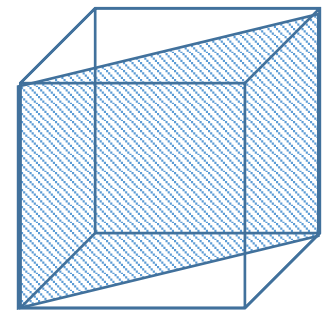
NFO\_100



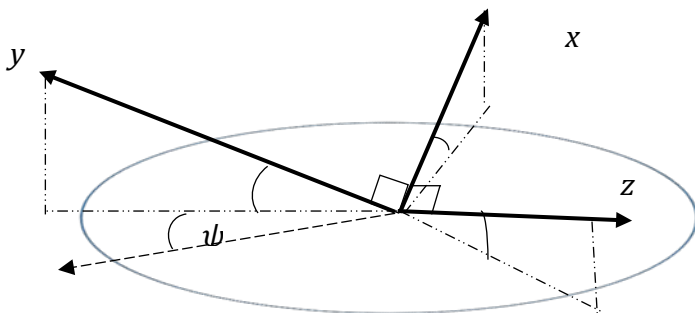
(b)



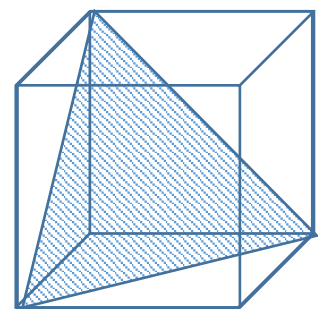
NFO\_110



(c)



NFO\_111



(d)

Figure 4 - Showing the directions in which the crystal axes occur in the NFO samples. In the (a) the relationship between the crystal axes and the crystallographic directions is demonstrated. (b), (c) and (d) represent the planes of the NFO\_100, NFO\_110 and NFO\_111 samples respectively. It is important to note that the angles between the crystal axes and the plane in the NFO\_111 case are equal for all three crystal axes.

### 1.3.1. NFO\_100

In the case of a {100} disc we know from Figure 4 that  $\theta = \psi$  and  $\phi = 90^\circ$  so the direction cosines take the form of:

$$\alpha_1 = \cos\psi$$

$$\alpha_2 = \sin\psi$$

$$\alpha_3 = 0$$

and so:

$$\lambda_{si} = \lambda_{100} + 3(\lambda_{111} - \lambda_{100})(\sin^2 \psi \cos^2 \psi) \quad (1-10)$$

and by the identity  $\sin^2 \theta \cos^2 \theta \equiv \frac{1}{4} \sin^2 2\theta$ :

$$\lambda_{si} = \lambda_{100} + \frac{3}{4}(\lambda_{111} - \lambda_{100}) \sin^2 2\psi. \quad (1-11)$$

Using the nickel ferrite values for  $\lambda_{100}$  and  $\lambda_{110}$  given earlier a polar plot of equation (1-11) is shown in Figure 5 as a function of sample rotation. This gives rise to a biaxial arrangement as seen in Figure 5, where the greatest contraction occurs along the hard axes and the smallest contraction occurs along the magnetic medium axes.

Note that the magnetostriction shown in Figure 5 is negated. This is so that the magnetostriction is in terms of contraction instead of the conventional terms of expansion, which is to allow for easier comparison with the experimental results of Chapter 5 where the magnitude of the magnetostriction is important but whether the sample expands or contracts is not.

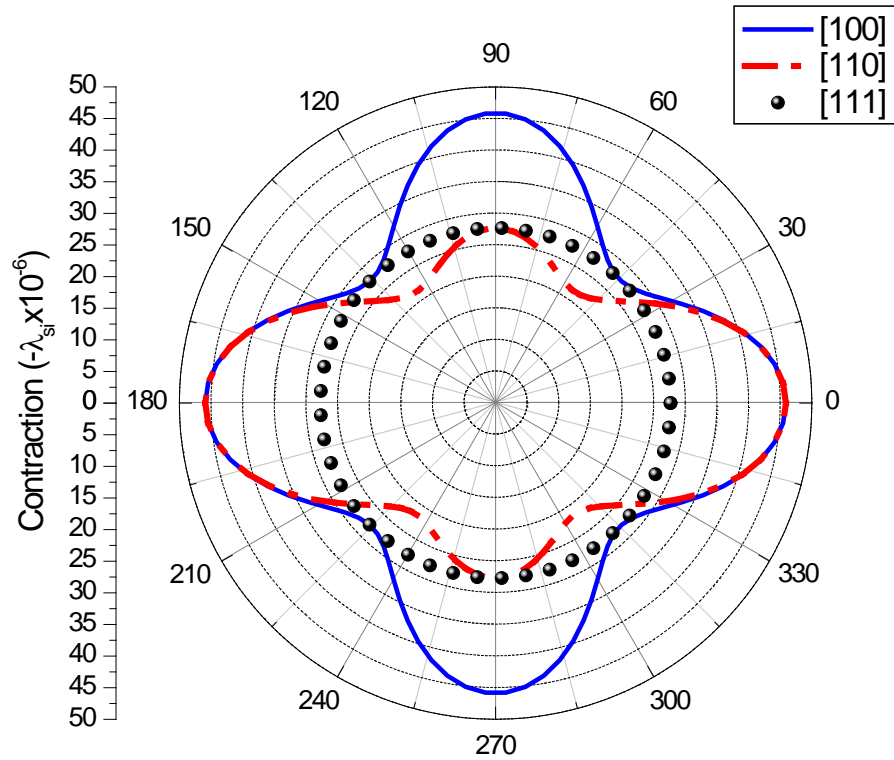


Figure 5 - Saturation magnetostriction as a function of sample rotation for discs cut in {100}, {110} and {111}. Note that the magnetostriction is presented negated so that it is in terms of contraction rather than extension.

### 1.3.2. NFO\_110

For the {110} disc, measuring from the vertical <100> direction, the z-axis in

Figure 4, such that  $\theta = \frac{1}{\sqrt{2}}$  and  $\phi = \psi$  we get:

$$\alpha_1 = \alpha_2 = \frac{\sin\psi}{\sqrt{2}}$$

$$\alpha_3 = \cos\psi$$

So:

$$\lambda_{si} = \lambda_{100} + 3(\lambda_{111} - \lambda_{110})\left(\frac{\sin^4 \psi}{4} + \sin^2 \psi \cos^2 \psi\right) \quad (1-12)$$

which simplifies to

$$\lambda_{si} = \lambda_{100} + \frac{3}{4}(\lambda_{111} - \lambda_{110})(\sin^4 \psi + \sin^2 2\psi) \quad (1-13)$$

Here the  $\sin^2 2\psi$  term is the biaxial term as with the {100} disc, which has been superposed with a uniaxial term,  $\sin^4 \psi$ . This implies 4 directions in which the contraction of the sample is minimum along the easy directions, two medium directions with intermediate contraction and two hard directions with maximum contraction as shown in Figure 5.

### 1.3.3. NFO\_111

The disc cut in the {111} plane contracts isotropically in the plane. This is because in this case the term:

$$\alpha_1^2 \alpha_2^2 + \alpha_2^2 \alpha_3^2 + \alpha_3^2 \alpha_1^2 = \frac{1}{4}$$

for every direction in the plane, and so the magnetostriction is:

$$\lambda_{si} = \frac{\lambda_{100} + 3\lambda_{111}}{4}. \quad (1-14)$$

This is insensitive to  $\psi$  and so the magnetostriction is isotropic in-plane as shown in Figure 5.

From this theoretical development and the magnetic anisotropy expected from the micro-magnetic modelling of Chapter 4 we expect the magnetostriction to align along the anisotropy axes of Figure 2 in the order of maximum magnetostriction along the hard axis, minimum along the easy axis and with an intermediate magnetostriction along the medium axis. In the next section we consider the piezoelectric layer and its response to the stress applied by the mechanically bonded magnetostriction of the magnetic layer.

#### **1.4. Piezoelectricity**

Piezoelectricity is the property of a crystal by which deformation, or strain, of the crystal induces electric polarization in the material, and therefore causes a charge on the crystal's surface. This effect is small, on the order of  $\text{\AA}/V$ . There also exists the converse piezoelectric effect so an applied electric field induces strain in the crystal. The Piezoelectric used in this project is the commonly used lead zirconate titanate (PZT), an equimolar solid solution of lead zirconate and titante:  $\text{PbZrO}_3\text{-PbTiO}_3$  [19].

All crystals that are in a ferroelectric state exhibit piezoelectric behaviour, but a crystal can be piezoelectric without being ferroelectric [20].

In 1-dimension this effect is defined as:

$$P = zd + E\chi \quad (1-15)$$

Where  $P$  is the polarisation,  $z$  is the applied strain,  $d$  the piezoelectric coefficient,  $E$  the applied electric field and  $\chi$  is the permittivity of the material.

The polarisation arises from a loss of symmetry within crystals. Figure 6 shows how this occurs in a crystal in a ferroelectric state. This is the way in which PZT exhibits piezoelectricity. As the crystal is distorted the separation between positive and negative ions is increased causing an increase in electric polarisation.

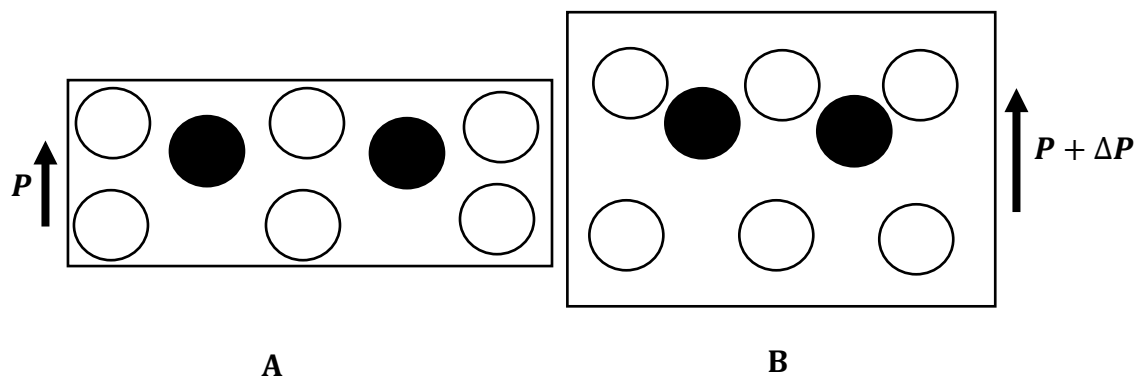


Figure 6 - Schematic representation of piezoelectricity in a material with spontaneous polarisation (A) without stress and (B) under strain. The white and black circles represent negatively and positively charged ions respectively.

## 1.5. Multiferroic composites and the magnetoelectric effect.

As mentioned earlier, Multiferroic materials exhibit multiple ferroic ordering parameters such as ferromagnetism, ferroelectricity and ferroelasticity. Ferroic order parameters get their name because of how they respond to applied fields in a similar way to how the magnetisation responds to applied magnetic fields in ferromagnetic materials. That is to say, when no field is applied there is spontaneous ordering, which requires a large opposing field to switch the direction of this ordering. This causes the well-known hysteresis loop, such as in Figure 7.

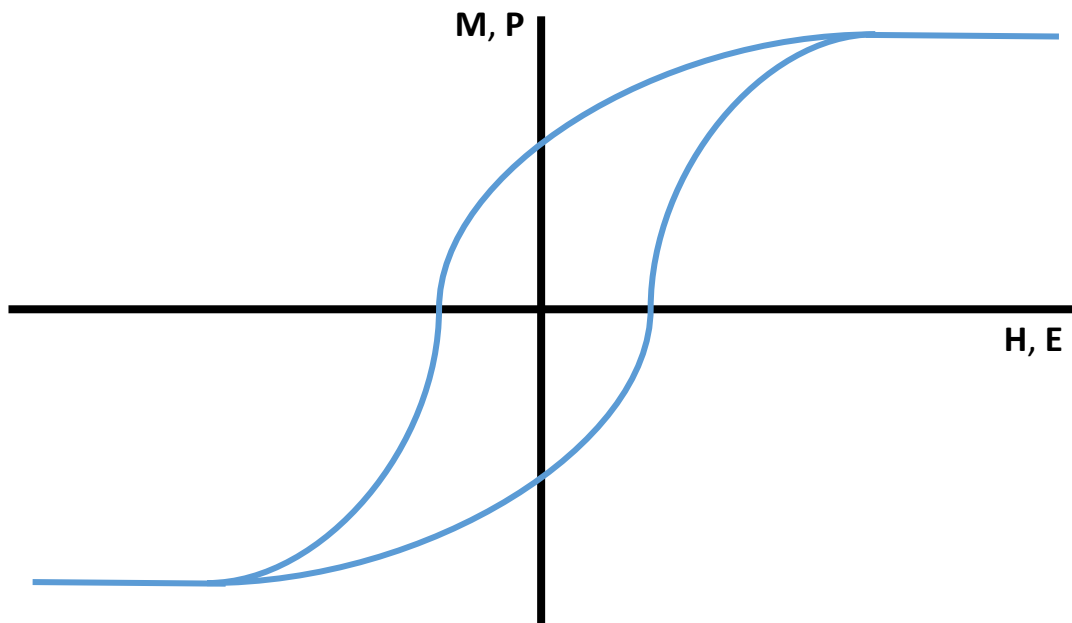


Figure 7 - Schematic of a hysteresis loop for Ferromagnetic or Ferroelectric materials

In some multiferroic materials there exists a coupling between multiple ferroic order parameters. The coupling between ferromagnetism and ferroelectricity results in magnetic-field-induced polarisation or electric-field-induced magnetisation as shown schematically in Figure 8. This is known as the magnetoelectric (ME) effect.

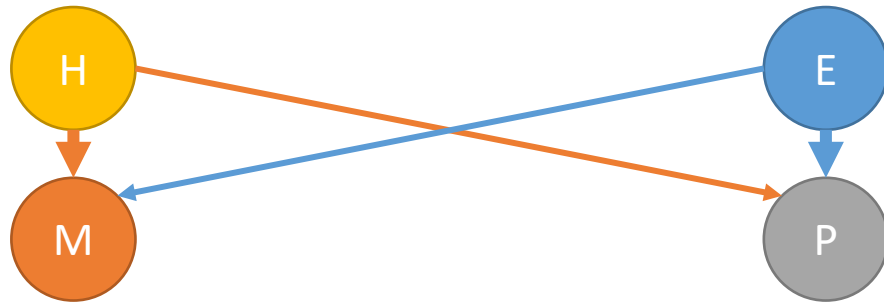


Figure 8 - Schematic of the ME effect where  $H$  is the applied magnetic field,  $E$  applied electric field,  $M$  is magnetisation and  $P$  is the polarisation. The thick down arrows represent the direct effect of an applied stimulus and the thin diagonal lines represent the induced ME effects.

Röntgen discovered that a moving dielectric became magnetised when placed in a magnetic field in 1888 [21], followed by a demonstration of the reverse effect, a moving dielectric becoming polarised in a magnetic field 17 years later. Curie suggested the possibility of intrinsic ME behaviour of non-moving crystals in 1894 and the term magnetoelectric was coined in 1924 by Debye [6]. It wasn't until the early 1960s that experimental confirmation of the ME effect, both in terms of magnetic-field-induced polarisation and electric-field-induced magnetisation, in  $\text{Cr}_2\text{O}_3$  [22-25].

For a small period of time, new ME materials were found including:  $\text{Ti}_2\text{O}_3$ ,  $\text{GaFeO}_3$ , and several phosphate and boracite compounds. However, the ME coefficient of these materials was found to be too low (approximately  $7 \text{ mV cm}^{-1} \text{ Oe}^{-1}$ ) for practical applications and multiferroic research floundered in the 1970s.

The weakness of intrinsic ME materials was overcome in 2001 with the advent of laminate composites. By combining highly magnetostrictive and piezoelectric

materials large ME coefficients up to 700 times greater than those found in single-phase composites can be produced. Mainly formed by epoxy-bonding or co-firing, laminate composites operate through the strain-mediated ME effect, where an applied magnetic field causes the magnetostrictive material to strain which in turn causes the piezoelectric material to strain and polarise due to piezoelectricity.

Due to the sensitivity to multiple stimuli the potential applications of ME composites are many and varied. Including Magnetic sensors [26], current sensors, transformers, gyrators, energy harvesters [27], Magnetic Random Access Memory (MRAM) [28], tunnel junctions [29], voltage tunable inductors, tunable band-pass filters, phase shifters, tunable resonators [30], magnetic recording read heads [31] and even solid-state cooling applications [32, 33].

One of the main advantages of Multiferroic materials, especially for memory applications such as MRAM and magnetic recording read heads is the interaction between magnetic fields and electric fields, instead of the conventional magnetic-field-current interaction. For example traditional recording read-write heads utilise the magnetic field induced by an electric current to encode data onto a recording medium and then the data is read by magnetoresistive processes [34] which require a constant DC test current through the sensor and so leads to heat loss. In a magnetoelectric read-write head, the encoding field is electric-field induced, which requires only the application of a potential difference, thus eliminating the power loss due to current flow and the data can be read back

directly as an induced voltage [35]. This heat-less operation has huge ramifications for miniaturisation where conventional memory technologies are facing challenges [36].

A good example of the versatility of strain mediated multiferroic composites is their use as energy harvesters. Primarily extracting energy from stray magnetic fields, the piezoelectricity of the device also enables energy harvesting from mechanical vibrations. As both of these energy harvesting operations use the piezoelectricity they can be performed simultaneously. Ryu *et al.* [37] demonstrated a Magneto-mechano-electrical (MME) generator made from a flexible piezoelectric single crystal fiber composite, a magnetostrictive Ni plate and Nd permanent magnetic proof mass. This generator is able to power 35 LEDs and drive a wireless sensor network in a small magnetic field of 5-7 Oe. Our work could help optimise these energy harvesters by ensuring the maximum power output by selectively texturing the crystal fibers to enhance the ME response in the field direction.

The use of ME materials in magnetic sensor devices allows an alternative to conventional Hall sensors or giant magnetoresistive (GMR) devices [38] and due to their passive nature and self-powered room temperature operation may be able to replace superconducting quantum interface devices (SQUIDs). The literature for ME magnetic sensors is extensive, covering: different categories of sensor construction [39], sensor unit packaging, fabrication techniques [40] and signal processing conditions [41]. Low-cost, miniaturised sensor devices with

high sensitivity and spectral resolution can be fabricated using thin film-based ME sensors, as demonstrated by Roebisch *et al.* [4].

Although this project has focused on the direct ME coupling effect, the converse ME effect is widely studied as well. For example some reports detail a possible control of coercive field of multiferroics by the application of a voltage/electric field [42, 43], while others have shown a direct control of magnetization by the application of an electric field [44]. This has been widely studied for the ability to switch magnetisation, and thus memory states in MRAM applications [45-51].

## 1.6. Sample Details

The samples used in this study are NFO/PZT magnetoelectric bilayers. The two layers are bonded with super glue and are slightly offset from each other to allow an electrical contact to be attached to each side of the

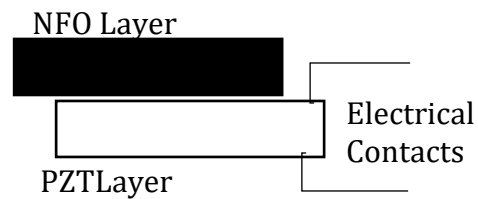


*Figure 9 - Schematic of NFO/PZT bilayers, showing how the electrical contacts are connected to either side of the PZT layer.*

piezoelectric layer as shown in Figure 9. The magnetocrystalline anisotropy is controlled by having 3 samples oriented in the {100}, {110} and {111} crystallographic planes, confirmed by the X-Ray Diffraction spectra shown in Figure 10 given by M Vopson an external advisor on this project [52]. These scans were performed using Cu-k  $\alpha$  radiation. The peaks indicate the presence of a crystallographic orientation in a sample. The angle of reflection at which these

peaks occur is as result of the lattice spacing of a particular plane as described by Bragg's law. The dominance of peaks due to one crystal orientation show good alignment has been achieved in our sample set.

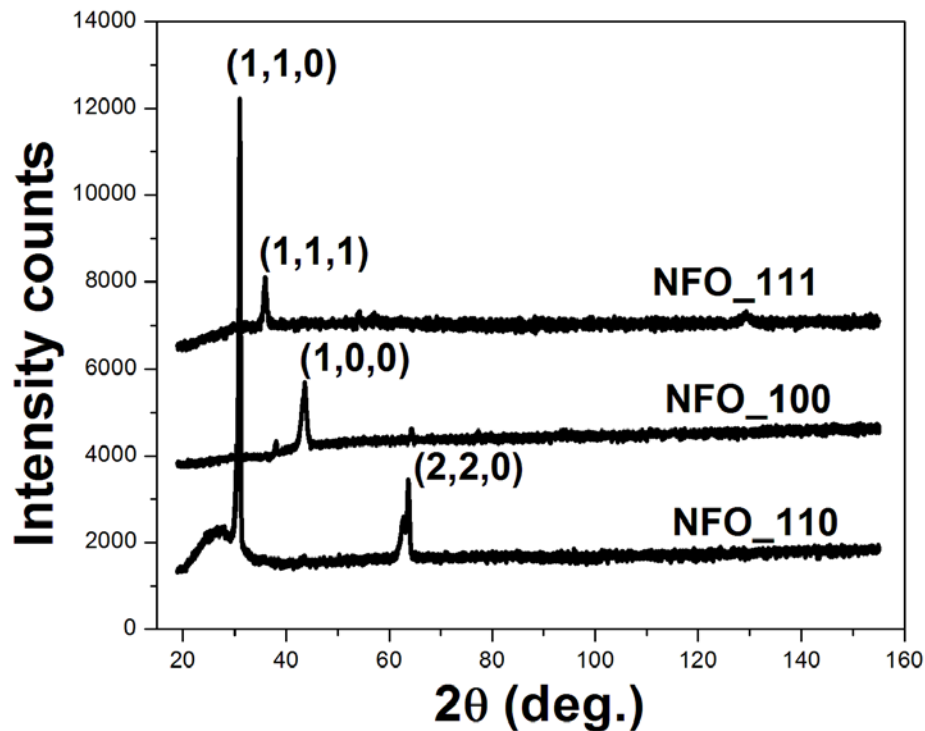


Figure 10 - X-Ray Diffraction spectra for the NFO\_100, NFO\_110 and NFO\_111 samples

## 1.7. Structure of this Thesis

This thesis begins with a description of the work developing the biaxial vibrating sample magnetometer to enable magnetic anisotropy measurements. The sensitivity profile of this machine is measured and compared with theory to determine the optimal sample position. However rotating a sample can cause it to precess, moving it from the ideal position. A method to reduce this precession by effectively shifting it to a different part of the machine is detailed and its efficacy is demonstrated. The completed biaxial VSM is tested by performing anisotropy measurements on known hard and soft magnetic samples including

direct measurement of the distribution of easy axes in hard samples and the identification of a sample's magnetic anisotropy axes directions and relative strengths using a modified torque magnetometry technique.

Also in chapter 2 the development of a dedicated Magnetolectric measurement rig is detailed. This rig required the simultaneous application of DC and AC magnetic fields and the rotation of the sample. As well as enabling electrical connections to the contacts attached to the piezoelectric layers of the multiferroic samples.

The torque magnetometry technique is expanded in chapter 3. A “reducing field” method was used to overcome a known limitation of using a biaxial VSM for torque magnetometry, where the measured signal reduces to zero as the sample approaches saturation (the point at which the torque is actually maximised). Further, a new method, based on the principle of torque magnetometry of determining the anisotropy directions in a sample using a standard VSM with sample rotation capabilities is laid out.

Chapter 4 details the process of basic micromagnetic modelling which is used to predict the anisotropy energies of Nickel ferrite when cut in planes of the form  $\{100\}$ ,  $\{110\}$  and  $\{111\}$ . It is hoped that this can be expanded to provide insight further insight into the magneto-mechanical behaviour of these discs and then the magnetolectric behaviour of our NFO/PZT samples.

The main results of this investigation are presented and discussed in chapter 5 with particular focus on the relation between the magnetic anisotropy, magnetostriction and the magnetoelectric response of the multiferroic samples. The optimum bias field and the strength of the ME coupling as a function of sample rotation are shown. These are compared to the expected magnetostriction evaluated in Section 1.3 by taking the product of the optimum field and peak signal which is shown to be proportional to the saturation magnetostriction  $\lambda_{si}$ . The behaviour of the magnetoelectric coefficient  $\alpha$  is also investigated as a function of sample rotation.

## **2. Development of magnetic and magnetoelectric measurement devices and methods.**

There are many ways to perform Magnetic Anisotropy measurements, such as direct and indirect Torque magnetometry [53, 54], Transverse Susceptibility [55], measurement of Easy Axis Distributions [56] and the determination of anisotropy constants derived from both static and rotational magnetisation curves [57]. A bi-axial vibrating sample magnetometer (also known as a vector-VSM) is a versatile and robust instrument as it allows multiple different measurement techniques to be applied to both hard and soft magnetic samples and was one of the two main instruments used in this study.

The other important aspect of this investigation required the determination of the electrical response of multiferroic composites to a magnetic field stimulus, that is typically referred to as the strain-mediated Magneto-Electric coupling (ME) response, along with its associated ME coupling coefficient [5]. This allowed the texture-induced anisotropy axes, characterised and found from the bi-axial VSM measurements, to be mapped onto the ME response and studied as a function of relative sample and applied field direction. In addition to being interesting from a purely scientific point of view, being able to routinely ‘tune’ the response of an ME device in such a way could be important for introducing additional functionality into the potential applications described in more detail in Chapter 1. Hence, a specialist rig that measures the ME response was built as part of this project and is also described here.

The chapter starts with the general VSM technique, where the moment is measured in the applied field direction, and is then extended to the full bi-axial set-up that includes sample rotation and full vector determination in the sample plane. The necessary re-commissioning of the bi-axial VSM at Preston is described, including the measurement and characterisation of the sensitivity profile across the measurement plane along with the reduction of sample precession under rotation. Results of testing the rig are given, carried out by using well-established characterisation techniques on known samples, before the final development of the torque curve measurements is detailed. This includes a change to the standard methodology in order to maximise sensitivity, which reduces at large fields when performed using a biaxial VSM. The modified methodology uses repeated measurements at different fields to highlight the important features. The chapter closes with details of the development of the ME coupling rig.

## **2.1. Vibrating Sample Magnetometry**

A vibrating sample magnetometer (VSM), first developed by Foner in 1955 [58], measures the magnetic properties of a material by detecting a change in magnetic flux in nearby pick-up coils as the sample is moved up and down at a low frequency (tens of Hz) incommensurate with the 50 Hz of the mains supply. Generally the frequency of operation is within audio ranges and early VSMs used

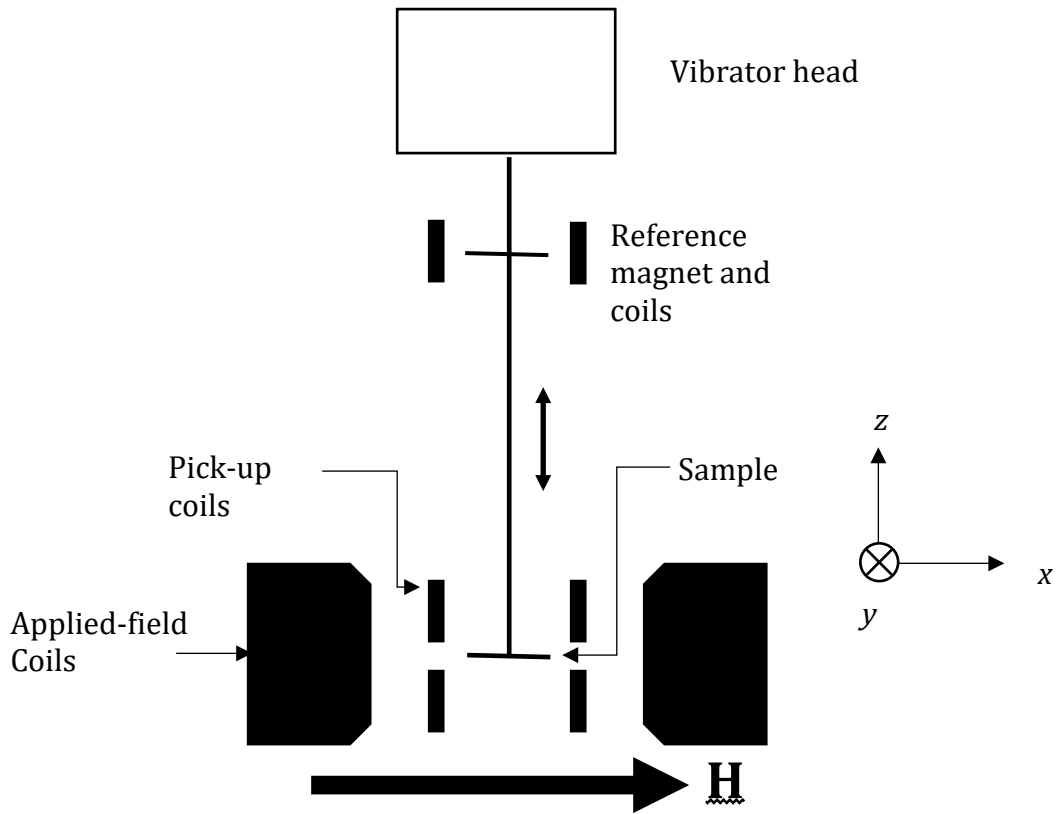


Figure 11 - Schematic representation of a standard VSM

loudspeaker cones to vibrate the sample. The EMF induced by the moving sample allows detection of the sample moment individually while also imparting frequency, amplitude and phase control. As control, and therefore selection, of the frequency is available noise reduction can be readily achieved by use of lock-in amplification, a method by which only signals of a particular frequency and phase-shift are detected.

Figure 11 shows a schematic of a standard VSM with the sample vibrating perpendicular to the applied field. Standard VSMs measure the component of a sample's moment in the field direction, normally using a balanced set of an even number of pick-up coils as shown to make the additive induced voltage response flat and relatively insensitive to the sample's position (the saddle point) around

the centre of the coil set. Bi-axial (Or Vector) VSMs have specially designed sets of pick-up coils as shown in Figure 12, with an additional set perpendicular to the standard set in the  $x$ - $y$  plane that enables measurement of both of these components and thus allows the in-plane vector moment to be determined. Coupled with sample

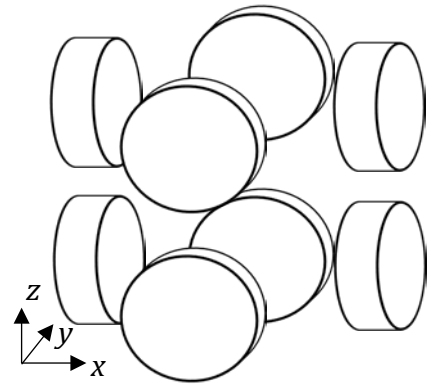


Figure 12 - Coil configuration of the bi-axial VSM at UCLan

rotation, bi-axial VSMs are a powerful tool for anisotropy measurements. However, with these more complex pick-up coils, position insensitivity is harder to achieve due to the existence of two saddle points that need to be aligned. The advantage of this system over others as described by Bernards [59] is in the ability to measure both components of the magnetisation vector at once without having to switch the coil arrangement. Further, unless care is taken, samples are likely to precess while undergoing rotation causing them to move in relation to the pick-up coils, with this being a significant issue in the UCLan vector VSM that was addressed as detailed later in this chapter.

## 2.2. Sensitivity Profiles of the bi-axial VSM

### 2.2.1. Theoretical

We begin by considering the sensitivity profile of the pick-up coils. Consider a set of coils each with diameter  $C_d$ , thickness  $C_l$ , and a central bore of diameter  $C_b$  as shown in Figure 13. Bernards shows, for a set of  $n$  such coils (4 in each of our coil sets) the induced voltage due to a sample at position  $\mathbf{P}$  is equal to:

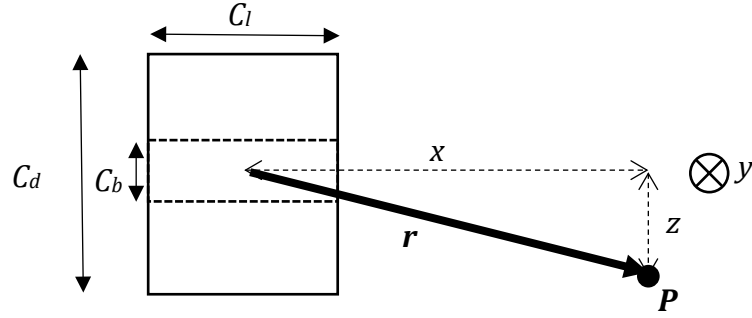


Figure 13 - Coil Dimensions of a single coil. The position  $\mathbf{P}$  defines the coordinate system used when considering the response to a sample at that point.

$$V_{tot} = \mu_0 M_x V v \frac{N}{a} \sum_{i=1}^n S_{x,i} S_{x,i} \quad (2-1)$$

where  $\mu_0$  is the permeability of free space,  $M_x$  is the component of the magnetisation in the in-field ( $x$ ) direction,  $V$  the sample's volume,  $v$  the samples velocity due to the vibration in the  $z$ -direction,  $N$  the number of turns in each pick-up coil and  $a$  the cross-sectional area of the coil. The sign of the coil,  $s_{x,i}$ , is such that the term  $s_{x,i} S_{x,i}$  is always positive in the measurement plane, due to the push-pull configuration of our coil set. The sensitivity function,  $S_{x,i}$  of each particular coil to the component of the magnetic moment in the in-field direction is dependent on the dimensions and position of the coil and is defined as:

$$S_x(x, y, z) = \sum_{l=1,3,5} B_l \frac{l+1}{r^{l+3}} \frac{z}{r} P'_{l+2}(\gamma), \quad (2-2)$$

where  $r$  is the distance of the sample from the centre of the coil given by  $r^2 = x^2 + y^2 + z^2$  and  $\gamma = \frac{x}{r}$ . The first set of coefficients, the  $B_l$  are given as:

$$B_1 = \left(\frac{C_b}{2}\right)^4 \frac{\beta}{6} (\alpha^3 - 1),$$

$$B_3 = - \left(\frac{C_b}{2}\right)^6 \frac{\beta}{120} [9(\alpha^5 - 1) - 20\beta^2(\alpha^3 - 1)] \text{ and}$$

$$B_5 = \left(\frac{C_b}{2}\right)^8 \frac{\beta}{336} [15(\alpha^7 - 1) - 84\beta^2(\alpha^5 - 1) + 56\beta^4(\alpha^3 - 1)],$$

in which  $\alpha = C_d/C_b$  and  $\beta = C_l/C_b$ .

The  $P_{l+2}$  are given by the Legendre polynomials of:

$$P_{l+2}(\gamma) = \frac{1}{2^{l+2}(l+2)!} \left(\frac{d}{d\gamma}\right)^{l+2} (\gamma^2 - 1)^{l+2}.$$

We evaluate this by substituting  $l = 1, 3, 5$ , before differentiating with respect to  $\gamma$  to give  $P'_{l+2}(\gamma)$  as in (2). From this it can be seen that  $S_x$  is dependent on sample position:  $x, y$  and  $z$ , and coil dimensions  $C_l, C_d$  and  $C_b$ , only.

### 2.2.2. Experimental

To measure the sensitivity we simply have to measure the magnetisation of a sample as it is moved around on the  $x$ - $y$  plane. For accurate measurements a small sample is required in order to minimise convolution effects. As Nickel has a relatively high magnetisation of  $510 \text{ emu/cm}^3$  [60] and is readily available in foil form, a  $25 \text{ }\mu\text{m}$  thick Ni foil sample of approximately 1 mm diameter was used and

referred to as the “nickel dot”.

However, as Ni is magnetically soft and thus requires an applied field in order to obtain a measureable magnetic moment, it was unsuitable for measurements of the transverse coil set that is, by definition, perpendicular to the field. Hence, a necessarily larger (smaller magnetisation) but magnetically hard sample made from a suspension of  $\gamma\text{-Fe}_2\text{O}_3$  in PVA glue, with dimensions of  $(2 \times 1 \times 1) \text{ mm}^3$ , was made that would enable remanent magnetisation to be used. Comparison of the results for these two samples for the sensitivity in the z-direction is shown in Figure 14. The good agreement between the two samples is evidence that any convolution effects are minimal, with further confidence being given in the close fit to the theory of Bernards detailed earlier. This meant that the use of the

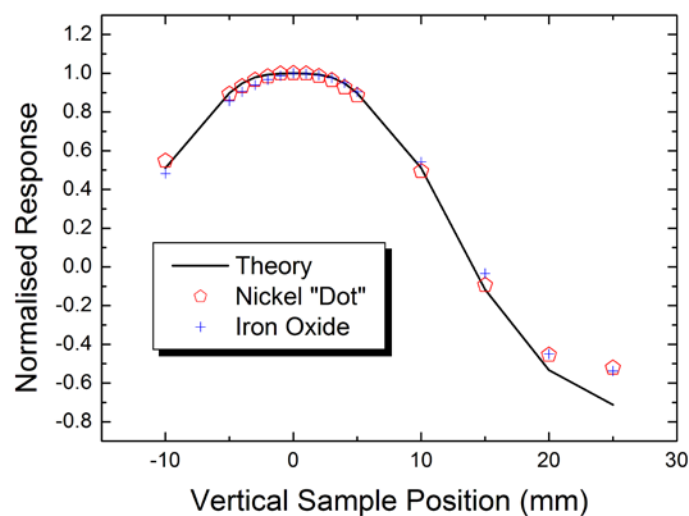


Figure 14 - Comparison of Nickel dot, Iron Oxide and theory to demonstrate minimal convolution effects.

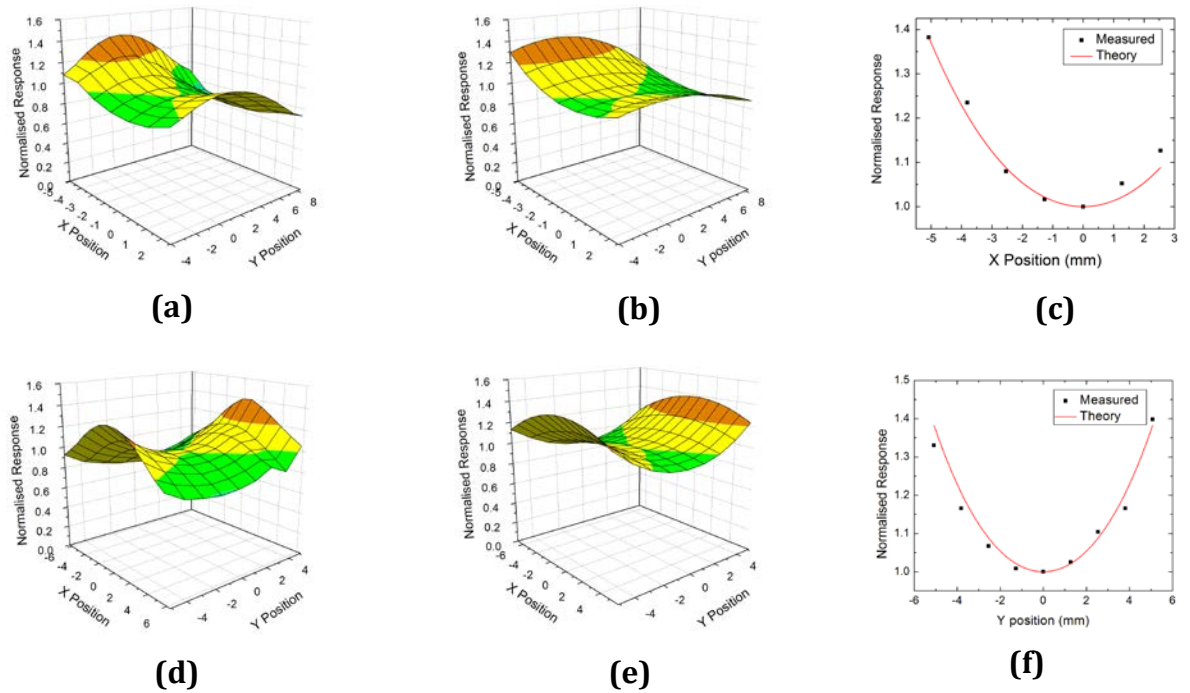


Figure 15 - Normalised Response curves for Parallel (a-c) and Transverse coils (d-f), with the measured curves (a & d), Theoretical (b & e) and a comparison on a single cross section (c & f) for each set.

vibrating iron oxide sample was suitable for mapping out the response across the whole plane in both magnetic measurement directions (with the sample in a state of constant remanent magnetisation) by measuring the signal on the lock-in amplifier at each point in the plane.

For the in-plane sensitivity measurements, the sample was rastered across approximately 25 mm in the  $y$  direction, and approximately 10 mm in the  $x$  direction with the height held constant at the  $z = 0$  point of Figure 16. This is shown for both coil sets in Figure 15 parts (a) and (d) alongside the theoretical curves of (b) and (e), with a clear “saddle” shape being the overall dominant feature. This is expected and can be understood in the following way: for a single pick-up coil, the sensitivity reduces as approximately the cube of the distance to the sample. When the sample is between two similar coils, as shown in Figure 16,

the sensitivity curve along the coil axis has a minimum equidistant from their centres. As you move off the coil axis in the  $y$ -direction, the sensitivity reduces in accordance with equation (2) due to the increase in  $r$  as illustrated in Figure 16.

Figure 15 shows reasonable agreement between measured and theoretical sensitivity. As it was difficult to obtain accurate measurement for the coil dimensions due to them being contained in a plastic block, a fit through the saddle points in the centre of the coils systems was carried out which allowed the dimensions to vary within fixed

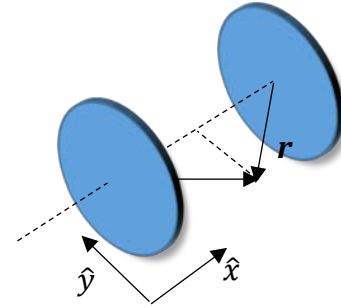


Figure 16 - Simple two coil system showing coil axis orientated in parallel-to-field direction

constraints. This is shown in parts (c) and (f), which is effectively a 2D slice of the surface maps across these points. These were then used to map out the theoretical 3d plots of parts (b) and (e). Further away from the centre of the surface the agreement becomes worse, with the expected sensitivity curves being flatter than those measured in parts (a) and (d). One unaccounted, but possible, cause is the presence of magnetic images in the electromagnet pole pieces. According to Bernards [59], this acts to increase the sensitivity,  $S_{wi}$ , at any point in the  $x$ - $y$  plane in comparison to the intrinsic sensitivity without images,  $S_i$ , such that  $S_{wi} = S_i(1 + \%S_i)$  where  $\%S_i$  is a fraction (less than 1) of the intrinsic sensitivity and which is given a value of around 30 % in his work. Hence, the absolute difference between any two points,  $\Delta S_{wi}$ , at say  $S_{wi}(x_1, y_1)$  and  $S_{wi}(x_2, y_2)$  will be greater than that for  $\Delta S_i$  of the intrinsic response at the same two points. This is consistent with our results, as it would cause the measured surface plots of (a) and (d) to be more curved (less flat) than those of (b) and (e) of the coils alone.

## **2.3. Precession and its reduction by modification to the UCLan VSM**

As a VSM utilises a long down rod to ensure that the vibrator head is removed from the magnetic field, misalignments will be projected down to the sample. If the sample is displaced from the axis of rotation it will describe a circle as it rotates, this is known as precession and is a major source of error in anisotropy measurements.

On the bi-axial vsm the down rod is 705 mm long, and so a misalignment of only  $0.65^\circ$  is enough to cause a precession of 8mm radius, larger than the diameter of the sample. To add further to this problem, the down rod is not ideally straight. This means to perfectly align the whole assembly is impractical.

### **2.3.1. Precession reduction methodology.**

Figure 17 (a) shows an ideal system with perfect alignment of a straight down-rod which has zero precession. Part (b) shows a system that has precession due to misalignment. Our method of reducing precession involved adding a micrometre controlled *x-y* stage to allow precision movement of the sample with respect to the rotational axis as shown schematically in Figure 18, positioning the sample closer to the rotational axis, effectively shifting the precession to the vibrator head at the top of the down rod as shown in Figure 17 (c).

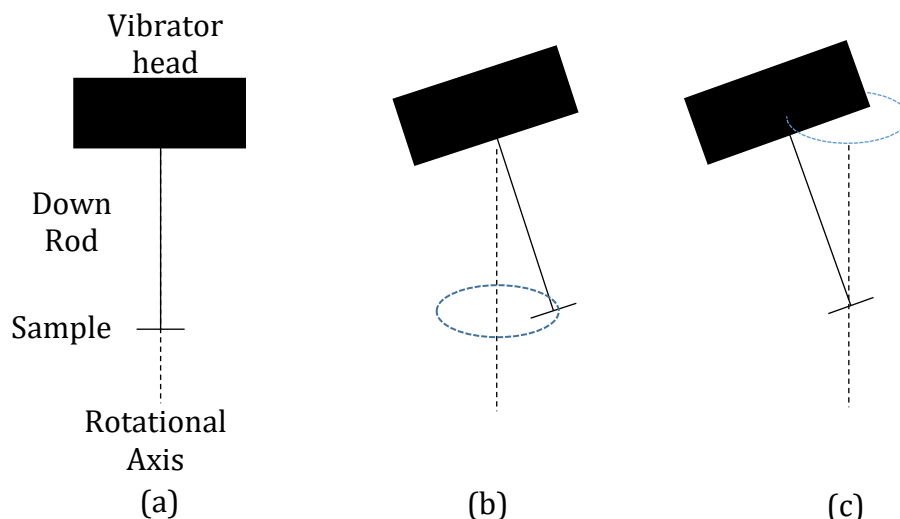


Figure 17 - Schematic demonstration of the method for reducing the precession of the sample during rotation. (a) Ideal arrangement, zero precession. (b) Misaligned sample with respect to the rotation axes, large precession. (c) Sample shifted into alignment with rotational axes, minimised precession.

In order to minimise precession, a method whereby it could be measured was developed first. This was achieved by affixing a drawing pin to the bottom of the down rod in the sample position. Positioning a piece of tinfoil on a board immediately below the tip of the pin and driving the Vibrator at a low frequency and a low amplitude caused the pin to mark the foil. Rotating then caused the pin to inscribe a circle on the foil which has a radius equal to the precessional radius. By changing the  $x$ -micrometre setting, repeating the process and determining the change in the precessional radius, the optimal setting for the  $x$ -micrometre could be found. The whole process was repeated for the  $y$ -micrometre. At the optimal settings the precessional radius was smaller than the diameter of the point of the pin.

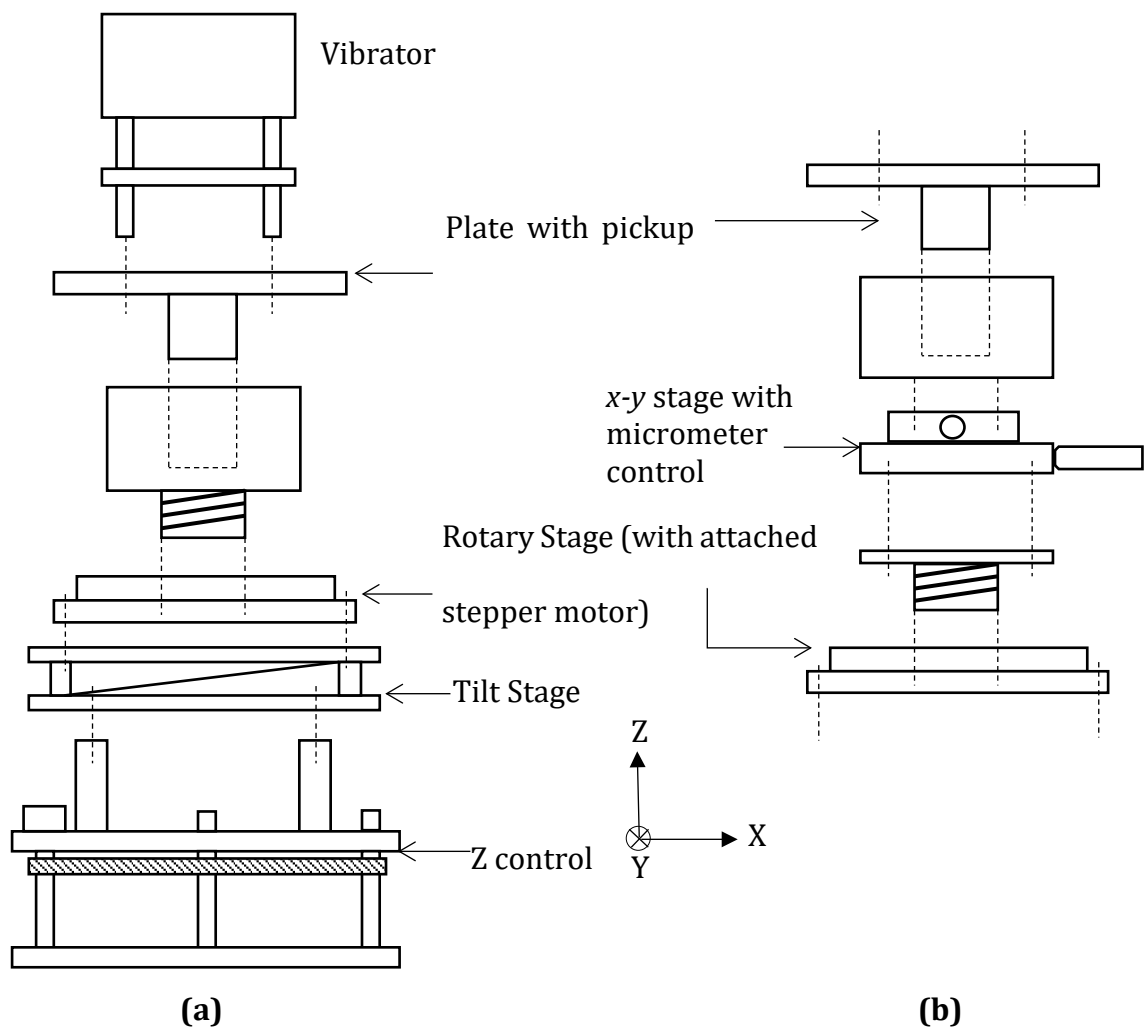


Figure 18 - Schematic showing the vibrator head assembly, (a) before modifications where made, and (b) after the x-y stage has been fitted to allow for precession reduction.

It is to be noted that in some cases this method of precession reduction is not suitable. Looking at Figure 17 (c) which shows the system in a precession-reduced state, it is clear that the sample is tilted and will therefore “wobble” as it is rotated. This should only be an issue for large samples, or if large corrections are required.

It is necessary to demonstrate that precession, and the “wobble” have minimal effect on the magnetisation measurements. This was done by rotating a hard

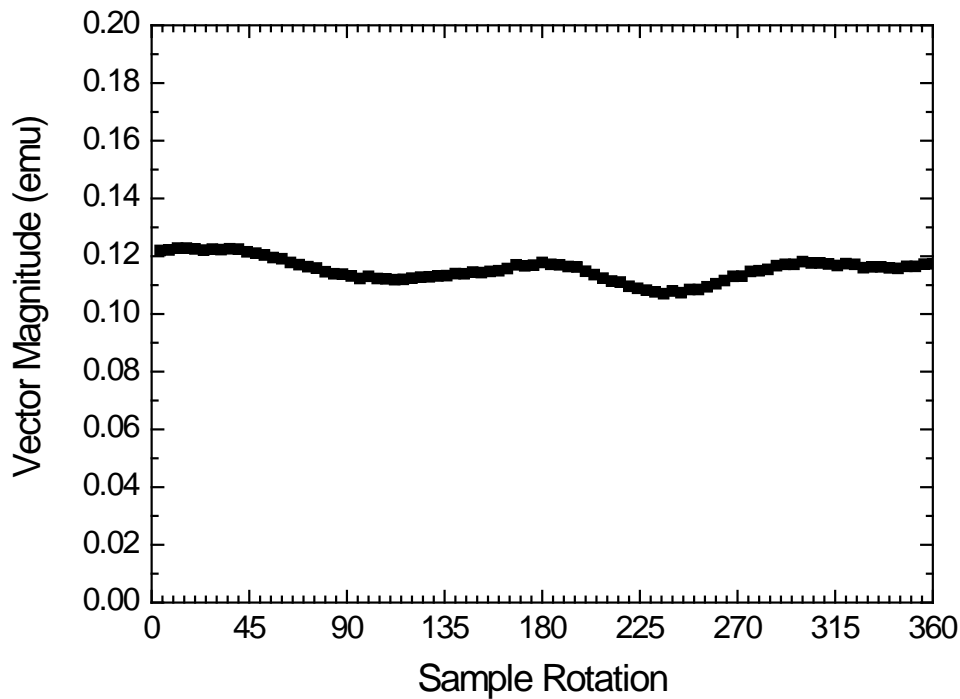


Figure 19 - Magnitude of the moment vector as a VHS tape sample is rotated. Showing reduced precessional effects.

remanent sample. The magnitude of the vector magnetisation should then remain constant as the sample is rotated. This is shown for a sample consisting of 6 layers of VHS tape in Figure 19. The mean value of this set of data is 0.115 emu with a standard deviation of 0.004 emu which means that any effects due to the precession of the sample have been reduced to less than 4%.

## 2.4. Experimental Control

The VSM is computer controlled utilising National Instruments' LABview virtual instrumentation suite. This allows instrument control, data input/output and data processing all to be performed from a custom-made user interface, such as the one shown in Figure 20. This is achieved by the use of "subVIs," small virtual instrument programs that can be combined to create the main virtual instrument.

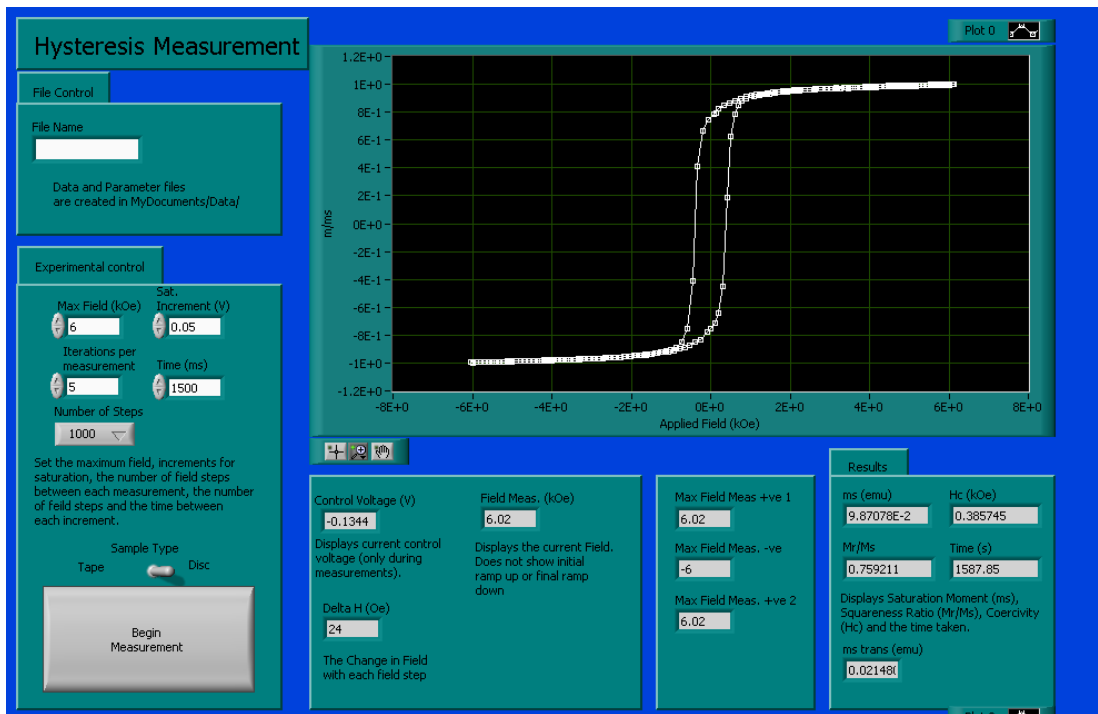


Figure 20 - Front Panel of the hysteresis routine developed in LABview. This is the main user-interface used for hysteresis measurements.

For full control of the VSM subVIs were required that allowed applied field control, sample rotation by stepper motor control and measurement of the sample moment and the applied field strength.

The field strength is measured using a Hirst GM05 gaussmeter with a resolution of 1 Oe which was calibrated using a permanent magnet and a zero-field chamber. The sample moment is measured as the induced voltage in the pick-up coils, by a Stanford Research Systems SR810 lock-in amplifier. Both the gaussmeter and the lock-in amplifier interface with the computer by means of standard RS232 serial communications. The signal from the lock-in is calibrated to units of emu using a nickel disc of known saturation moment. A further calibration step is needed as the sample holder exhibits a linear diamagnetic

response, which can be accounted for by applying a linear “baseline” correction to magnetic moment measurements.

The stepper motor is controlled via a specialist control board with USB-interface, and was supplied with LABview subVIs for ease of use. These were incorporated into the virtual instruments developed for this project.

## **2.5. Measurement Techniques**

The recommissioned bi-axial VSM was tested by performing well-known magnetic and magnetic anisotropy measurements, first on magnetically hard samples and then on soft samples more commensurate with the NFO/PZT samples. In this section, we introduce the standard magnetic hysteresis loop of hard materials as a way to define the most common characteristic parameters of magnetic materials. Methods of determining the distribution of easy axes in magnetically hard materials are applied to a well-known sample of uniaxial magnetic recording media. This allows us to demonstrate the reduced precession and the consistency of the vector measurements of the UCLan bi-axial VSM, and so gives confidence in the instrumentation as a whole. Finally we introduce indirect torque magnetometry, a method by which the anisotropy directions in magnetic materials can be determined using a bi-axial VSM, including an adapted methodology to reduce a known limitation of the measurement.

2.5.1. The Magnetic Hysteresis (M-H) loop

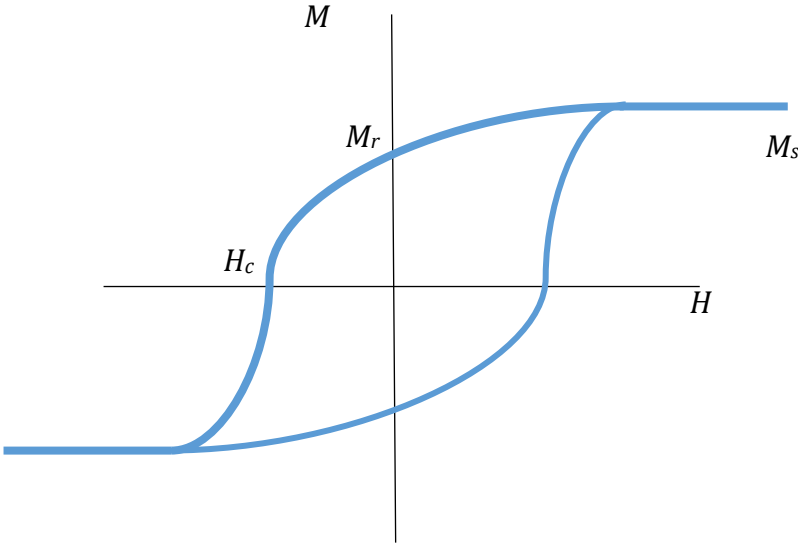


Figure 21 - A typical hysteresis loop for a hard sample, denoting saturation magnetisation,  $M_s$ , remanent magnetisation  $M_r$  and the coercivity  $H_c$

A common magnetic measurement technique, the  $M$ - $H$  loop, or Hysteresis loop, of a sample provides three key parameters for magnetic characterisation: The saturation moment,  $m_s$ , the remanent moment  $m_r$ , and the coercivity field  $H_c$ . The magnetic moment of a sample is dependent on the volume of the sample  $V$ , a more useful measure for the comparison of materials is the magnetisation  $M$ , defined as:

$$M = \frac{m}{V} \tag{2-3}$$

If we normalise the moment using the saturation moment, it can be seen that it is equal to the normalised magnetisation i.e.:

$$\frac{M}{M_s} = \frac{m}{m_s}. \quad (2-4)$$

A hysteresis loop is produced by applying a magnetic field large enough to saturate the sample, i.e. the moment is constant at  $m_s$  with respect to field, in the positive field direction. The field is then reduced slowly to zero and the moment is measured. If the sample is magnetically hard, at zero field the moment will not be zero; this is the remanent moment,  $m_r$ . As the field is increased in the negative field direction the moment will reduce to zero, the value of the field where this occurs is called the coercivity field  $H_c$ . The field is then increased until the sample is saturated, before being reduced and then increased in the positive direction to produce a full loop.

For distributions of uniaxial particles we can use the ratio of the remanent magnetisation and the saturation magnetisation, which is known as the squareness and is related to the degree of alignment in a particle distribution, with a squareness of 1 representing perfect alignment and a squareness of 0.5 being randomly orientated. This is a basic measurement of alignment. A more advanced method is used to determine the distribution of easy axes about the alignment direction and is described next.

### 2.5.2. Easy Axis Distribution Measurements

In any anisotropic sample, there will be a distribution of easy axis directions. This can be measured by the saturation remanence magnetisation, the magnetisation

when a sample has been placed in a saturating field and then the field reduced to zero, as a function of sample rotation. This is because a moment will lie along an easy axis direction when no field is applied. If a field is applied at an angle to the easy axis and then removed, the moment will relax into the nearest possible easy axis direction. If this direction is different from the original direction, the moment has “switched.” In this way, as the sample is rotated, saturated and returned to a remanent state, the magnitude of the vector remanent moment changes, and thus the rate of change with respect to angle of the vector remanence gives the Easy Axis Distribution or EAD.

In the case of particulate magnetic recording media an ideal sample would have single domain uniaxial particles of the same size, shape and material all perfectly aligned along the same single easy axis. This would result in a delta function at the point of alignment with the easy axis as all the particles would switch their magnetisation at this single point to align with the applied field, provided the field exceeds the switching field (which would be the same for all particles due to their uniformity of size and shape).

In reality, imperfect alignment of the particles causes there to be a distribution of the particulate easy axes about the ideal uniaxial direction, this will cause a spread in the function about this point. This is shown in Figure 22 for a VHS tape sample.

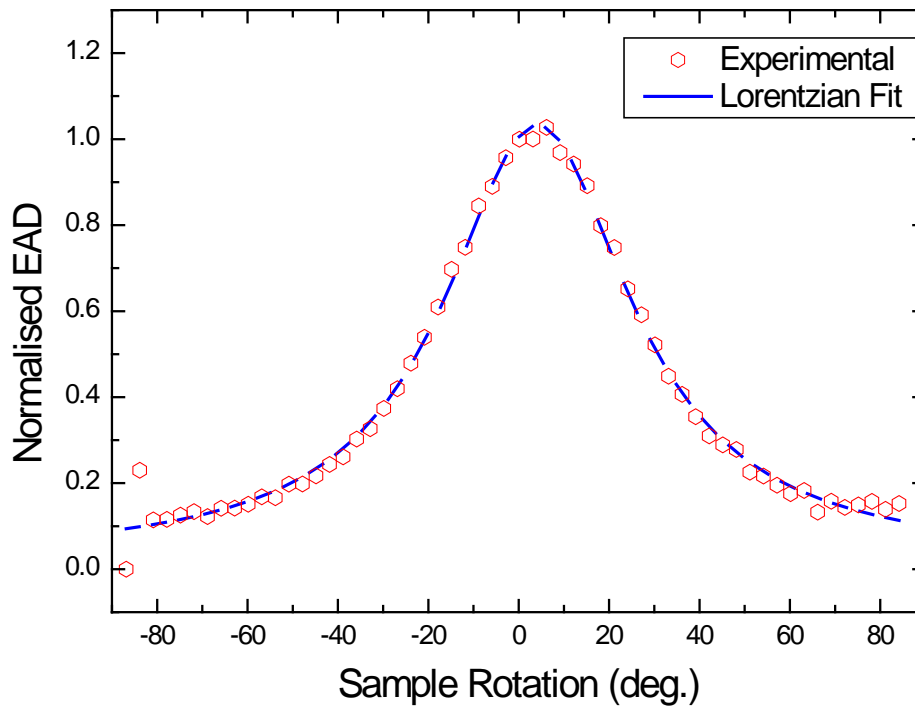


Figure 22 - Easy axis distribution measurement on a uniaxial VHS sample.

The vector remanence of the sample was measured by summing the parallel and transverse components in quadrature, as demonstrated originally by Schmidlin *et al.* [56] and can also be used for out-of-plane EAD measurements with small modifications to the procedure. Figure 22 shows a comparison for a uniaxial VHS tape sample, and a Lorentzian fit giving a FWHM of the measured EAD of  $40^\circ$  which is typical of the range seen in media of this type [56]. The symmetry of the EAD supports the successful reduction of precession in our measurement apparatus and gives confidence in the machine as a whole over a range of measurement techniques.

### 2.5.3. Torque Magnetometry using a Vibrating Sample Magnetometer

Conventionally performed with a specialised torque magnetometer, torque magnetometry is a powerful tool for anisotropy measurements [53]. Torque

magnetometry allows determination of the directions of the anisotropy axes of a sample, and their relative strengths, as well as determination of the anisotropy constants. It is possible to indirectly perform torque magnetometry using a biaxial VSM.

The torque due to the applied field,  $L_a$ , needed to rotate the saturation magnetisation,  $M_s$  away from an easy direction can be shown to be equal to:

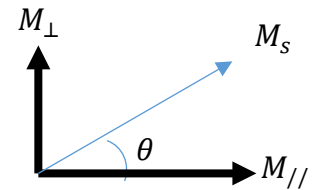


Figure 23 - The geometry of the biaxial measurement.

$$|L_a| = |M \times H_a| = M_s H_a \sin\theta \quad (2-5)$$

By considering the geometry of the Biaxial VSM measurement, as shown in Figure 23 it can be seen that:

$$|M_{\perp}| = |M_s| \sin\theta \quad (2-6)$$

Therefore:

$$L_a = M_{\perp} H_a \quad (2-7)$$

As this is the case, a torque curve can be measured using a biaxial vsm by rotating the sample in an applied dc field and measuring the transverse component of the

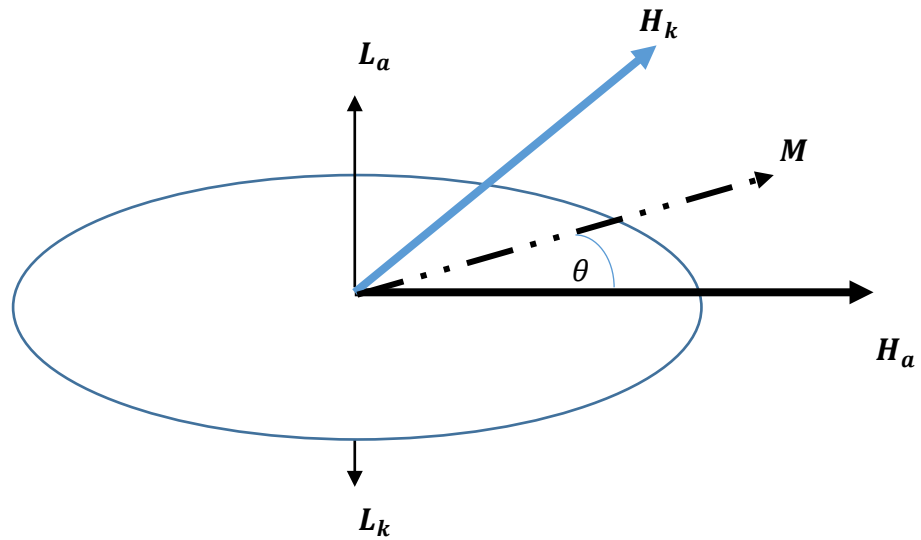


Figure 24 - Torques,  $L_a$  (due to an in-plane applied field  $H_a$ ) and  $L_k$  (due to the anisotropy field  $H_k$ ) acting on the magnetization vector  $M$ . As each torque is equal and opposite, the magnetization is in an equilibrium position.

magnetisation. This measured torque will be balanced by the torque due to the magnetic anisotropy, see Figure 24, such that the anisotropy directions in a sample can be determined from the measured torque curves.

There is a well known limitation of this methodology. As the applied field is increased such that the torque is greatest, the magnetic moment of the sample is pulled increasingly into the field direction. As this occurs it causes  $M_{\perp}$  to reduce toward zero [10].

An alternative methodology has been developed that involves repeat measurements at reducing fields to find the optimum measurement field. Figure 25 shows  $M_{\perp}$  as a function of angle for various fields. Through the new methodology it was determined that 800 Oe is the optimum field, and so has distinct crossing points and a large signal. As the field is increased to saturation

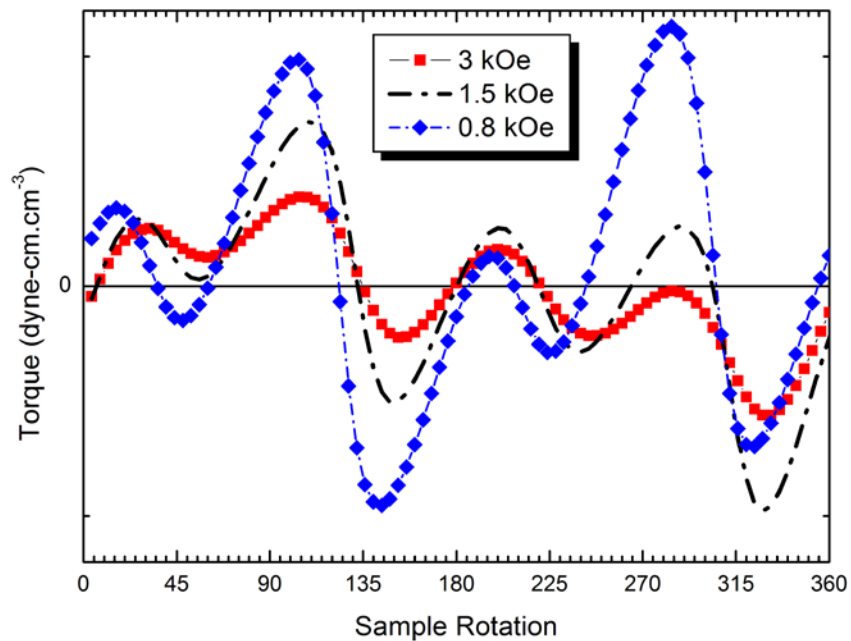


Figure 25 - Showing how  $M_{\perp}$  reduces at high fields.

the signal reduces and the crossing points become less distinguished and “washed-out.” This methodology will be discussed in detail in Chapter 3. Furthermore investigation of this new methodology led to the development of a new technique [61] that allows users with a standard (uniaxial) VSM to indirectly measure the torque due to an applied magnetic field and is also detailed in Chapter 3.

## 2.6. Development of a Magnetolectric Measurement Device

### 2.6.1. Requirements/Construction

ME measurements require the simultaneous application of DC and AC fields, and measurement of the piezoelectric voltage of the sample. To modify the VSM to achieve this would have required unacceptable risk to the delicate pick-up coil system by removing them to fit a Helmholtz pair. The pick-up coil itself was

proposed for the ac field generation however due to the push-pull nature of the coil system, any field induced by passing a current through the coils would result in opposing fields at the saddle-point so the field would be near-zero.

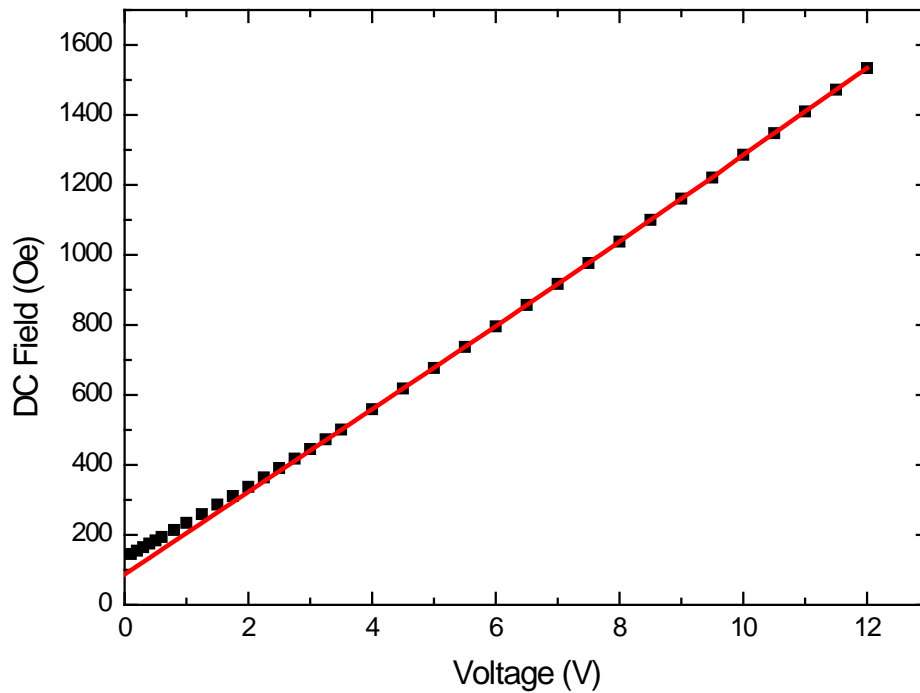


Figure 26 - DC field as a function of input voltage for the 4" Newport magnet

With the VSM being unsuitable for making ME measurements other options had to be considered with a Newport 4" magnet used for the DC field generation. The DC field profile as a function of input voltage is shown in Figure 26. The response is highly linear over a range of 0.5 to 1.5 kOe with a gradient of 122 Oe/V as shown by the linear regression. This means a constant input voltage step will result in a constant field step for measurements over this range. It is also seen that at low fields non-linearity occurs such that there is still a measurable magnetic field at zero applied voltage, this is a known effect due to the iron pole

pieces of the electromagnet not being perfectly soft. This means that the remanent magnetisation of the pole pieces generates a small magnetic field, in this case approximately 140 Oe. If zero field measurements are required a negative “correcting” field would need to be applied.

A pair of coils in a Helmholtz configuration are used to generate the AC field as shown in Figure 27, and are driven by an audio-amplified lock-in reference signal. These coils remain linear up to the 4 Oe required for the ME measurements as shown in Figure 28. The Helmholtz configuration provides a large region of uniform field [16] between a matched pair of coils. This AC field was measured using a search coil and a lock-in amplifier.

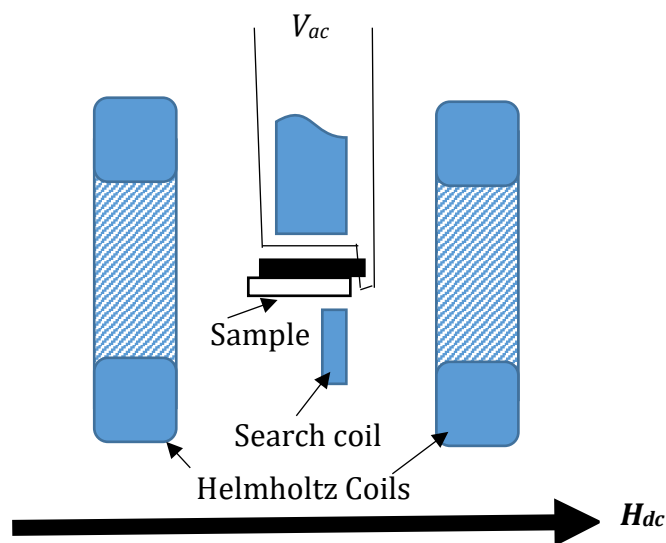


Figure 27 - Schematic of the ME rig showing the sample position, contact wires for measuring the piezoelectric response and the Helmholtz coils for producing the small ac magnetic field.

The output ME coupling signal is of the order of  $\mu V$ , and is measured directly from the electrical contacts on the sample by lock-in amplification.

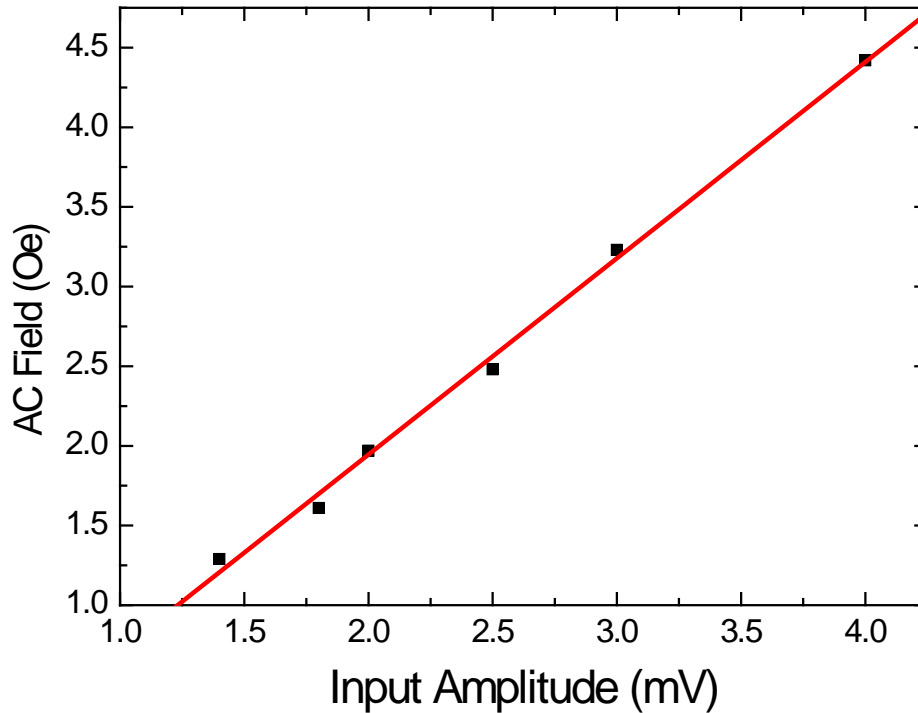


Figure 28 - AC Field as function of input amplitude for the helmholtz coils

A final requirement, due to needing ME measurements as a function of orientation to the anisotropy axes, is the rotation of the sample. A hand-driven rotational stage with a measurement resolution of  $0.5^\circ$  was used. Precession is less of an issue for this new rig than for the biaxial vsm as the sample rod is shorter (500 mm). Adjustment of the rotation head was sufficient to reduce precession to an acceptable level.

### 2.6.2. ME Coupling Measurements

Two measurements form the basis of the Direct ME characterisation of the NFO samples. As mentioned both an AC and DC magnetic field have to be applied to the sample. This gives us two independent variables. The ME coupling signal was

measured as a function of DC Field (ME response) and then as a function of AC field (ME Coupling Coefficient), with the other being held constant in each case. This was repeated at different angles to build up the anisotropic profile of both DC and AC response.

Figure 29 shows the typical ME response as a function of applied DC signal. At high fields when the sample is saturated the response is constant. The response generally initially increases as the field is reduced but can initially decrease

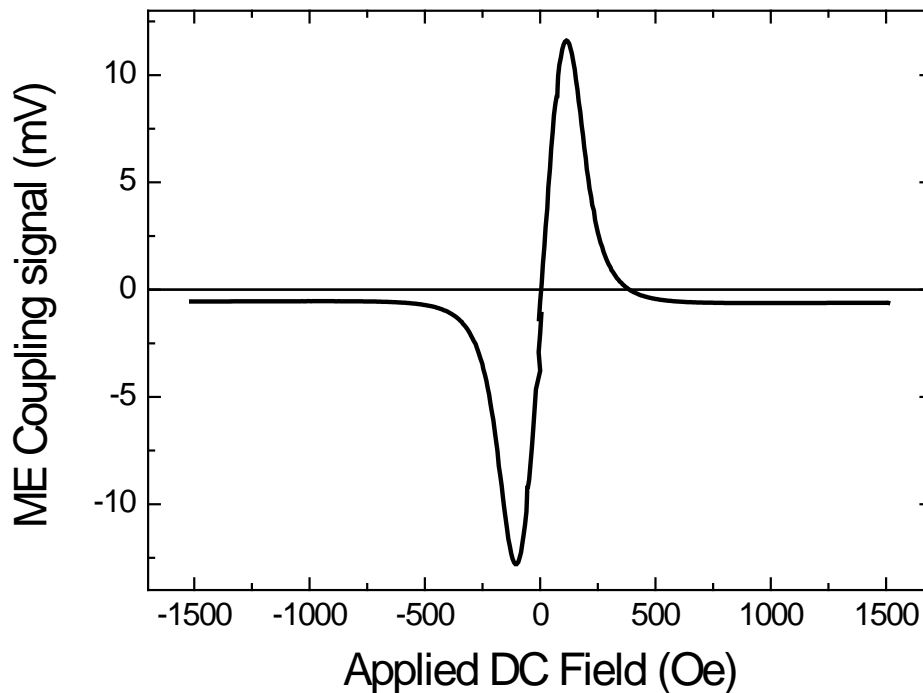
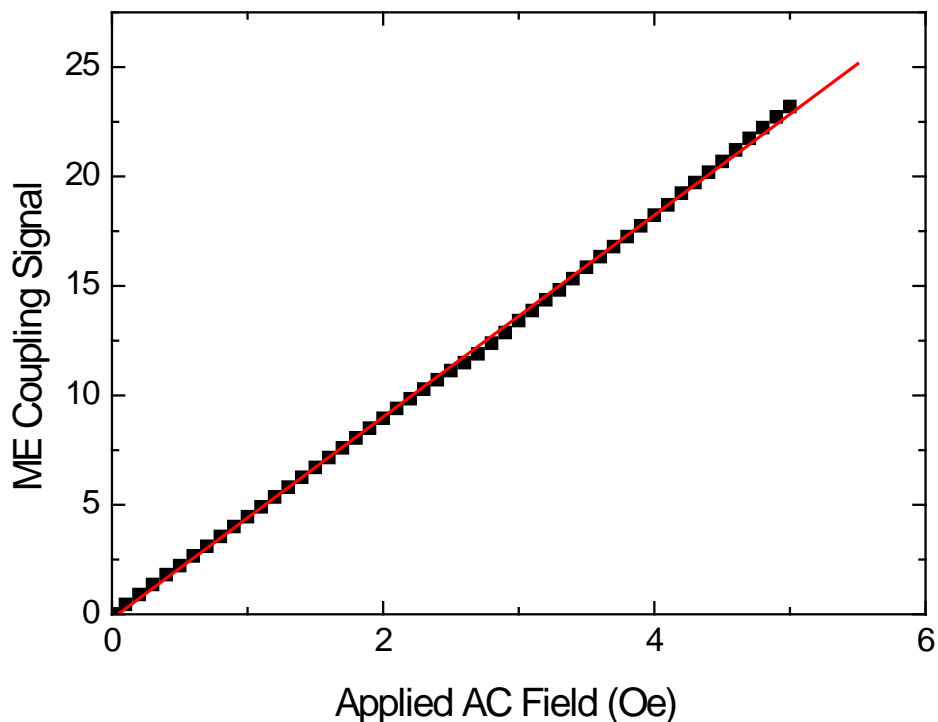


Figure 29 - Typical ME response as a function of applied DC magnetic field

slightly before increasing to a peak and then tending to zero at zero field. This results in there being an optimal DC-bias field, in Figure 29 this occurs at approximately 120 Oe for both positive and negative field directions (note the response generally has the same sign as the field).

It is important to note in Figure 29 that there is a systematic offset, shifting the response in the negative direction. The source of this could not be determined in the scope of this project, but the symmetry of the curve around the zero-field point suggests it is due to the experimental setup and is not intrinsic to the samples. In chapter 5 we will show that this offset is approximately constant with respect to the sample rotation, further evidence that it is not due to the sample. However it was not always possible to accurately determine the scale of this



*Figure 30 - Typical ME Coupling signal as a function of applied AC field.*

offset and so it has not been removed in the measurements detailed later.

The AC response is measured with the DC-applied field set to the optimum DC-bias field for that sample rotation, i.e the field at which the peak occurs in Figure 29. The AC field is increased from 0 at 0.1 Oe intervals up to a maximum field of

4 Oe. This response is expected to be linear, as shown in Figure 30 and the gradient is the linear ME coefficient  $\alpha$ .

In Chapter 4 the optimum DC-bias field, the ME response at this field (the peak signal) and the ME coefficient  $\alpha$ , are analysed in relation to the anisotropy axes via sample rotation.

### **3. Development of An Alternate Method of Simulating Torque Curves Using A Standard VSM.**

When characterising soft and hard magnetic materials, it is important to know the anisotropic characteristics of the sample and the direction of the anisotropy axes. Methods such as those developed by Barandiaran *et al.* [62], Dubuget *et al.* [63], Xue *et al.* [64], and Fan *et al.* [65] are only applicable to uniaxial anisotropies or require prior knowledge of the sample's anisotropy distribution.

Torque magnetometry is the traditional method for anisotropy measurements and directly measures the couple acting on a sample by an applied magnetic field. This is well documented in the literature. García *et al.* [66] utilised a modified Torque magnetometer to investigate the anisotropy of nanocrystalline Fe-Al alloys. An analogous method, also widely used, simulates torque magnetometry by using a bi-axial VSM to measure the in-plane transverse component of the magnetisation perpendicular to the applied field ( $M_{perp}$ ). Although either a dedicated torque magnetometer or a bi-axial VSM is available in many magnetics research laboratories, this is not always the case.

Here we describe a method we have developed in which torque magnetometry can be simulated using the in-plane magnetisation in the field direction ( $M_{//}$ ) obtained using a standard VSM with a rotating sample stage.

By considering the torque per unit volume,

$$\mathbf{L} = \mathbf{M} \times \mathbf{H} \quad (3-1)$$

of a sample of magnetization  $\mathbf{M}$  in an applied field of  $\mathbf{H}$ , the magnitude of  $\mathbf{L}$  is given as

$$L = MH \sin \phi \quad (3-2)$$

where  $\phi$  is the angle between the magnetisation and the applied field.

If we can measure  $M_{\perp}$  as in a biaxial VSM then,

$$M_{\perp} = M \sin \phi . \quad (3-3)$$

and:

$$L = M_{\perp} H. \quad (3-4)$$

Plotting this as a function of sample rotation simulates the torque curves directly.

Note that a standard VSM gives

$$M_{//} = M \cos \phi \quad (3-5)$$

and obtaining torque values from this will be returned to later.

A known limitation of the bi-axial method is that when maximum torque is achieved as a sample approaches saturation, then  $M_{\perp}$  is being reduced to a minimum as the vector sample moment  $\mathbf{m}$  is pulled completely into the field direction. For our soft samples, saturation occurs at approximately 1.5 kOe. To avoid this effect, the sample is saturated and then the field is reduced to a lower value before the torque curves are measured. By repeating this procedure at incrementally lower fields, a distinctive repeat pattern arises.

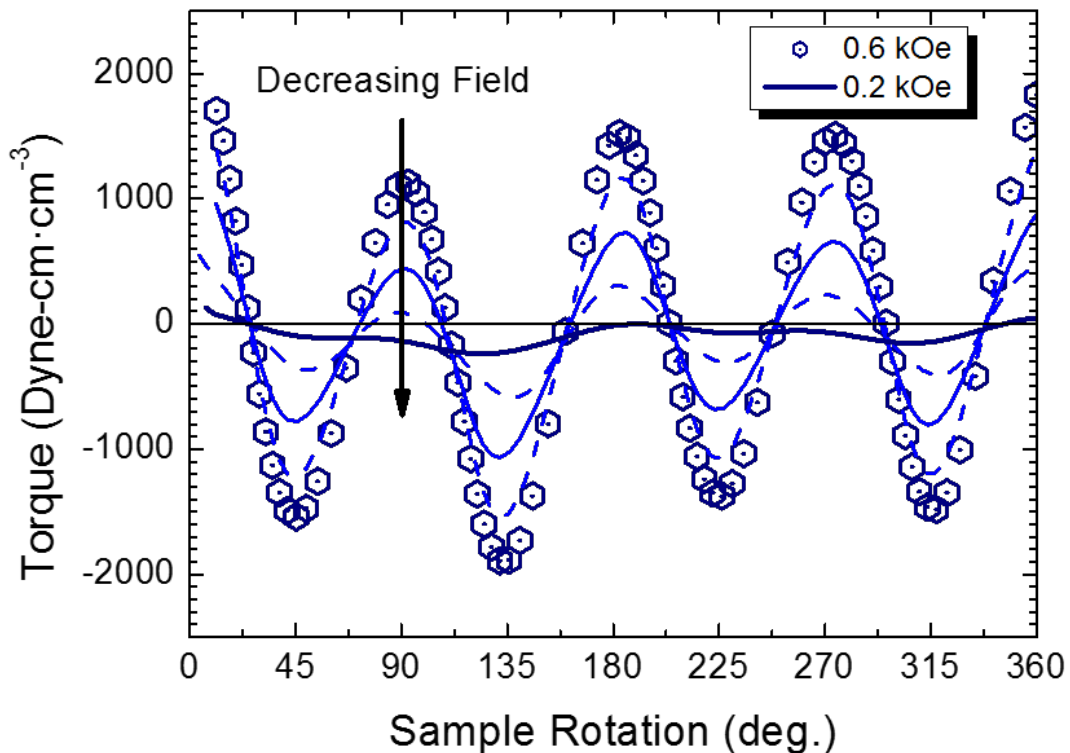


Figure 31 - Torque curves derived from the transverse magnetisation of the NFO\_100 sample. The sample is originally saturated before the field is reduced to the required value. A measurement of the moment is made every  $4^{\circ}$ . The intercepts with the abscissa with positive and negative gradients indicate the hard and medium axes of the sample, respectively. Each axis is separated from the previous by approximately  $45^{\circ}$  as expected from the theory. The field was decreased by 100 Oe between each measurement.

The NFO\_100 sample was initially saturated at 10 kOe for each curve prior to rotation in the non-saturating range of 0.6 - 0.2 kOe. From this a series of common intercepts with the abscissa is observed, with the crossing points that have positive gradient spaced  $90^\circ$  apart at  $68^\circ$ ,  $158^\circ$ ,  $248^\circ$ , and  $338^\circ$ , respectively. Likewise, a set of common intercepts with negative gradient are also spaced  $90^\circ$  apart, starting at  $23^\circ$  and leading to alternate negative and positive gradient intercepts spaced  $45^\circ$  apart. This is as expected for this crystallographic orientation, representing Medium  $\langle 110 \rangle$  and Hard  $\langle 100 \rangle$  directions respectively. In this case the Easy axes are all out of plane and so do not appear in the measurement.

It is to be noted that for these soft materials, where the magnetisation tends to zero at zero field, that the features in the torque curve flatten out and disappear as the torque also tends to zero. The 0.2 kOe curve in Figure 31 shows this happening.

The results for the NFO\_100 agree with what is expected from having a negative value of  $K_1$ , giving a biaxial disc consisting of 2 crystallographic medium directions  $\langle 110 \rangle$  and 2 crystallographic hard directions  $\langle 100 \rangle$  [17].

### 3.1. In-field Methodology Development

Consider first a saturated sample in a large applied field that is significantly above the switching field in any of the in-plane directions. If the sample is then rotated through a full 360°, the vector moment  $\mathbf{m}$  will always be switched along the in-field direction.

If the field is now reduced to some value below the upper limits of the switching field distribution and is rotated to an angle  $\theta$  with respect to the sample direction, the sample will now have a net vector moment that no longer lies parallel to the field direction. This is because  $\mathbf{m}$  now contains both switched and un-switched components and while the switched components rotate to remain parallel to the field direction, the un-switched stay aligned with the sample resulting in a net vector moment at an angle

$\phi$  to the field direction. Experimentally this is achieved by rotating the sample rather than the field in order to maintain the measurement geometry of the biaxial VSM

as shown in Figure 32.

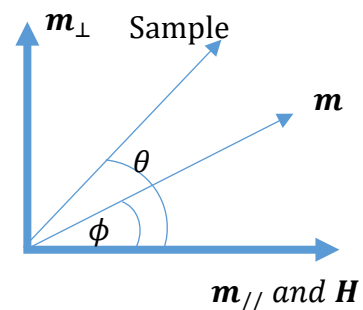


Figure 32 - Geometry of biaxial measurements, showing sample rotation angle  $\theta$ , and the magnetisation angle  $\phi$ .

From simple trigonometry and the magnitude of the moment  $m$  we know the transverse component of the moment  $m_{\perp}$  as shown in Figure 32 is

$$m_{\perp} = m \sin \phi \quad (3-6)$$

and that the parallel component is

$$m_{//} = m \cos \phi . \quad (3-7)$$

This suggests it is possible to derive the transverse moment needed for simulated torque curves from the in-field signal of a standard VSM, as

$$\frac{dm_{//}}{d\phi} = -m \sin \phi = -m_{\perp} . \quad (3-8)$$

However, this is only applicable if the angle  $\phi$  is known, which without a biaxial measurement is difficult to obtain.

We now consider the effects of the decreasing field method on our mixed system of switched and un-switched components. We assume that this is an assembly of anisotropic particles with a distribution of switching fields, such as that shown in Figure 33 (a), that are aligned along the various anisotropic axes of the sample.

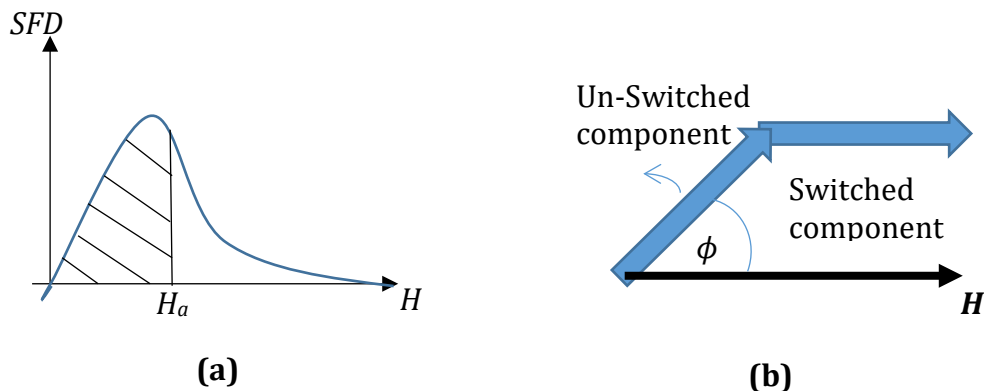


Figure 33 - **(a)** A schematic switching field distribution (SFD). When an applied field ( $H_a$ ) is applied any moment with a switching field less than  $H_a$  (shown as the shaded area) is considered “switched” and those with a greater switching field are considered “un-switched.” **(b)** How the switched and un-switched components interact with the field as the sample is rotated. The unswitched components rotate with the sample whilst the switched components remain in the direction of the applied field.

Starting from the limit of saturation, when all the particles are switched under rotation into the parallel direction of  $\phi = \text{zero}$ , the reduction of applied field leads to an increase in the un-switched particles shown as the unshaded region in Figure 33 (a) at the expense of the switched ones, the shaded region in Figure 33 (a). As the un-switched particle moments are not held in the parallel direction they begin to rotate with the sample as shown in Figure 33 (b) becoming ever more closely aligned with the sample rotation angle at each decreasing field step. The combination of the relative decrease in the parallel magnetization component at the same time as the increase in the rotational magnetisation component means that the vector moment ins now tending to the direction of  $\theta$ , such that  $\phi \rightarrow \theta$  as  $H \rightarrow \text{zero}$ , validating the use of (3-8) as a means of simulating torque curves by differentiation of the parallel signal used in standard VSM instruments.

It should be noted that for measurements on soft materials with negligible hysteresis,  $m \rightarrow 0$  as  $H \rightarrow 0$ , so the technique becomes limited at the small field end due to low magnetisation signal.

### **3.2. Testing of the Methodology Using In-Field Rotation Curves**

The results of applying the methodology to the in-field rotation curves of the NFO\_100 sample are shown in Figure 34. The curves compare well with those of the bi-axial method of Figure 31, reproducing all the essential features to show two sets of perpendicular bi-axial anisotropy directions  $45^\circ$  apart.

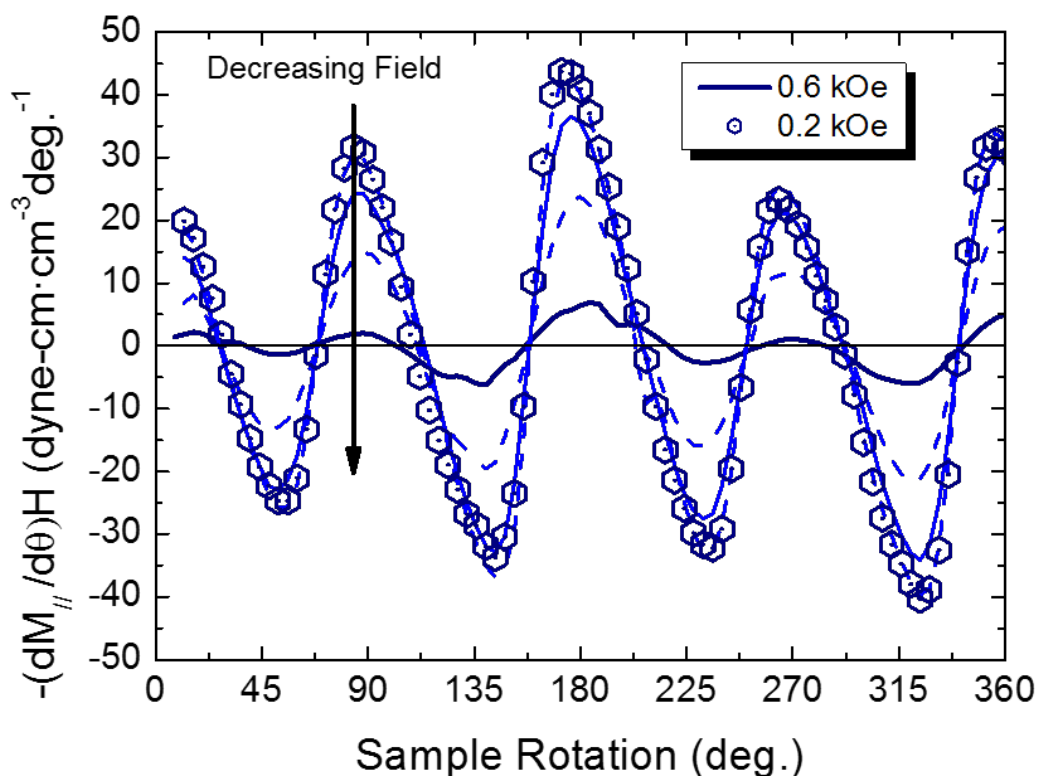


Figure 34 - Torque curves derived from the in-plane magnetisation of the NFO\_100 showing good agreement with the bi-axial method of Figure 29 for the position of the intercepts with the abscissa. This gives confidence in the new method as a means of identifying the anisotropy axes of a material. Note the loss of definition at small fields.

To further demonstrate the applicability of this method the NFO\_110 sample was investigated. The more complex anisotropy, consisting of 2 easy axes separated alternately by a medium and a hard axis, requires even more careful selection of fields to produce clear torque curves.

The in-field (parallel) curves of magnetisation as function of sample rotation are shown in Figure 35 for the NFO\_110 disc. As such, they can be thought of as the raw data that could be obtained from a standard VSM fitted with an inexpensive rotational stage. Repeating patterns can be observed, such as the two troughs of approximately the same depth at 158° and 338°, and the smaller troughs at

approximately 68° and 248°. Differentiating these curves give the results shown by data points in Figure 37. For comparison, the results of the bi-axial method are displayed as lines on the same plot. The two data sets compare well with the curves crossing the x-axis at the same points and with all the finer features of the bi-axial method, such as the relative amplitude of the peaks, apparent using the new methodology.

Again these crossing points show the positions of the anisotropy axes within the plane of the sample. In addition, inspection of the standard VSM data of Figure 35 shows the means of classifying their relative hardness or softness. This is due to the different saturating fields occurring at different sample orientations, as in Figure 36. For example, if the sample is orientated with an easy axis aligned with the field direction it will have a lower saturation field than a sample orientated

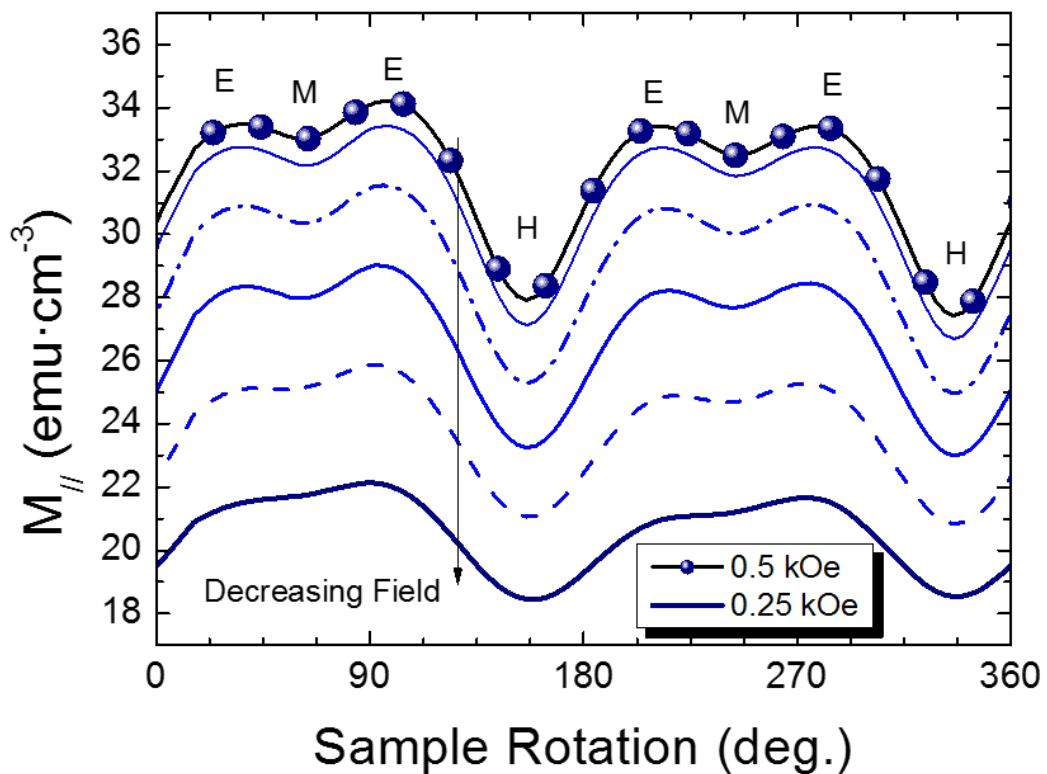


Figure 35 - In-field magnetisation as a function of sample rotation for the NFO\_110 sample. The sample is initially saturated before the field is reduced to the required value. The turning points are labelled E for easy axis, M for medium axis and H for hard axis.

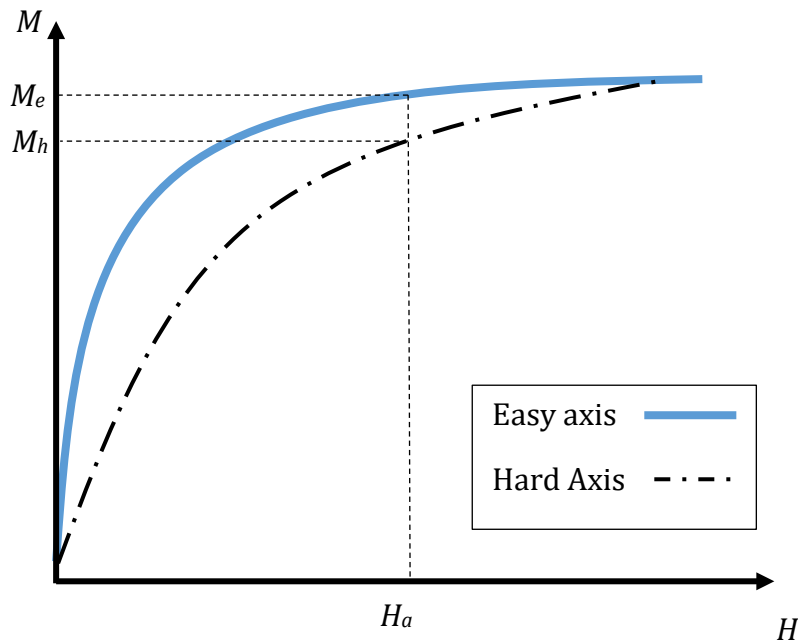


Figure 36 - Schematic representation of the M-H loops measured when the field is aligned along an easy (blue) and hard (black) axis. When the sample is rotated from an easy to a hard axis at a fixed field lower than saturation ( $H_a$ ) the magnetisation will change from  $M_e$  to  $M_h$ . This gives rise to the peaks and troughs in Figure 35.

in any other in-plane direction. Likewise, when the sample is orientated in a direction such that a Hard axis is aligned with the applied field the saturating field will be higher than for any other in-plane orientation. Hence, as our reducing field step methodology takes place below saturation, this ensures that for a given field ( $H_a$  in Figure 36) the easy axis magnetisation ( $M_e$  in Figure 36) is at a higher value than that of the harder axis ( $M_h$  in Figure 36). This is because the easy axis is closer to the saturation point at that field step when compared with that of the hard axis. This explains the behaviour seen in Figure 35 where the troughs represent relatively hard axes, with respect to their neighbouring axes, and the peaks represent relatively easy axes.

Application of this classification methodology to the data of Figure 35 shows that the easy axis peaks (marked E) occur at the same angles as four of the crossing

points of Figure 37 at around 34°, 98°, 210°, and 280°, with just the first one marked. It should be noted that the uncertainty in the positions is limited by the 4° resolution of the rotation steps used.

Also marked are the first of two medium and two hard axes, identified from the respective intermediate and low moment turning points in Figure 35 (marked M and H, respectively). For a cubic crystal orientated parallel to the {110} plane, these axes can be mapped to the <100>, <110> and <111> directions. Closer analysis of the anisotropy axes shows that the hard axes along <100> and the

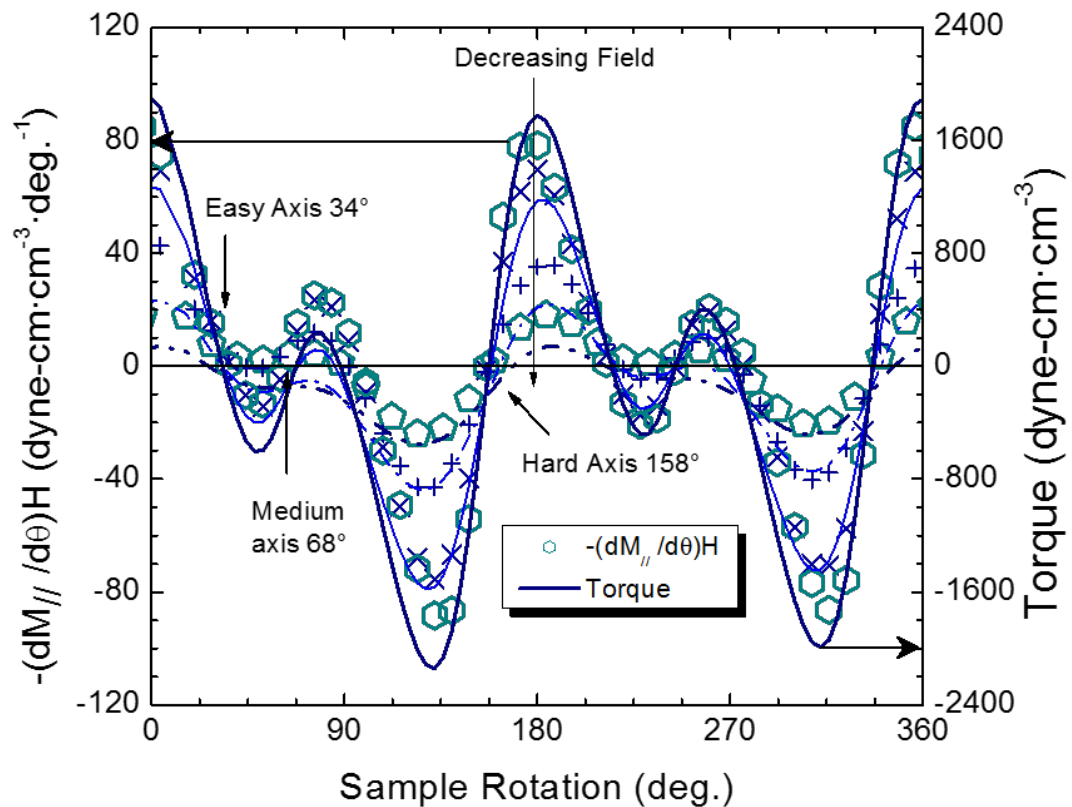


Figure 37 - Comparison of the in-field method (data points, which refer to the left axis) with the bi-axial VSM (Lines, which refer to the right axis) for the NFO\_110 sample. The good agreement of the intercepts with the abscissa and the relative amplitude of the peaks gives confidence in the applicability of the new method. The different symbols and line types represent measurements being taken at different applied field values, ranging from 0.25 kOe to 0.5 kOe.

medium axes along  $\langle 110 \rangle$  are spaced 90 degrees apart, but the easy axes along  $\langle 111 \rangle$  are not at  $45^\circ$  to either. This is consistent with an imperfect cubic lattice of slightly unequal lattice parameters that can sometimes be a result of strain in the texturing process of film growth.

It should be noted that a lower field-step increment of 40 Oe was needed for the NFO\_110 sample compared with the 100 Oe increment of the NFO\_100 sample of Figure 34. This was expected due to the more complex anisotropy of the  $\{100\}$  plane that requires the vector moment direction to be as close as possible to the sample rotation in order to generate the equivalent transverse moment response of the bi-axial method. Simply reducing the field to lower values to increase the number of un-switched components starts to have a negative effect in soft materials because of the drop off of the magnetisation signal toward zero at low fields. Hence, an optimum or sweet point needs to be found between these two factors when using the new methodology. Experimentally this was done by initially using the 100 Oe field step increments of the NFO\_100 sample over a wide range, this resulted in most of the curves failing to reproduce the results of the bi-axial method, often with crossing points being “washed-out.” Selecting a range of fields where these initial curves are smoothest and the features most consistent the measurements are repeated with a smaller, 40 Oe, field step increment over this smaller range. In the case of the NFO\_110 sample, this

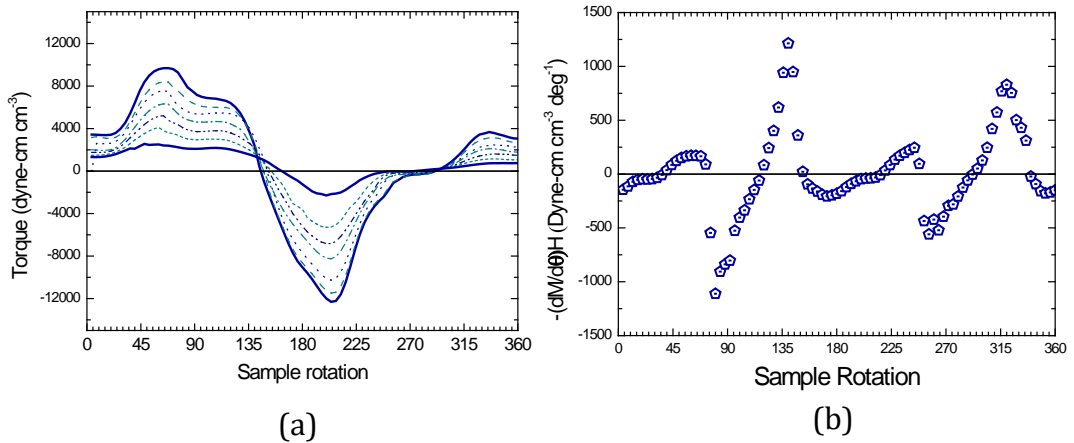


Figure 38 - Torque measurements on the NFO\_111 sample using (a) conventional transverse method and (b) the newly developed in-field method note the curve closest to the “sweet spot” is shown

occurred between 500 and 300 Oe. This methodology produced the smooth and consistent curves shown in Figure 37.

Figure 38 shows the results from applying these two methodologies to the NFO\_111 sample, which should be isotropic. In Figure 38 (a) shows a distinct crossing point at  $\sim 140^\circ$  suggesting some anisotropic behaviour although no features develop as the field is swept across the sweet spot. When the new methodology is applied, as in Figure 38 (b) some features appear although they are not as smooth as in the other cases. These suggest that the NFO\_111 sample exhibits some  $\{110\}$  like behaviour, evidenced by the large positive-gradient crossing points at  $\sim 125^\circ$  and  $\sim 300^\circ$  indicating “hard” axes, two smaller positive-gradient crossing points at  $\sim 30^\circ$  and  $\sim 210^\circ$  which indicate “medium” axes and four negative-gradient crossing points at  $\sim 75^\circ$ ,  $\sim 145^\circ$ ,  $\sim 245^\circ$  and  $\sim 335^\circ$ . These follow the easy-hard-easy-medium progression expected in a  $\{110\}$  disc and are possibly due to misalignment of the crystallographic texture in the sample. However except for the medium axes these should not be the crystallographic

anisotropy axes and are merely the directions in this sample in which the anisotropy energy is most extreme.

In the next chapter we will discuss the micromagnetic modelling of our samples, in particular we focus on the anisotropy energy and how it relates to the torque curves.

## 4. Micromagnetic Modelling

Micromagnetics is a continuum phenomenological model of magnetisation dynamics in magnetic materials with a length scale of a few nanometres up to micrometres [67]. A large range of interactions can be incorporated within micromagnetic models by calculating effective fields from new energy terms, including Zeeman energy, magnetostatic energy, various types of exchange energy, magnetocrystalline anisotropy, and magnetoelastic energy. Static magnetisation can also be reproduced by finding local minima in the total energy landscape as well as reproducing the shape of magnetic hysteresis loops.

### 4.1. Magnetic Moment from Angular Momentum

It is convenient to define the magnetic moment in terms of the angular momentum of electrons in an atom:

$$\boldsymbol{\mu} = \gamma \mathbf{L}, \quad (4-1)$$

here  $\gamma$  is the gyromagnetic ratio and  $\mathbf{L}$  is the orbital angular momentum of the electron

### 4.2. Bohr Magneton and Gyromagnetic Ratio

Classically the angular momentum of the electron is given by  $\mathbf{L} = m_e \mathbf{v} r$ , where  $m_e$  is the mass of the electron,  $\mathbf{v}$  is its linear velocity and  $r$  the orbit radius. In atoms the angular momentum is quantized as  $L = n\hbar$ , where  $n$  is a natural number and  $\hbar$  is the reduced Planck's constant. For the lowest orbit we have:

$$\mu = IS = \pi r^2 I = \gamma \hbar = \gamma m_e v r \quad (4-2)$$

$$I = -\frac{ev}{2\pi r} \quad (4-3)$$

Where  $e$  is the magnitude of the electron charge. Here  $I$  and  $S$  represent the current, and the area enclosed by a circular current loop, which in this case consists of an electron in a circular orbit.

Substituting:

$$\mu = -\frac{evr}{2} = \gamma \hbar = \gamma m_e v r$$

And so:

$$\gamma = -\frac{e}{2m_e} \quad (4-4)$$

$$\mu = -\frac{e\hbar}{2m_e} = -\mu_B \quad (4-5)$$

Where  $\mu_B$  is known as the Bohr magneton.

### 4.3. Magnetic Moment of an Isolated Electron

Electrons have an intrinsic magnetic moment due to the spin angular momentum:

$$\mu_e = \gamma_e S \quad (4-6)$$

Where  $S$  is the electron's spin and  $\gamma_e$  is the electron's gyromagnetic ratio, which includes additional relativistic and quantum field theory corrections, given by Landé's g-factor (which for an electron is approximately 2 [68]),

$$\gamma_e = -\frac{ge}{2m_e} \cong -\frac{e}{m_e} \quad (4-7)$$

The spin observable has two eigenstates. If the wave function collapses into either eigenstate, we can then speak of a definite magnetic moment:

$$\mu_e = \mp \frac{ge\hbar}{4m_e}$$
$$|\mu_e| \cong \mu_B \quad (4-8)$$

### 4.4. Precession and Continuum Magnetisation

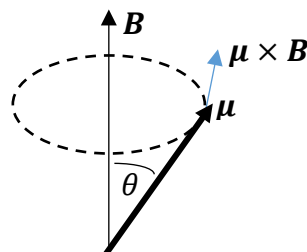


Figure 39 - Precession of the magnetic moment  $\mu$  around the magnetic field  $B$

Let us consider the interaction between a magnetic moment originating from an angular momentum as shown in Figure 39. The magnetic field exerts a torque on the magnetic moment, which also equals the rate of change of angular momentum:

$$\mathbf{G} = \boldsymbol{\mu} \times \mathbf{B} = \frac{d\mathbf{L}}{dt} \quad (4-9)$$

From (4-1)

$$\frac{d\boldsymbol{\mu}}{dt} = \gamma \boldsymbol{\mu} \times \mathbf{B} \quad (4-10)$$

This set of differential equations can be solved to obtain:

$$\mu_x(t) = |\boldsymbol{\mu}| \sin(\theta) \sin(\omega_L t)$$

$$\mu_y(t) = |\boldsymbol{\mu}| \sin(\theta) \cos(\omega_L t)$$

$$\mu_z(t) = |\boldsymbol{\mu}| \cos(\theta)$$

Here  $\theta$  is defined as shown in Figure 39 and  $\omega_L$  is the angular precession frequency, called the Larmor precession frequency given by:

$$\omega_L = \gamma B$$

In materials where we have a strong correlation between individual magnetic moments the expectation value of magnetic moment varies on a scale much larger than the crystal lattice scale we can speak of a continuous spatially varying magnetic moment function  $\boldsymbol{\mu}(x, y, z)$ , where the value at a given point arises from

a local average. The magnetisation is defined as the volume density of the magnetic moments or:

$$\mathbf{M}(x, y, z) = \frac{\boldsymbol{\mu}(x, y, z)}{V} \quad (4-11)$$

And so:

$$\frac{\partial \mathbf{M}}{\partial t} = \gamma \mathbf{M} \times \mathbf{B} \quad (4-12)$$

#### 4.5. Landau-Lifshitz Equation

Until this point, we have assumed that the energy remains constant. In real magnetic materials the potential energy is dissipated/transferred through various relaxation mechanisms resulting in an effect known as magnetisation damping. As this potential energy lowers, the angle between the magnetic moment and the magnetic field direction is constantly reduced until the two line up thus the magnetic moment undergoes a damped precessional motion, spiralling toward the magnetic field direction. The magnetisation damping can

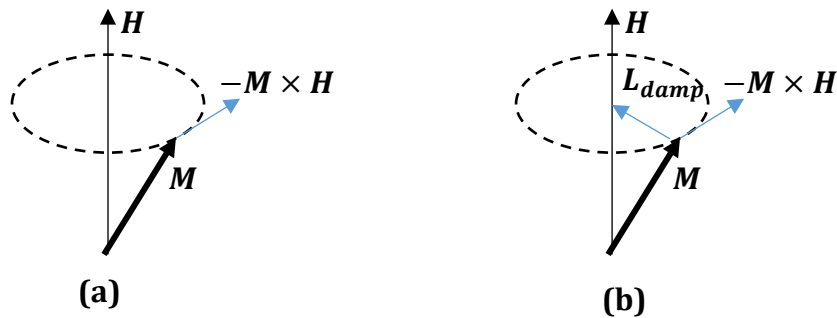


Figure 40 - (a) loss-less precession of magnetisation around a magnetic field. (b) damped precession around a magnetic field, showing damping torque ( $\mathbf{L}_{damp}$ ) direction.

be modelled as an additional torque term perpendicular to the field torque and the magnetic moment.

One possibility is to have a damping torque term of the form  $\mathbf{L}_{damp} = \mathbf{M} \times (\mathbf{M} \times \mathbf{B})$  which is perpendicular to both  $\mathbf{M}$  and  $\mathbf{M} \times \mathbf{H}$  as in Figure 40 (b), introduced by using a phenomenological damping constant,  $\lambda > 0$  known as the Landau-Lifshitz damping constant. This results in the Landau-Lifshitz equation:

$$\frac{1}{\mu_0} \frac{\partial \mathbf{M}}{\partial t} = \gamma_e \mathbf{M} \times \mathbf{H} - \frac{\lambda}{|\mathbf{M}|} \mathbf{M} \times (\mathbf{M} \times \mathbf{H}) \quad (4-13)$$

Where we have used  $\mathbf{B} = \mu_0 \mathbf{H}$ .

While this represents a damped precessional moment, as  $\lambda$  becomes very large the rate of change of the magnetic moment also tends to infinity. Since the damping arises due to a transfer of energy this is not as expected.

#### 4.6. Landau-Lifshitz-Gilbert Equation

Instead we use a damping term of the form  $\mathbf{M} \times \partial \mathbf{M} / \partial t$  [69] since this is also perpendicular to both  $\mathbf{M}$  and the precessional torque, as  $\frac{\partial \mathbf{M}}{\partial t} = \gamma \mathbf{M} \times \mathbf{B}$ . In this way we get:

$$\frac{1}{\mu_0} \frac{\partial \mathbf{M}}{\partial t} = \gamma_e \mathbf{M} \times \mathbf{H} + \frac{\alpha}{\mu |\mathbf{M}|} \mathbf{M} \times \frac{\partial \mathbf{M}}{\partial t} \quad (4-14)$$

This is known as the Landau-Lifshitz-Gilbert equation. The Gilbert damping term  $\alpha > 0$ , a dimensionless constant, has been introduced. Note that:

$$\mathbf{M} \cdot \frac{\partial \mathbf{M}}{\partial t} = 0 \quad (4-15)$$

We can then rearrange (4-14) to get:

$$\frac{1}{\mu_0} \frac{\partial \mathbf{M}}{\partial t} = \frac{\gamma_e}{1 + \alpha^2} \mathbf{M} \times \mathbf{H} + \frac{\alpha \gamma_e}{1 + \alpha^2} \frac{1}{|\mathbf{M}|} \mathbf{M} \times (\mathbf{M} \times \mathbf{H})$$

By substituting  $\mathbf{m} = \frac{\mathbf{M}}{|\mathbf{M}|}$  we obtain:

$$\frac{1}{\mu_0} \frac{\partial \mathbf{m}}{\partial t} = \frac{\gamma_e}{1 + \alpha^2} \mathbf{m} \times \mathbf{H} + \frac{\alpha \gamma_e}{1 + \alpha^2} \mathbf{m} \times (\mathbf{m} \times \mathbf{H}) \quad (4-16)$$

The limitations of the LLG come from the fact that we have assumed a constant magnitude of  $\mathbf{m}$ , it is possible to relax this restriction enabling consideration of non-saturated materials and thermal effects. This is achieved by including a longitudinal damping torque in addition to the transverse damping torque. This has the effect of making the magnetisation length non-constant. In this way the magnetisation dynamics are then described by the Landau-Lifshitz-Bloch equation as shown in [70].

## 4.7. Effective Field Contributions

So far, we have only considered applied, or external, fields. However, it is easy to model internal interactions as effective fields acting on the magnetic moments.  $\mathbf{H}$  is now defined by four main components:

1. Zeeman (applied field,  $\mathbf{H}_a$ )
2. Magnetostatic (demagnetising field,  $\mathbf{H}_d$ )
3. Direct Exchange (exchange field,  $\mathbf{H}_{ex}$ )
4. Magnetocrystalline Anisotropy (anisotropy field,  $\mathbf{H}_k$ )
5. Magnetoelastic (Strain anisotropy  $\mathbf{H}_\lambda$ )

The Zeeman term refers to the applied field,  $H_a$  and is defined by the program. The exact manner in which these fields are incorporated into the program will be detailed later.

### 4.7.1. Magnetostatic Term

Magnetic dipoles interact through the dipole-dipole or dipolar, interaction with energy given by:

$$E = \frac{\mu_0}{4\pi r^3} \left[ \boldsymbol{\mu}_1 \cdot \boldsymbol{\mu}_2 - \frac{3}{r^2} (\boldsymbol{\mu}_1 \cdot \mathbf{r})(\boldsymbol{\mu}_2 \cdot \mathbf{r}) \right] \quad (4-17)$$

Here  $\boldsymbol{\mu}_1$  and  $\boldsymbol{\mu}_2$  are two magnetic moments separated by the distance  $\mathbf{r}$ . This interaction tend to align magnetic dipoles parallel or anti-parallel to each other, forming a flux-closure state, thus avoiding free poles. In a magnetic material the dipolar interaction results in a demagnetising field which is orientated in the

opposite direction to the magnetisation of the material. The magnetostatic energy is given by:

$$E_d = -\frac{\mu_0}{2} \iiint \mathbf{M} \cdot \mathbf{H}_d dV \quad (4-18)$$

In general, the demagnetising field,  $\mathbf{H}_d$  depends on the shape of the material and is described by the demagnetising tensor  $\mathbf{N}$  [71] as:

$$\mathbf{H}_d = -\mathbf{N}\mathbf{M} \quad (4-19)$$

The demagnetising tensor is derived by the method of Newell [72], which in general has the form:

$$\mathbf{N} = \begin{pmatrix} N_{xx} & N_{xy} & N_{xz} \\ N_{xy} & N_{yy} & N_{yz} \\ N_{xz} & N_{yz} & N_{zz} \end{pmatrix}. \quad (4-20)$$

#### 4.7.2. Direct Exchange

The exchange interactions between electrons, either within the same atom or with those in neighbouring atoms, is of great importance for micromagnetic modelling. The simplest form is the direct exchange between two electrons with no intermediaries. The direct exchange energy density is given as:

$$\epsilon_{ex} = A \left[ \left( \frac{\partial \mathbf{m}^2}{\partial x} \right) + \left( \frac{\partial \mathbf{m}^2}{\partial y} \right) + \left( \frac{\partial \mathbf{m}^2}{\partial z} \right) \right] \quad (4-21)$$

Where  $A$  is the exchange stiffness, a characteristic parameter of the material. This energy density can be expressed as a magnetic field:

$$\mathbf{H}_{ex} = \frac{2A}{\mu_0 M_s} \nabla \mathbf{m}^2 \quad (4-22)$$

This gives rise to another property, the exchange size  $l_{ex}$  below which the magnetization does not vary typically significantly and is given by:

$$l_{ex} = \sqrt{\frac{2A}{\mu_0 M_s^2}} \quad (4-23)$$

It is conventional to use this value as the lower limit for the cell-size in micromagnetic modelling. If the cell-size is significantly larger than the exchange length the simulation will be inaccurate, however cell-sizes below the exchange length increase the computational cost without increasing the accuracy.

### 4.7.3. Magnetocrystalline Anisotropy

#### 4.7.3.1. Uniaxial Anisotropy

Uniaxial anisotropy is the simplest type of magnetocrystalline anisotropy and it is characterised by a single rotation symmetry axis. The magnetocrystalline

anisotropy has the effect of pulling the magnetisation into an easy axis direction. This means the magnetocrystalline anisotropy can be modelled as a magnetic field.

The anisotropy energy is given by:

$$\epsilon_k = K_0 + K_u \sin^2 \theta$$

Here  $K_u$  is the uniaxial anisotropy constant and  $\theta$  is the angle between the magnetisation and the symmetry axis and its sign designates whether the symmetry direction is an easy or hard direction.

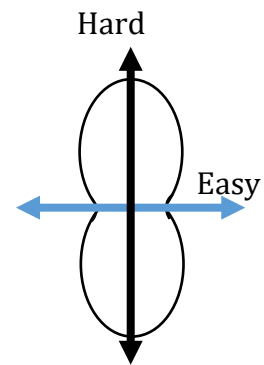


Figure 41 - Schematic of the in-plane uniaxial anisotropy energy, with the easy and hard axes highlighted

The energy minima are found by solving the following conditions:

$$\frac{\partial \epsilon_{An}}{\partial \theta} = 0 \text{ and } \frac{\partial^2 \epsilon_{An}}{\partial \theta^2} > 0$$

Thus for  $K_u > 0$ , we obtain  $\theta = 0, \pi$ , so the symmetry axis is an energy minimum and thus an easy axis and for  $K_u < 0$  the symmetry axis is a hard axis.

We can describe this in terms of an anisotropy field as:

$$\mathbf{H}_k = -\frac{1}{\mu_0 M_s} \frac{\partial \epsilon}{\partial \mathbf{m}}$$

$$H_k = \frac{2K_u}{\mu_0 M_s} \quad (4-24)$$

In this case the field acts along the symmetry axis.

#### 4.7.3.2. Cubic Anisotropy

We are concerned, not with uniaxial anisotropy, but with cubic anisotropy. Cubic anisotropy is characterised by 4-fold rotational symmetry about 3 orthogonal axes. The energy density in this case is given by:

$$\epsilon_k = K_0 + K_1[\alpha^2\beta^2 + \alpha^2\gamma^2 + \beta^2\gamma^2] + K_2\alpha^2\beta^2\gamma^2$$

Here  $K_1$  and  $K_2$  are the cubic anisotropy constants and  $\alpha, \beta, \gamma$  are the direction cosines [10]. With  $\theta$  and  $\phi$  being the polar and azimuthal angle respectively these can be written:

$$\alpha = \sin(\theta) \cos(\phi)$$

$$\beta = \sin(\theta) \sin(\phi)$$

$$\gamma = \cos(\theta)$$

Considering only the energy density in the x-y plane, with  $\theta = \frac{\pi}{2}$ , we get the special case where  $\alpha = \cos(\phi)$ ,  $\beta = \sin(\phi)$ ,  $\gamma = 0$  and so:

$$\epsilon_k = K_0 + K_1 \sin^2(\phi) \cos^2(\phi)$$

If  $K_1 > 0$ , for  $\phi = 0, \frac{\pi}{2}, \pi, \frac{3\pi}{2}$  we have energy minima, thus we have 2 orthogonal easy axes in the x-y plane. For  $K_1 < 0$  the orthogonal easy axes are rotated by  $\frac{\pi}{4}$  radians.

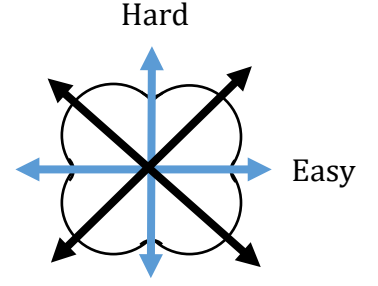


Figure 42 - Schematic representation of the cubic anisotropy energy in the x-y plane, showing the biaxial nature of this plane. The Easy and Hard axes marked are for this plane.

As before, we can derive an anisotropy field, which for the case with  $\langle 111 \rangle$  easy directions we get:

$$H_k = \frac{-4(3K_1 + K_2)}{9\mu_0 M_s} \quad (4-25)$$

In our simulations of NFO samples this is the value used for the anisotropy field.

#### 4.7.4. The Magnetoelastic Effect

The Magnetoelastic effect is the inverse of magnetostriction, where an applied strain alters the magnetic properties of a material. The magnetoelastic energy is given by:

$$\epsilon_\lambda = -\frac{3}{2}\lambda\sigma(\alpha_1^2\gamma_1^2 + \alpha_2^2\gamma_2^2 + \alpha_3^2\gamma_3^2)$$

Where  $\lambda$  is the material's magnetostriction,  $\sigma$  is magnitude of the applied stress,  $\gamma_1, \gamma_2$  and  $\gamma_3$  are the direction cosines of this stress and  $\alpha_1, \alpha_2$  and  $\alpha_3$  are the direction cosines of the magnetisation [17]. This can be expressed as a magnetic field:

$$H_\lambda = \frac{1}{\mu_0 M_s} \frac{\partial \epsilon_\lambda}{\partial \mathbf{m}}$$

As  $m_x = \alpha_1$ ,  $m_y = \alpha_2$  and  $m_z = \alpha_3$ , we can write:

$$H_\lambda = \frac{3\lambda\sigma}{\mu_0 M_s} (\hat{x}m_x\gamma_1^2 + \hat{y}m_y\gamma_2^2 + \hat{z}m_z\gamma_3^2) \quad (4-26)$$

#### 4.8. Micromagnetic Modelling Software – Boris

The software used to perform the micromagnetic modelling in this project is Boris, developed by Serban Lepadatu, a screenshot of the main interface is shown in Figure 43. It is a command-line driven program with a modular design that allows interactions to be included or excluded as required. The available

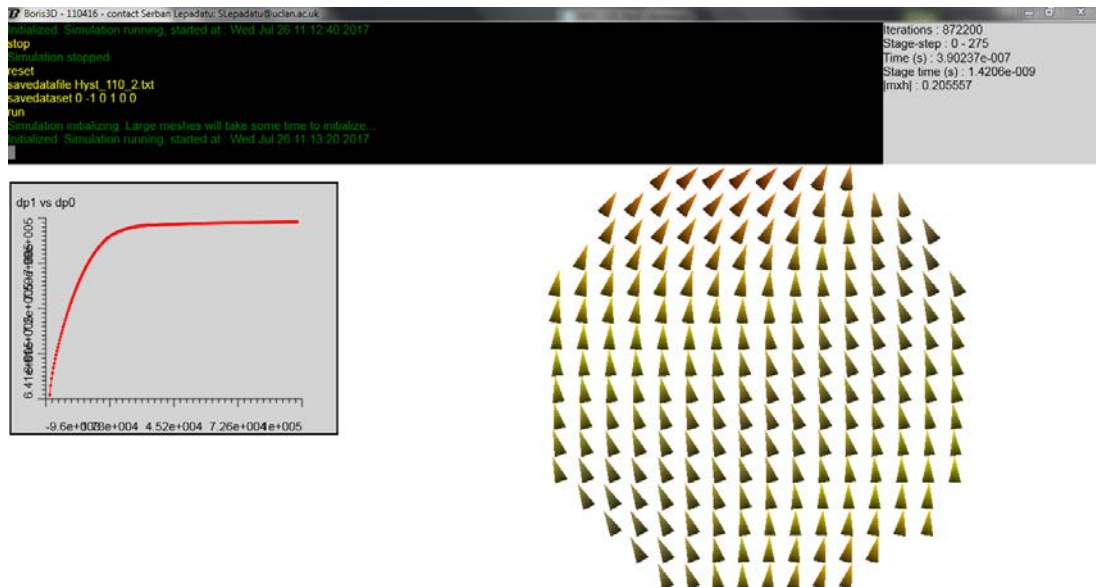


Figure 43 - Boris micromagnetic package during a hysteresis simulation on a NFO\_110 disc. The command line is shown top-left with a real-time display of the magnetisation bottom-right.

interactions include: Demagnetising fields, exchange interactions, Zeeman and uniaxial and cubic anisotropy, to name but a few.

Boris operates by using a finite difference method to solve the LLG equation. Each effective field (except the applied field) is derived through energy equations as follows.

The demagnetising field,  $\mathbf{H}_d$  involves interactions between every cell. As such it is the most computationally expensive field to determine. This is due to it being expressed as the convolution of the magnetisation and the demagnetising tensor:

$$\mathbf{H}_d(\mathbf{r}_0) = - \int_{\text{rev}} \mathbf{N}(\mathbf{r} - \mathbf{r}_0) \otimes \mathbf{M}(\mathbf{r}) d\mathbf{r} \quad (4-27)$$

Where  $\mathbf{N}$  is the demagnetising tensor determined by Newell *et al.* [72],  $\mathbf{M}$  the magnetisation and  $V$  the sample volume. To save computation time this is computed using the convolution theorem which means:

$$FT(\mathbf{N}(\mathbf{r} - \mathbf{r}_0) \otimes \mathbf{M}(\mathbf{r})) = FT(\mathbf{N}(\mathbf{r} - \mathbf{r}_0)) \times FT(\mathbf{M}(\mathbf{r}))$$

where  $FT()$  denotes the fourier transform of the function within the parentheses. In this way the demagnetising tensor only has to be calculated once and only the fourier transform of the current magnetisation state has to be evaluated during each iteration.

The direct exchange term ( $\mathbf{H}_{ex}$ ) is simply given by:

$$\mathbf{H}_{ex} = \frac{2A}{\mu_0 M_s} \nabla^2 \mathbf{m}$$

where  $A$  is the exchange stiffness. In Boris this is a user defined variable and varies by the material being simulated. For nickel ferrite this is approximately 12 pJ/m [73] this means the exchange length given by (4-23) is 4.89 nm and so the cell-size is chosen to be 5 nm.

Finally the anisotropy field ( $\mathbf{H}_k$ ) given by:

$$\begin{aligned} \mathbf{H}_k = & -\frac{2k_1}{\mu_0 M_s} (\mathbf{e}_1 \alpha_k [\beta_k^2 + \gamma_k^2] + \mathbf{e}_2 \beta_k [\alpha_k^2 + \gamma_k^2] \\ & + \mathbf{e}_3 \gamma_k [\alpha_k^2 + \beta_k^2]) \\ & - \frac{2k_1}{\mu_0 M_s} (\mathbf{e}_1 \alpha_k \beta_k^2 \gamma_k^2 + \mathbf{e}_2 \alpha_k^2 \beta_k \gamma_k^2 + \mathbf{e}_3 \alpha_k^2 \beta_k^2 \gamma_k) \end{aligned}$$

Where  $\mathbf{e}_1$  and  $\mathbf{e}_2$  are user defined anisotropy directions and  $\mathbf{e}_3$  is defined as  $\mathbf{e}_3 = \mathbf{e}_1 \times \mathbf{e}_2$ .  $\alpha_k$ ,  $\beta_k$  and  $\gamma_k$  are the scalar products of these anisotropy directions and the magnetic moment:

$$\alpha_k = \mathbf{e}_1 \cdot \mathbf{m},$$

$$\beta_k = \mathbf{e}_2 \cdot \mathbf{m},$$

And

$$\gamma_k = 1 - (\mathbf{e}_1 \cdot \mathbf{m})^2 - (\mathbf{e}_2 \cdot \mathbf{m})^2.$$

The sum of these four terms is used as the field term in the LLG, which is then solved using a the 2nd order Adams-Bashforth-Moulton method as detailed by Lepadatu *et al.* [74]

Our samples are modelled on a 64 x 64 x 1 cell mesh as a single crystal disc of approximately 0.3  $\mu\text{m}$  in diameter. This is significantly smaller than the 8 mm diameter of our polycrystalline samples, however a larger mesh size significantly increases the simulation time. Likewise it would be possible to apply a grain structure to the mesh to provide a closer simile of the real samples but we are interested in the magnetocrystalline anisotropy of the  $\text{NiFe}_2\text{O}_4$  discs.

To determine the crystallography of each different sample we define the two symmetry directions and the two anisotropy constants  $K_1$  and  $K_2$ . As the anisotropy constants are material-dependent they are the same for each sample with  $K_1 = -10,000 \text{ J/m}^3$  and  $K_2 = -1 \text{ J/m}^3$  [15]. The symmetry directions are defined by polar angle  $\theta$  and the azimuthal angle  $\phi$  as in Table 1. The third symmetry direction is then generated perpendicular to these defined two.

*Table 1 - Symmetry direction polar and azimuthal angles for NFO samples*

	NFO_100	NFO_110	NFO_111
$\theta_1$	$90^\circ$	$45^\circ$	$54.7^\circ$
$\phi_1$	$0^\circ$	$0^\circ$	$0^\circ$
$\theta_2$	$90^\circ$	$135^\circ$	$54.7^\circ$
$\phi_2$	$90^\circ$	$0^\circ$	$120^\circ$

#### 4.9. Hysteresis loop showing bulk NFO is magnetically hard

As ever the first step of magnetic characterisation is to consider the hysteresis loop of the samples. We model this by an applied field of  $8 \times 10^5$  A/m or approximately 1 T being reversed in the x-direction. We calculate the relaxed magnetisation every 1600 A/m and the results are plotted in Figure 44. In this case, the hysteresis loop shows coercivity of  $10^4$  A/m (0.01 T) and a squareness of 0.84. This is unlike what is seen in experiment where a similar coercivity is observed but with a significantly lower remanence. The high remanence seen here can be explained by a number of factors. We have modelled this sample as a uniform single crystal disc whereas the measured sample is a polycrystalline disc and so has a granular structure with exchange decoupled grains. Figure 45 shows an example simulation on a polycrystalline sample, in particular a  $1 \mu\text{m} \times 1 \mu\text{m}$

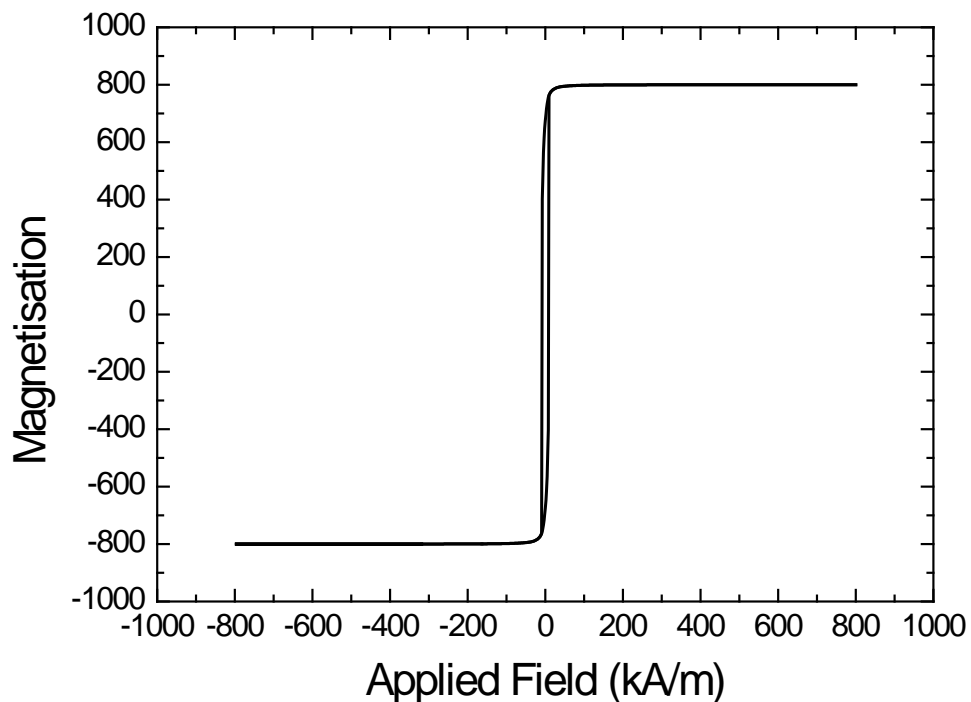
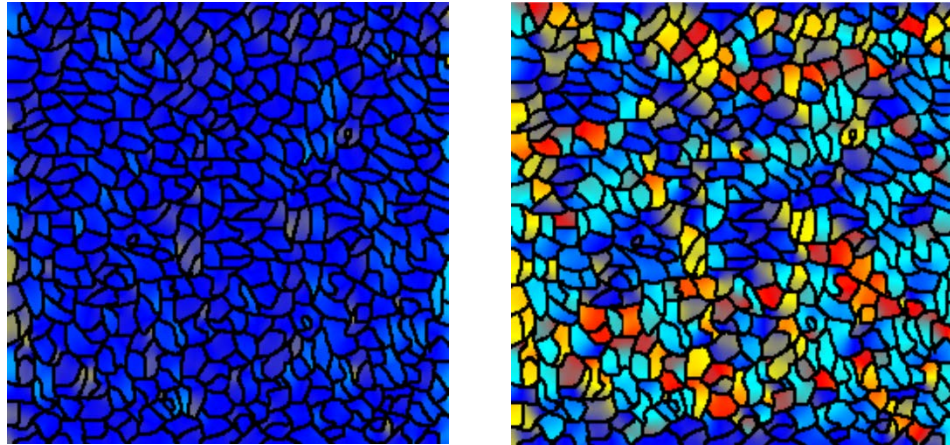


Figure 44 - Modelled Hysteresis curve for NFO\_110 sample



**(a)**

**(b)**

*Figure 45- Saturation (a) and Remanent (b) states in a simulated polycrystalline sample. The colour indicates the direction of magnetisation, with blue being left-aligned and red being right-aligned. In the saturated state the majority of grains are aligned in a single direction. When the field is removed the magnetisation of some grains rotates to be antiparallel with their neighbours due to long-range demagnetising effects.*

area. Initially saturated with all the grains magnetised to the left in a larger field, the sample is allowed to relax into a remanent state. As this occurs long range demagnetising effects can cause the magnetisation of some grains to rotate to be antiparallel resulting in a reduced remanence magnetisation.

The simulation scale is also much smaller than the actual sample and considerably thinner (i.e. thinner in proportion to its diameter) which would cause the out-of-plane demagnetising field to be larger [10]. Finally this curve is modelled at 0 K rather than room temperature, however comparing the thermal energy:

$$E_t = k_b T$$

where  $k_b$  is the Boltzmann constant and  $T$  the temperature and the magnetocrystalline anisotropy of a single grain:

$$E_k \approx k_1 V$$

where  $k_1$  is the first-order anisotropy constant and  $V$  the grain volume. By setting these values equal to each other we can estimate a grain volume below which thermal effects will begin to overcome the magnetocrystalline anisotropy. At room temperature this volume is

$$\begin{aligned} V &= \frac{k_b T}{k_1} = \frac{1.38 \times 10^{-23} \text{ m}^2 \text{ kg s}^{-2} \text{ K}^{-1} \times 293 \text{ K}}{10^4 \text{ Am}^{-1}} \\ &= 4 \times 10^{-25} \text{ m}^3 \end{aligned}$$

which corresponds to grains approximately 7 nm across. This is on the same scales as the exchange length in nickel ferrite and would therefore constitute an unrealistically fine grain structure.

#### **4.10. Torque Magnetometry.**

A field of  $1 \times 10^5 \text{ A/m}$  was rotated around the disc, allowing the magnetisation to relax at each step. At each step the magnetisation and the anisotropy energy in the field direction were calculated.

Figure 46 shows the magneto-crystalline anisotropy energy of the simulated NFO discs. The NFO\_100 and NFO\_110 discs have energy maxima of approximately 0 J, occurring in the NFO\_100 disc at 0°, 90°, 180°, 270°, 360° and in the NFO\_110 disc at 90° and 270°. These correspond to the magnetocrystalline hard axes and occur where expected for these crystal orientations.

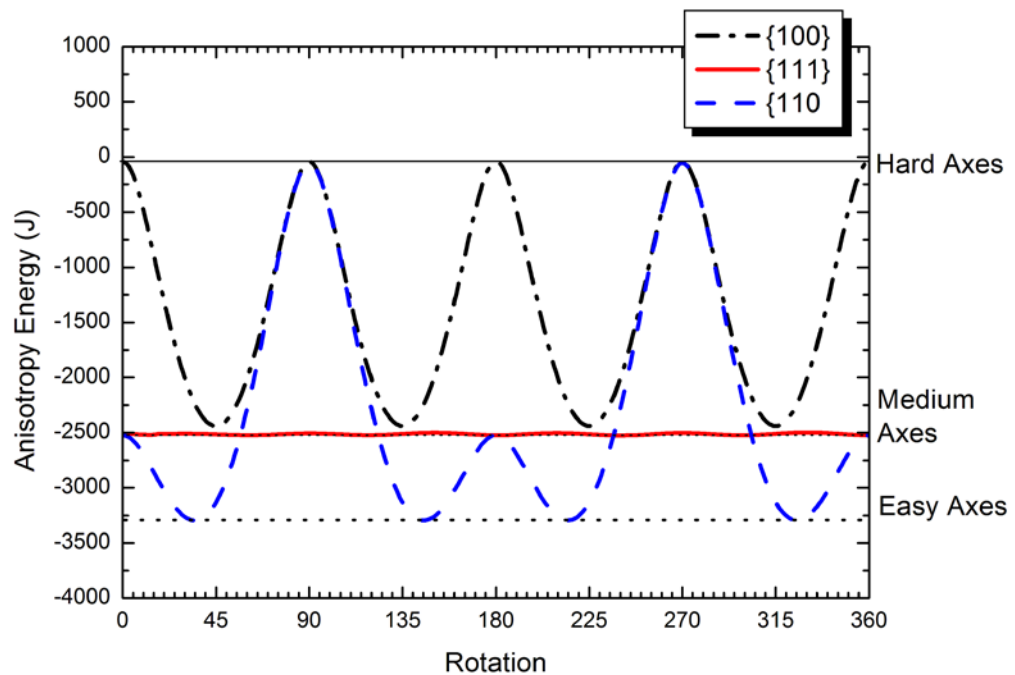


Figure 46 - Magnetocrystalline Anisotropy Energy of the three simulated NFO discs

The Energy minima in the NFO\_100 disc, approximately -2500 J occur at 45°, 135°, 225° and 315°, representing medium axes. The anisotropy energy of the NFO\_111 discs remains constant at about this level and the NFO\_110 has local maxima at 0°, 180 and 360°. Finally, the NFO\_110 has energy minima, -3250 J representing the easy axes directions, at 35°, 145°, 215° and 325°.

These results agree well with the expected anisotropy directions in the NFO samples and serves to demonstrate why the NFO\_111 sample can be described

as isotropic in the plane as the anisotropy energy of the disc is nearly constant as it is rotated. It is also clear that the medium axes are not “half-strength” hard axes with energy significantly lower than that of the hard axis directions.

With the current model, determining the expected torque curves from the micromagnetic behaviour of the samples is impossible. This is due to using the LLG equation which assumes local saturation of the magnetic moments. By using a model where this is not the case, such as by using the Landau-Lifshitz-Bloch equation, we could more accurately model the behaviour as the sample is rotated. It would also enable investigation into the “reducing field” torque magnetometry methodology as developed in chapter 3.

It would also be useful to include strain properties in this model, especially magnetostriction, to form a “Micro-magneto-mechanical model,” with the ultimate goal of producing a “Micro-magnetoelectric model.” Currently it is possible to apply a uniaxial anisotropy to simulate a uniform strain across the sample, but allowing individual cells to distort due to their magnetisation would require severe modification to the micromagnetic model. This could be achieved using a finite element model with strained tetragonal cells using a coupled micromagnetic and piezoelectric model.

## 5. Anisotropy measurements of the Magnetoelectric effect in $\text{NiFe}_2\text{O}_4/\text{PbZrTiO}_3$ bilayers

In this chapter we consider the magnetic and magnetoelectric properties of the NFO/PZT bilayer laminates as a function of sample rotation, with particular focus on the sample's behaviour when a principal crystallographic direction is aligned with the applied field.

The three samples, as described in chapter 2, are the NFO\_100, NFO\_110 and NFO\_111 designated by the miller indices of their crystallographic orientation. Due to this orientation we expect the NFO\_100 sample to exhibit biaxial behaviour with alternating medium and hard magnetocrystalline anisotropy axes. The NFO\_110 sample has a more complicated structure consisting of superposed uniaxial and biaxial components, resulting in a pattern of hard-easy-medium-easy axes as the sample is rotated, with the hard and medium axes perpendicular in the plane of the sample. Finally the NFO\_111 is expected to be isotropic in the plane.

We begin by discussing the magnetic properties of the samples with reference to the principal easy, medium and hard anisotropy directions before describing how the magnetoelectric coupling signal changes with respect to both applied field and sample rotation. Finally we introduce the “peak product” the product of the peak ME coupling signal and the optimum DC bias field, which is proportional to the saturation magnetostriction.

## 5.1. Magnetic Characterisation of Nickel Ferrite samples

Hysteresis curves were measured for all three NFO samples with the positive-field curves for NFO\_110 shown in Figure 47, which shows how the susceptibility changes with respect to the Easy (blue), Medium (red) and Hard (black) anisotropy axis that is in the field direction. The coercivity (<10 Oe) and remanence (<20%) agree well with measurements on polycrystalline NFO made by Iniguez *et al* [75]. The inset of Figure 47 shows the full major hysteresis loop for an easy direction in the NFO\_110 sample. As the coercivity and remanence is near zero for all directions, the “easiness” of a direction is apparent only in the larger susceptibility and smaller saturating field value. For example, starting with the field applied along an easy direction in the NFO\_110 sample, as the sample is rotated the susceptibility decreases until a medium direction is encountered. At this point the susceptibility increases back to the second easy

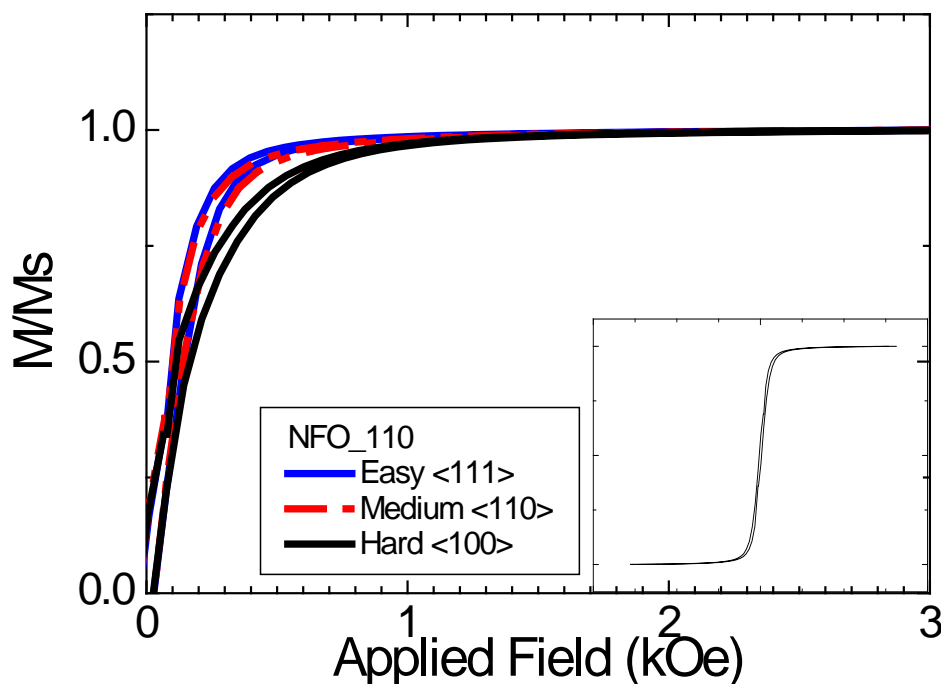


Figure 47 - Positive-field hysteresis loops along the three principle axes in the NFO\_110 sample. The inset is a full field hysteresis loop of an easy direction in the same sample. In all cases  $H_c = 10$  Oe

direction before decreasing even further to the hard direction. A large susceptibility causes the magnetisation to rapidly increase to the saturation value, so that there is a small saturating field required. Likewise, a low susceptibility needs a large field to reach saturation. This property is what leads to the variation in the in-field magnetisation used to derive the torque curves in the new methodology presented in chapter 3.

The other two samples follow this pattern, with the medium directions in the NFO\_100 having higher susceptibility and lower saturating fields than the hard directions and the susceptibility in the NFO\_111 remaining constant. This demonstrates that the variation measured in the torque curves in chapter 3, which suggests the NFO\_111 sample is {110}-like, is very small.

Although Nickel Ferrite as a bulk single crystal is magnetically hard with a large remanence, as shown in chapter 4, our samples are polycrystalline and flux closure mechanisms cause the net magnetisation to reduce to zero as the field reduces to zero. These mechanisms include thermal effects, small demagnetising field due to the large thickness of the samples and the grains being exchange decoupled.

## **5.2. Determination of the Magneto-Electric coupling as a function of sample rotation.**

As detailed in chapter 2, to generate a direct ME voltage signal requires the simultaneous application of two applied magnetic fields: a DC bias field,  $H_{DC-bias}$

and a small AC modulating field,  $H_{AC}$ . We begin by considering the effect of varying  $H_{DC-bias}$ . With a  $H_{AC}$  of constant amplitude of approximately 4 Oe,  $H_{DC}$  was varied between 1.5 kOe and 0 kOe with approximately 5 Oe increments. As the field is reduced from saturation the ME coupling response increases before reaching a maximum value at  $H_{DC-peak}$  and reducing to zero at zero field as shown in Figure 48.

In Figure 48 the ME coupling signal as a function of DC signal is shown for the three principle crystallographic directions in the NFO\_110 sample:  $\langle 111 \rangle$ ,  $\langle 110 \rangle$  and  $\langle 100 \rangle$ , which relate to easy, medium and hard magnetic anisotropy directions.

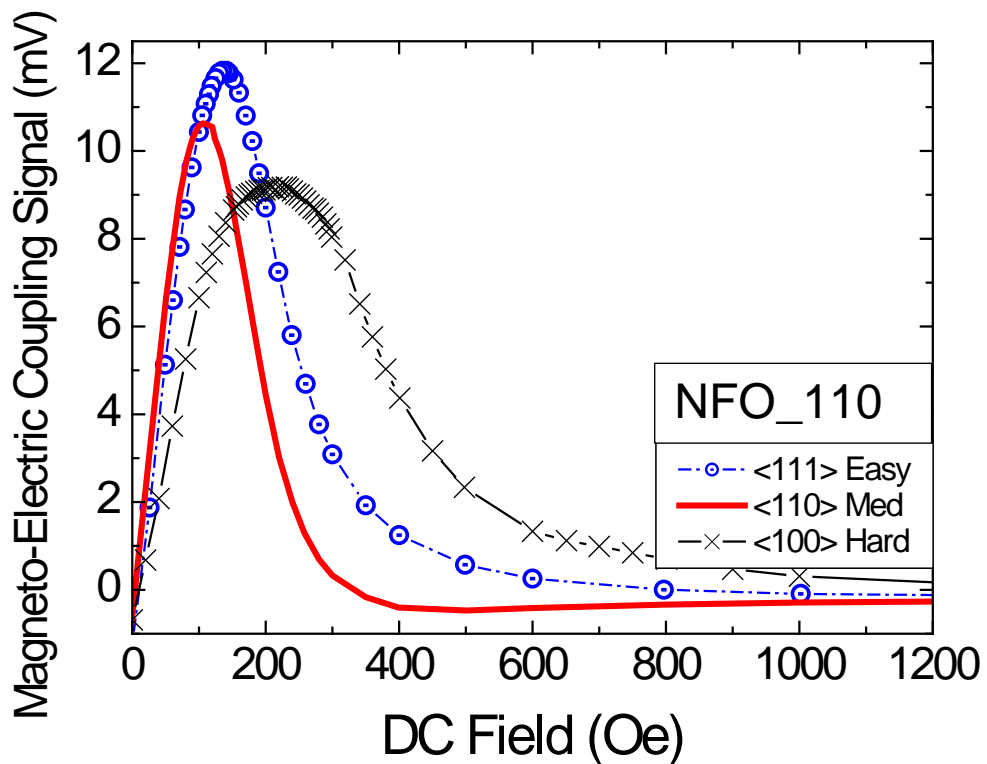


Figure 48 - Magneto-Electric coupling signal as a function of applied DC field in the NFO\_110 sample for the three principal crystallographic directions.

It can be seen that the maximum signal has a range of approximately 3 mV with the highest occurring along the easy direction and the lowest along the hard direction. It is also of note that the optimum field at which the peak occurs changes over a range of around 50 Oe. These preliminary results shows that the magneto-electric effect exhibits anisotropic behaviour in this sample.

Hence in any potential device the maximum (optimal) ME response is a function of both DC bias field and sample rotation. By plotting the position of this peak ( $H_{DC-bias}$ ) as a function of the sample rotation the effects of sample anisotropy due to the crystallographic texture on the optimal point are illustrated. This is shown for the NFO\_110 sample in Figure 50.

The highest peak field values occur with the field aligned along the Hard axis and the lowest along the Medium axis. The peak position follows a  $180^\circ$  repeating pattern suggesting a uniaxial anisotropy effect unlike the magnetic anisotropy of the sample. It can be seen that the range of fields is greater than that of the preliminary measurement, a range of approximately 90 Oe is shown.

The peak field has a consistent disagreement between positive and negative fields of approximately 10 Oe, which is caused by the offset described in Chapter 2. The fact that this offset is constant with respect to sample rotation supports the assumption that the offset is an experimental error and not due to the sample.

It also shows that the offset is isotropic and so does not affect the shape of the curves as a function of sample rotation.

Figure 49 shows how the peak amplitude of the ME coupling signal changes as the NFO\_110 sample is rotated, again measurements are shown for both positive and negative DC-bias fields. The positive field direction gives a systematic increase of approximately 1 mV compared to the negative field direction.

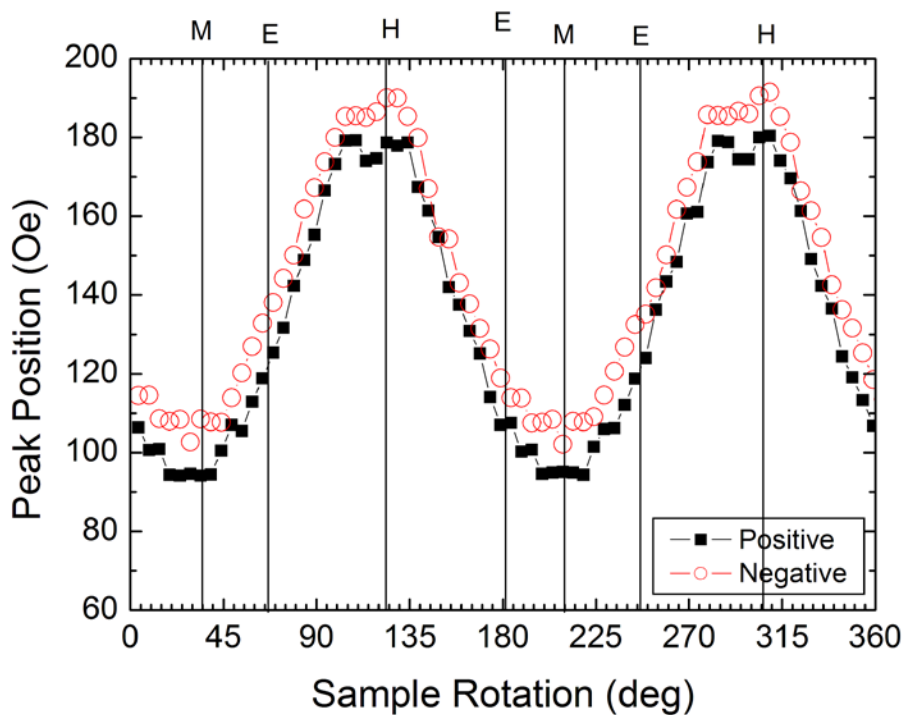


Figure 49 - Peak ME coupling as a function of sample rotation for the NFO\_110 sample..

The Peak signal varies by around 4 mV and although the pattern repeats with a period of 180° it is not as simple as the pattern of the peak field variation. The pattern is formed of two large minima at 110° and 290°, two small minima at 45° and 225°, two small maxima 80° and 255° and two large maxima at 160° and

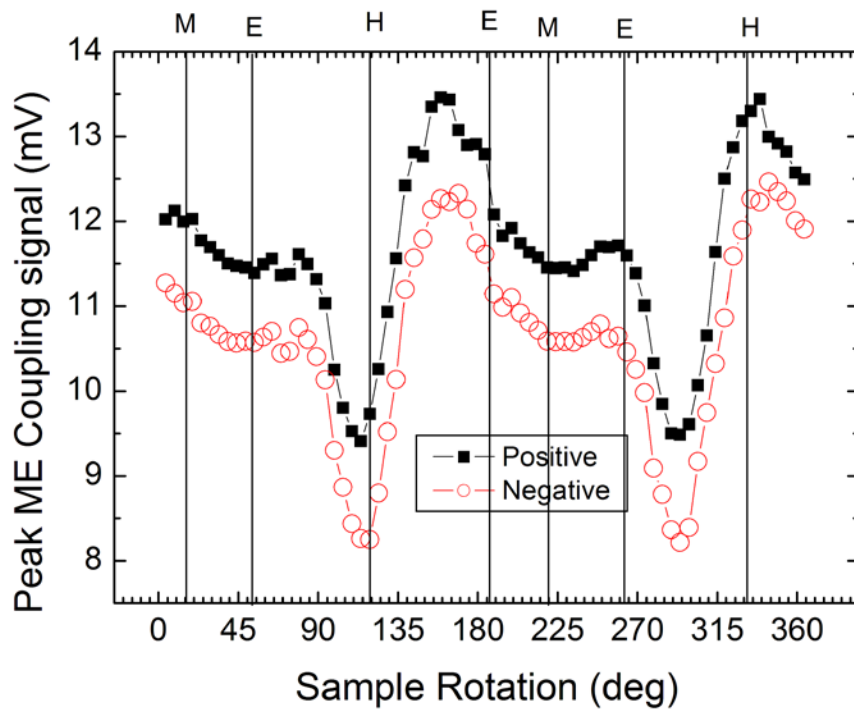


Figure 50 - Peak ME coupling as a function of sample rotation for the NFO\_110 sample. with an ac field of 4 Oe

340°. It is interesting to note that these have similar separation as the minima and maxima of the Torque curves as shown in Chapter 3 (Figure 37) this suggests a link between the peak coupling signal and the magnetocrystalline anisotropy energy, which defines the shape of the torque curves.

The shape of these graphs is easier to see when plotted as polar coordinates as in Figure 51, where the anisotropy directions determined from the torque curves are superimposed on the ME response. The value of a point on these graphs is determined by their distance from the centre of the graph, for example, the point corresponding to the peak field of the hard axis, which occurs at 120°, has a value of 190 Oe (as can be verified from Figure 50) and is displayed slightly inside the 200 Oe contour.

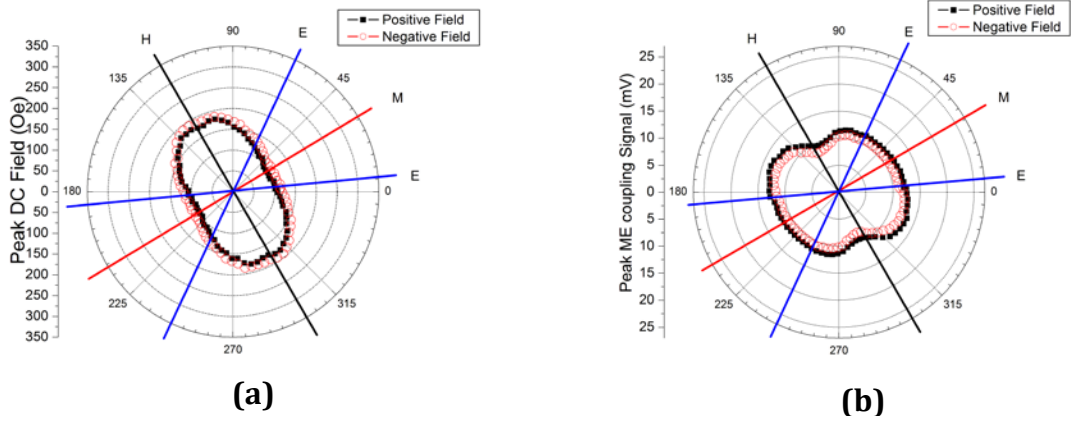


Figure 51 - Polar plots of the Peak DC field (a) and Peak ME coupling signal (b) for NFO\_110

### 5.3. The Effects of Magnetostriction

We assume for the moment the mechanical strain mediation and piezoelectric response is linear and one-to-one such that the magnetoelectric response will only be affected by the magnetostriction.

Although the precise manner by which a sample reaches its saturation magnetostriction is difficult to predict, there are some main features of the curve of  $\lambda$  as a function of  $H$ . In general  $\lambda$  will tend to  $\lambda_{si}$  the saturation magnetostriction at high fields and to reduce to zero at zero field. As  $\lambda$  is the magnetically induced strain, it is expected to be described by an even function, such that

$$\lambda(H) = \lambda(-H).$$

Finally this function is expected to be smooth, with no discontinuities in either the function or its derivative. Figure 52 is a schematic of such a function, in particular this theoretical magnetostrictive material fits an inverse Gaussian function defined as:

$$\lambda = \lambda_{si} \left( 1 - e^{-\frac{H_{DC}^2}{2w^2}} \right), \quad (5-1)$$

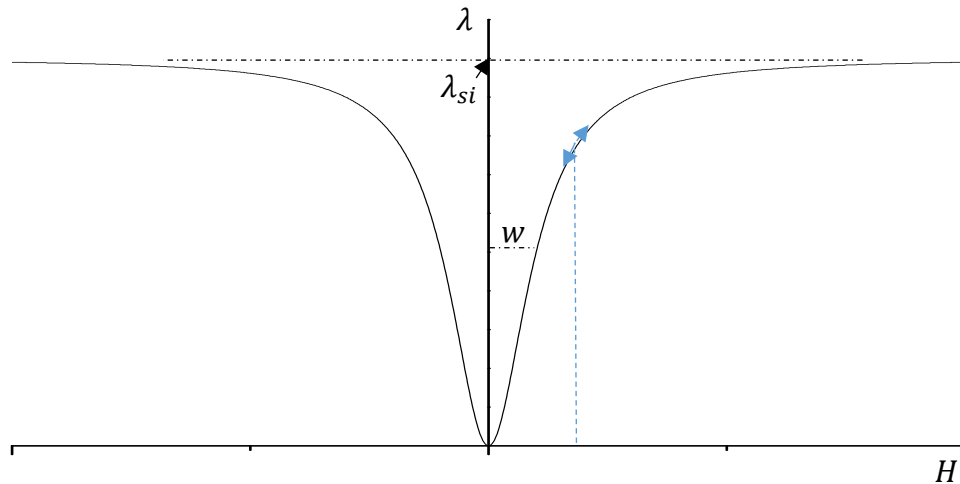


Figure 52 - Schematic representation of magnetostriction as a function of applied magnetic field.

where  $\lambda_{si}$  is the saturation magnetostriction and  $w$  defines the width of the Gaussian function. The theoretical values of  $\lambda_{si}$  for our samples were evaluated in Chapter 1 but the width (and actual shape) of the magnetostriction function depend on how domain walls move in the sample as it magnetises and so cannot be determined analytically.

When a DC and an AC magnetic field are applied to the sample simultaneously the measured AC voltage from the piezoelectric layer will be proportional to the derivative of the  $\lambda - H$  curve. The applied DC field selects a position on the curve and the small AC field perturbs the magnetostriction along the curve, pictured in Figure 52 as the small blue arrows.

Returning to the theoretical material of Figure 52, differentiating the function (5-1) yields:

$$V_{me} \propto \frac{d\lambda}{dH_{dc}} = \frac{\lambda_{si} H_{DC} e^{-\frac{H_{DC}^2}{2w^2}}}{w^2} \quad (5-2)$$

where  $V_{me}$  is the magnetoelectric coupling voltage. This function, as shown in Figure 53 has peaks at:

$$H_{peak} = \pm w = \pm k_1 w \quad (5-3)$$

Where  $k_1$  is a constant of proportionality dependent on the true shape of the magnetostriction function, and for the case when the magnetostriction can be described by a Gaussian function  $k_1 = 1$ .

The shape of Figure 53 closely resembles the measured ME coupling as shown in Figure 29 in Section 2.6.2

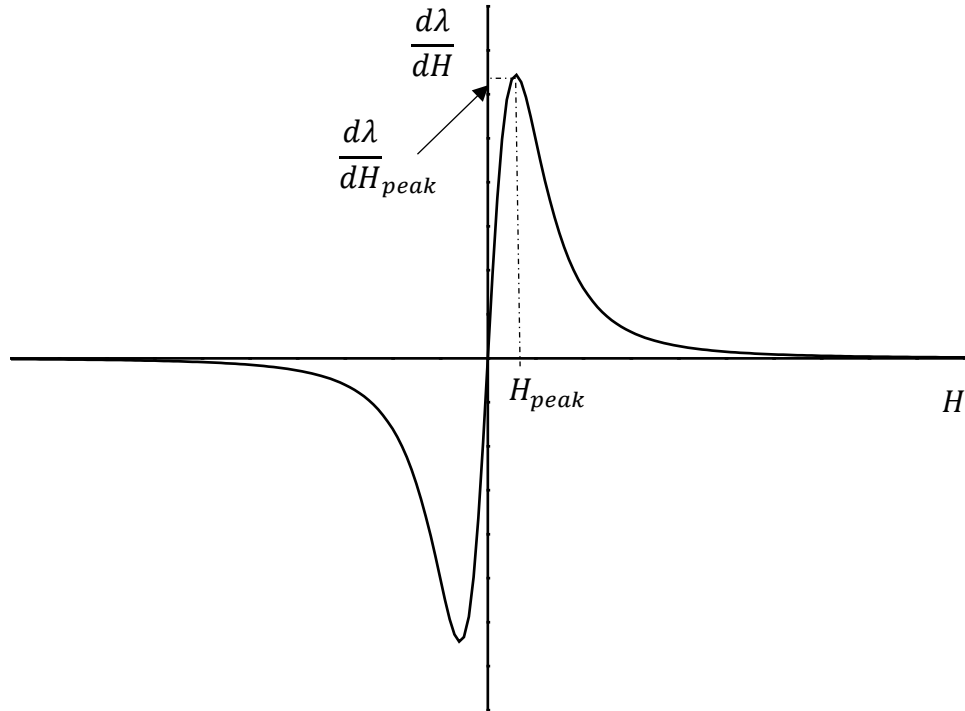


Figure 53 - Schematic showing the derivative of the function in Figure 8. Of particular importance are the peak field  $H_{peak}$  and the peak height  $\frac{d\lambda}{dH_{peak}}$ .

By substituting this value into the equation of (5-2) we find the height of the peak as:

$$V_{me-peak} \propto \frac{d\lambda}{dH_{peak}} = \frac{\lambda_{si}\sqrt{e}}{w}, \quad (5-4)$$

and so:

$$V_{me-peak} = k_2 \frac{\lambda_{si}}{w} \quad (5-5)$$

where  $k_2$  is a second constant of proportionality dependent on the shape of the magnetostriction function. Expressing these as proportionalities gives:

$$H_{peak} \propto w \quad (5-6)$$

And

$$V_{me-peak} \propto \frac{\lambda_{si}}{w}. \quad (5-7)$$

This means that the measured peak field is related to the width of the magnetostriction function and the peak signal is related to both the saturation magnetostriction and the width of the function. Furthermore, the product of these two values will be proportional only to the saturation magnetostriction such that:

$$H_{peak}V_{peak} \propto \lambda_{si} \quad (5-8)$$

Or

$$H_{peak}V_{peak} = K\lambda_{si}, \quad (5-9)$$

Where K is some constant of proportionality,  $K = k_1k_2$ . This product will be referred to from here as the “peak product”. From the analytical model developed in Chapter 1 we know the saturation magnetostriction for cubic crystals is described by the two constant equation:

$$\lambda_{si} = \lambda_{100} + 3(\lambda_{111} - \lambda_{100})(\alpha_1^2\alpha_2^2 + \alpha_2^2\alpha_3^2 + \alpha_3^2\alpha_1^2)$$

and by substituting into (5-9) it is shown that:

$$H_{peak}V_{me-peak} = K\lambda_{100} + 3K(\lambda_{111} - \lambda_{100})(\alpha_1^2\alpha_2^2 + \alpha_2^2\alpha_3^2 + \alpha_3^2\alpha_1^2).$$

This can be simplified for discs in planes of the form {100}, {110} and {111} as shown in Chapter 1 so that for the {100} disc we get:

$$H_{peak}V_{me-peak} = K\lambda_{100} + \frac{3k}{4}(\lambda_{111} - \lambda_{100}) \sin^2 2\psi,$$

for the {110}:

$$H_{peak}V_{me-peak} = K\lambda_{100} + \frac{3k}{4}(\lambda_{111} - \lambda_{100}) (\sin^4 \psi + \sin^2 2\psi),$$

and for the {111}:

$$H_{peak}V_{me-peak} = \frac{K(\lambda_{100} + 3\lambda_{111})}{4}.$$

This means the experimental data can be fitted to with these functions using  $K$ ,  $\lambda_{100}$  and  $\lambda_{111}$  as fitting parameters. The values for  $\lambda_{100}$  and  $\lambda_{111}$  are constrained to within  $\pm 5\%$  of those measured by Smith and Jones for nickel ferrite [15].

The results of applying this methodology to the NFO\_110 sample data are shown in Figure 54. The full ME coupling measurements for the NFO\_100 and NFO\_111 samples are shown in Figure 55 and Figure 56 which include the optimum bias field (a), the peak coupling signal (b) and the peak product (c) all as a function of sample rotation. In the case of the NFO\_100 sample of Figure 55, the anisotropy axes determined by torque magnetometry have been superimposed on the

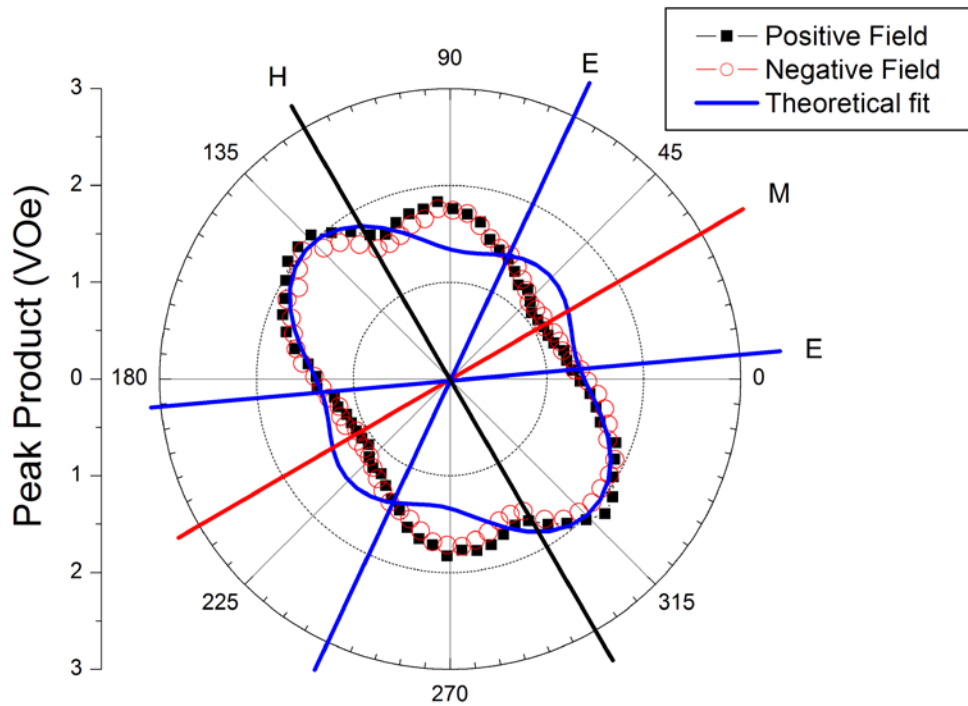


Figure 54 - The product of the DC ME peak height and field for the NFO\_110 sample for both positive and negative fields. The theoretical line is fit to the positive field curve.

figures. As the NFO\_111 sample is almost entirely isotropic in plane, Figure 56 is presented without anisotropy axes overlaid.

Looking at Figure 55 (a) the pattern of the optimum bias-field as a function of sample rotation repeats over  $90^\circ$  as expected for a biaxial system. Minima occur at approximately  $5^\circ$ ,  $105^\circ$ ,  $185^\circ$  and  $270^\circ$  which gives a separation of  $90^\circ$ . This is consistent with a biaxial system however the polar contour plot, appears to be “squared off.”

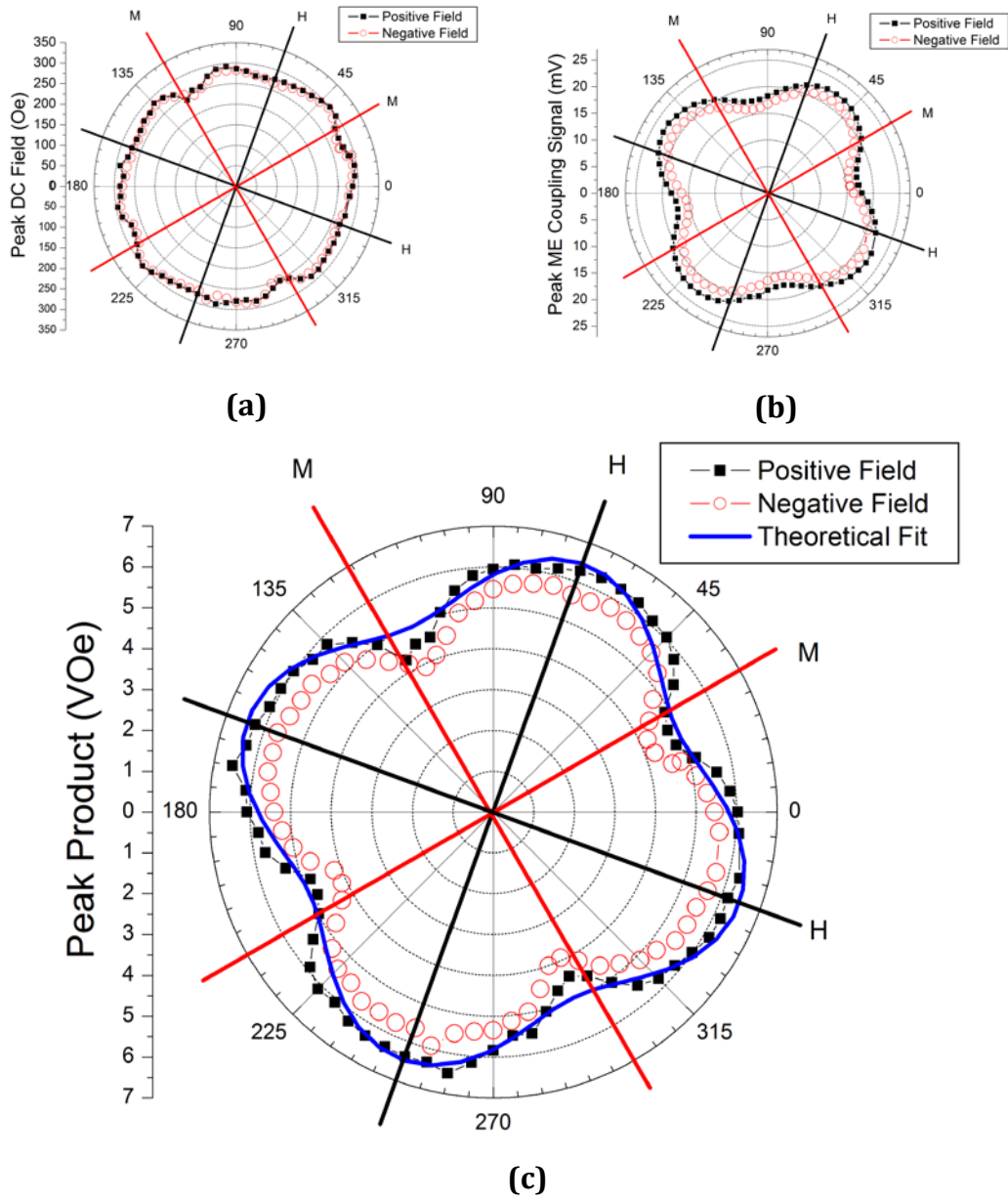


Figure 55 - Results for the NFO\_100 sample as a function of sample rotation:(a) The Optimum dc bias field, (b) the peak ME coupling signal and (c) The product of the DC ME peak height and field for the NFO\_100 sample for both positive and negative fields. The theoretical line is fit to the positive field curve.

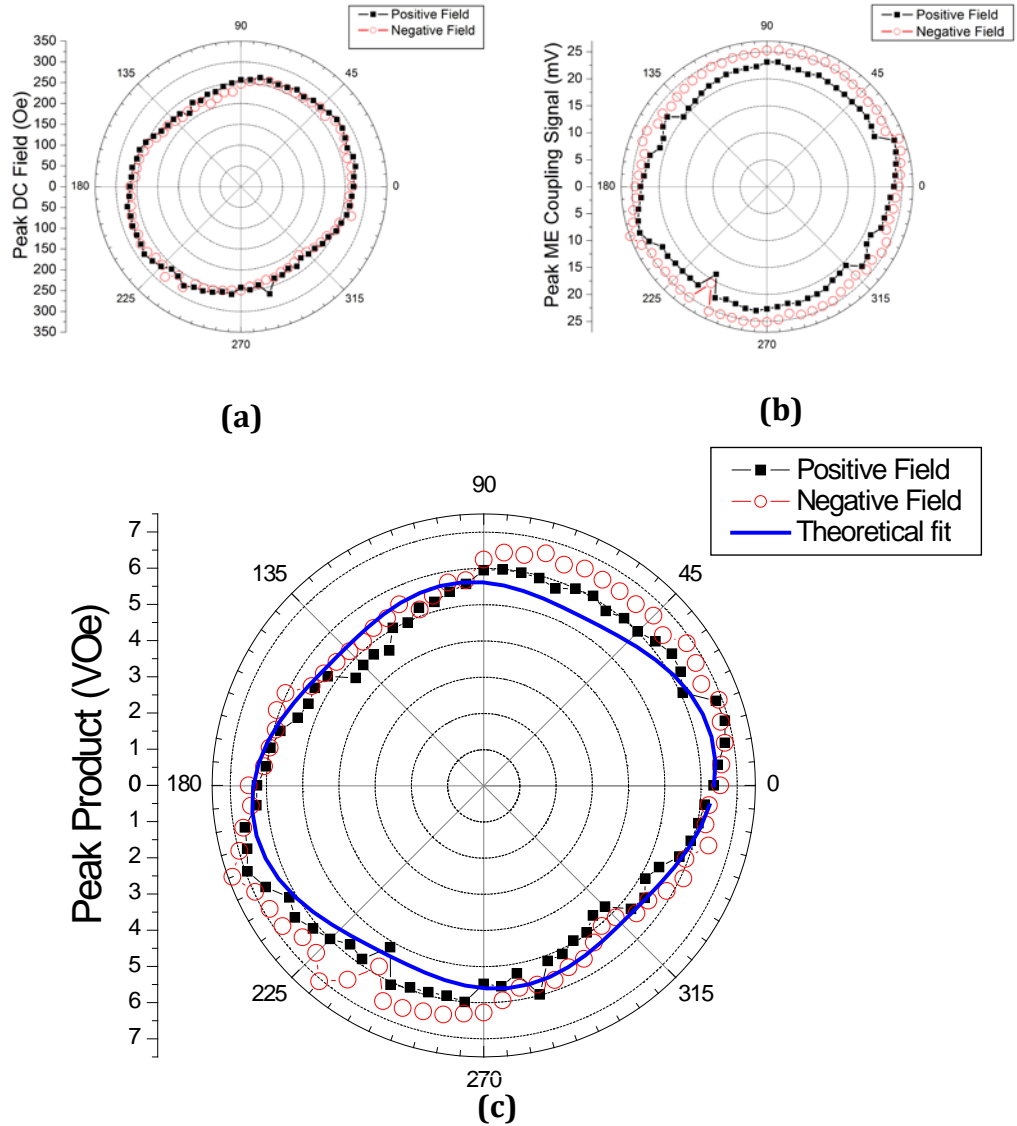


Figure 56 - Results for the NFO\_111 sample as a function of sample rotation: (a) The Optimum dc bias field, (b) the peak ME coupling signal and (c) The product of the DC ME peak height and field for the NFO\_100 sample for both positive and negative fields. The theoretical line is fit to the positive field curve.

Figure 55 (b) shows the Peak ME coupling signal for the NFO\_100 sample, this shows a distinct bi-axial relation with 4 minima and 4 maxima. The anisotropy directions of the crystal are between subsequent maxima and minima. As with the NFO\_110 sample, this reflects the shape of the torque curves. The peak product for the NFO\_100 sample as plotted in Figure 55 (c) when compared with theory agrees poorly ( $R^2 \approx 0.5$ ). However the overall shape of the curve and the position of the turning points with relation to the anisotropy axes compare well. It is interesting to note here that the turning points in the peak signal lie between

the anisotropy axes, but when multiplied by the optimum field, the turning points are shifted  $15^\circ$  so that they align with the anisotropy axes and the expected magnetostriction of the sample.

Returning to the NFO\_110 sample, the peak product in Figure 54 shows that the agreement for the NFO\_110 sample is significantly worse, with an  $R^2 = 0.36$ . However in general qualitative terms, the expected high peak product value is observed in the hard direction. The poor fit can possibly be explained by the fact that this sample was damaged and repaired, such that a crack runs along the hard axis. This crack leads to having two half-discs of nickel ferrite, such that when the applied field is applied perpendicular to the direction of the crack, a competing strain due to these halves separating appears in the piezoelectric layer and potentially reduces the magnetoelectric response in this direction. The theoretical fit also disagrees with the measured alignment of the magnetic anisotropy directions by  $15^\circ$ . This suggests that a mistake has been made in aligning the sample as it was transferred from the biaxial VSM where the torque magnetometry was performed to the ME measurement rig. If we assume that this is the case, the curve appears to follow the general trend that the Hard axis has the largest peak product and the Easy axes the smallest, if the reduction of the medium axis response due to the crack is accounted for. Ultimately this measurement needs to be repeated with a complete, unbroken NFO\_110 sample and additional care taken in maintaining the sample alignment between the two samples.

In the NFO\_111 case, as shown in Figure 56 (a) and (b), the peak field has a slight uniaxial behaviour and the Peak Coupling signal has little angle dependence as can be expected since this sample should be isotropic in plane. The peak product in Figure 56 (c) shows slightly uniaxial behaviour roughly along the  $45^{\circ}$ - $225^{\circ}$  axis, however the variation is very small with a standard deviation of approximately 11%. This supports the result from the torque curves shown in Chapter 3, which suggested a slight misalignment of the texture in the NFO\_111 sample causing a {110}-like response.

The poor quantitative agreement with the theory of all 3 samples can be attributed to the simplicity of the model. This model was developed under the assumption that the piezoelectric layer responds linearly and isotropically to in-plane strain and that the strain mediation is linear and one-to-one.

Currently, one of the main barriers to functionable magnetoelectric composites is the existence of the bias field [5] which limits the minimum device size [76]. It has been suggested that self-biasing can be used to achieve sizable ME coupling under an external AC magnetic field in the absence of a DC magnetic field. It is believed that by fully utilising the anisotropy of the magnetostriction and its effect on the ME coupling in combination with self-biasing composites it will be possible to produce highly magnetoelectric low-cost devices which require little to no bias-field.

#### 5.4. The Effect of Varying applied AC Field.

We now consider the effect of changing the AC field. For each measurement we set the dc-bias field to the peak value measured earlier. We then vary the AC field between 0 and 4 Oe rms at increments of 0.1 Oe.

Figure 57 shows the relation between the ME coupling signal and the applied AC field for the principal directions in the NFO\_110 sample. As we have a linear relation, we can define the magnetoelectric coupling coefficient as:

$$V_{ME} = \alpha H_{ac}$$

The medium axes shows distinct non-linearity at low fields. Recall that this is the cracked sample and that the medium axis in this sample is approximately perpendicular to the crack, such that the field is aligned across the crack. As such it is possible that at low AC fields opposing strains reduce the ME signal resulting in this non-linearity. This corresponds with the reduced peak product observed for fields applied along the medium axis, as in Figure 54. However further investigation into the precise influence of the crack on the magnetoelectric characteristics of the sample is still required.

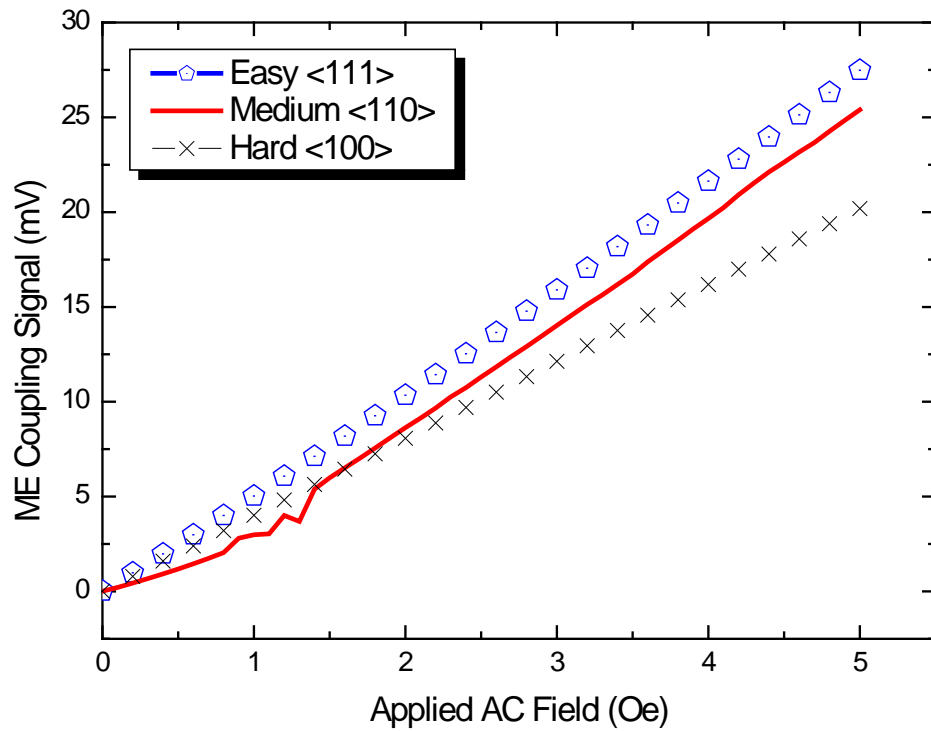


Figure 57 - Magnetolectric coupling as a function of applied AC field for the principal axes in the NFO\_110 sample

By repeating the measurements at intervals of  $4^\circ$  and fitting using a least-square method we obtain the ME coefficient as a function of sample rotation as shown in Figure 58. The anisotropic behaviour of  $\alpha$  mimics that of the ME peak signal. This is because of the linear relation between ME signal and applied AC-field, so as the ac field is varied the dc response curve will increase and decrease in height along with it.

This also occurs in the NFO\_100 sample as shown in Figure 59 (b). The in-plane isotropy of the NFO\_111 sample does not appear however the anisotropy of the magnetolectric coefficient is small compared to the other 2 samples, varying by  $<1 \text{ mV/Oe}$  compared to  $>2 \text{ mV/Oe}$ .

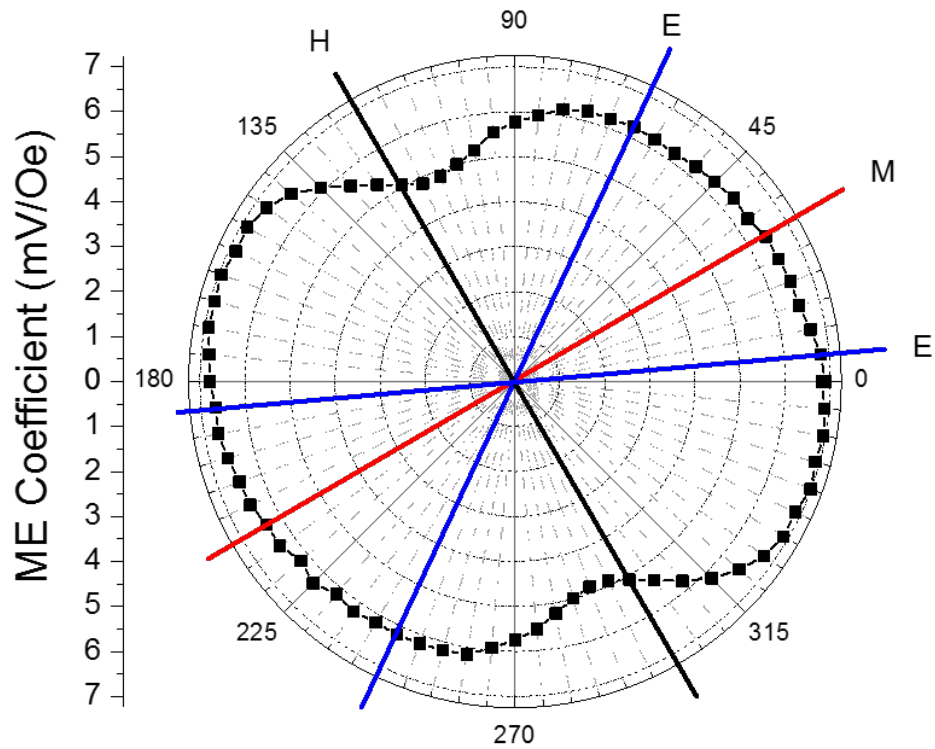


Figure 58 - ME coefficient as a function of angle for the NFO\_110 sample

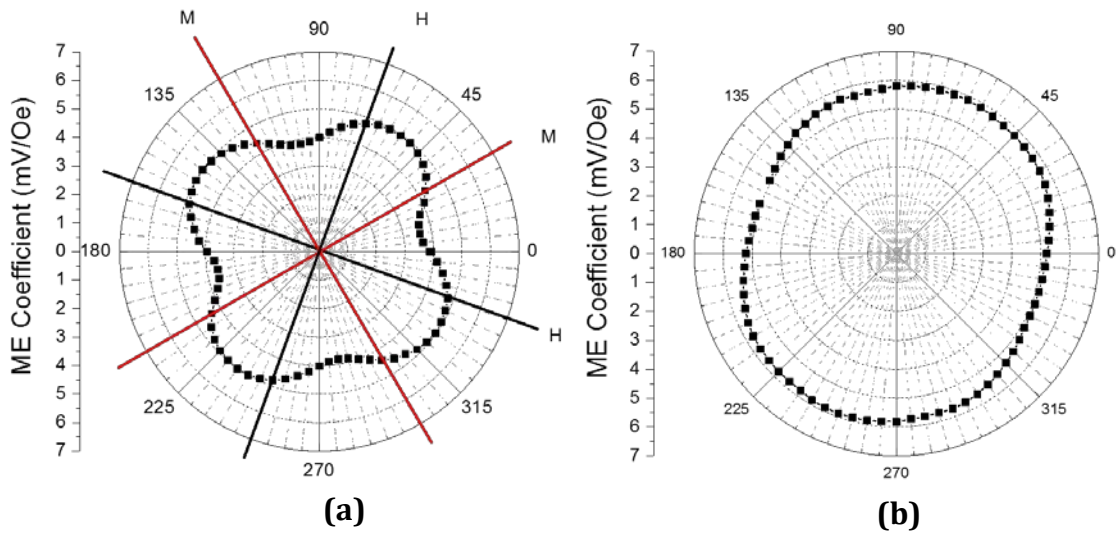


Figure 59 - ME Coefficient as a function of angle for the NFO\_100 (a) and NFO\_111 (b) samples

The fact that the maximum ME coupling does not occur at the same sample rotation angle as the minimum optimum bias field means that tuning a functional

device by using the anisotropy of the ME effect will require full consideration of the magnetoelectric response, for example in this case it appears that the medium axis in NFO is the best choice for low bias field and high ME coefficient as demonstrated in Figure 51 and Figure 55. However, the necessity for alignment with anisotropy directions of the magnetic layer corresponds to the large increase in piezoelectric response found in textured piezoelectric ceramics, which leads to highly magnetoelectric composites, as demonstrated by Yan *et al.* [2]. Therefore the combination of magnetic and piezoelectric texture is likely to lead to high-reponse tunable magnetoelectric devices.

In device design, tuning will depend on the requirements. For example if low bias-field should be required a minimum, such as alignment along a medium axis in Figure 55 (a) would be chosen. If maximum ME coupling was required a maximum in Figure 55 (b) would be chosen, such as the 55° alignment. In an optimised material both of these directions would be the same.

In some devices spatial directionality is important. Hence the peak product could provide a method of identifying viable materials for these devices.

## 6. Conclusions

The investigation described in this thesis demonstrates a strong anisotropy in the relationship between the magnetic, electrostatic and striction properties of the three samples investigated, both in terms of the direction of applied magnetic field in the sample plane and in the orientation of the crystal lattice to that plane due to induced texture. This has important implications in the design of transducers and other devices using multiferroic materials. By careful choice of crystal orientation and direction of measurement, it is possible to maximise the sensitivity of such devices. In addition, this study has shown that any device that requires a range of sensitivities may now be fabricated in one transducer, with the change in sensitivity brought about by a simple change of direction of the applied field. The key development of this work is shown in the main results of Chapter 5.

As part of the analysis in the main result chapter, the thesis describes the development of a peak product parameter proportional to the saturation magnetostriction of the material. This product provides an assessment of the viability of a magnetic material in terms of performance and tunability for its use as a multiferroic device. This will help in development of new multiferroic materials with enhanced properties.

The peak product parameter was developed from a phenomenological model of the magnetostriction of a material due to an applied magnetic field. It shows that the

product of the maximum magnetoelectric coupling and the dc-bias field at which this occurs is proportional to the saturation magnetostriction. In this way we have shown a direct connection between the magnetoelectric coupling strength and the bias field as well as linking them to the anisotropic properties of magnetic materials in a way that has not been studied before and which allows one parameter to be determined that describes the net effect of both the coupling and the bias field.

The samples studied are composites with specific crystallographic textures in their magnetic layers, one {100}, one {110} and one {111} and has thus enabled access to the full cubic magnetocrystalline anisotropy. As far as is known, no such study on the anisotropy of the magnetoelectric effect has been reported thus far.

During the course of this work, the knowledge required to understand existing/accepted techniques of measuring anisotropy via torque magnetometry techniques using a bi-axial VSM led to a new methodology being developed that optimises the measurement that is normally carried out at saturation magnetisation. By reducing the applied field in a series of steps to the optimal point, anisotropy features that would otherwise be missing (washed out) are observed and so effectively increases the sensitivity of the measurement. Furthermore, this investigation also led to a new method being developed to obtain an equivalent measurement using a “standard VSM”; that is a VSM with only a single set of pick-up coils parallel to the applied field direction. As many laboratories that do not have a bi-axial VSM are likely to have the simpler

standard VSM, this new method could be useful to other workers. There is also the potential that the new method may be more sensitive than the bi-axial method due to the torque tending to align the sample moment towards that of the measurement direction, but this requires further investigation. This work is detailed in Chapter 3.

The ME effect is the coupling between ferromagnetic and ferroelectric order parameters and results in magnetic-field-induced electric polarisation and electric-field-induced magnetisation. The ME effect has many applications such as magnetic sensors, current sensors, transformers, gyrators, energy harvesters, magnetic random access memory, and magnetic recording read heads. One of the main limiting factors for making functional ME devices is the requirement of a magnetic DC bias field to achieve large ME response, this work shows one possible method of tuning a device to have a lower optimum DC bias field in order to mitigate this problem.

In the samples studied the ME effect is strain mediated by a mechanical coupling between magnetostrictive and piezoelectric layers. This is a cheap and effective way of creating high response ME devices and is common practice in multiferroic studies.

In Chapter 2 the details of how a biaxial vibrating sample magnetometer (VSM) has been recommissioned and developed to enable precession reduction for

accurate measurements involving sample rotation, such as torque magnetometry. The VSM measures the change in magnetic flux in a series of pickup-coils due to a moving magnetised sample. In this chapter the sensitivity profiles of the pick-up coil systems are mapped out and compared with theoretical response. It is shown that the response of the pick-up coils is relatively insensitive to sample position in the centre of the coil systems and that the measured response agrees well with theory in this central area, however as the distance from the centre of the coil set increases the agreement gets worse. This is likely due to the exclusion of imaging effects due to the pole pieces of the applied field magnet which act to flatten the sensitivity profile.

The samples also needed to be rotated within the pick-up coils by a stepper motor and any misalignment in the rotation system causes the sample to precess. This was reduced by aligning the sample with the rotation axis in the x-y plane, effectively shifting the precession to another part of the machine so it does not affect the sample position. This method reduces the effects of precession such that they are negligible compared with the uncertainty of the pick-up response.

The modifications are tested by performing anisotropy measurements on known magnetic samples. The distribution of magnetic easy axes in a VHS tape sample was measured, with the symmetry of the result demonstrating the successful reduction of precession. These easy axis distribution methods were not suitable for the magnetically soft nickel ferrite samples and so to determine the alignment

of anisotropy directions in the samples torque magnetometry had to be employed.

Torque magnetometry is a powerful technique for probing the magnetic anisotropy characteristics of a material and can be simulated using the in-field perpendicular (transverse) component of magnetisation in a sample, as measured by a biaxial VSM. One of the main uses of torque magnetometry is identifying magnetic anisotropy directions in materials. In Chapter 3 a methodology is developed to make this process easier when performing the measurements on a biaxial vsm, where the transverse component of the magnetisation reduces to zero at large fields. This is done by repeat measurements at slowly decreasing fields, producing a repeating pattern of crossing points. At a certain field, lower than the material's saturating field the features of the torque curve become distinct and easily identifiable. When applied to our three samples this methodology identifies anisotropy directions consistent with the expected magnetocrystalline anisotropy in nickel ferrite.

Also in Chapter 3, a method by which torque magnetometry can be performed using a standard VSM is developed, in which only the in-field direction (parallel) component is measured. This enables anisotropy directions in magnetically soft materials to be easily identified in laboratories which do not have access to torque magnetometers or biaxial VSMs.

Chapter 4 details the micromagnetic model used to simulate the hysteresis loops and magnetocrystalline anisotropy energy of the nickel ferrite samples. This model uses the Landau-Lifshitz-Gilbert (LLG) equation to determine the magnetisation dynamics of the sample. Internal and external interactions with the magnetic moments in the material are represented by “effective” magnetic fields including the Applied field, demagnetising field, exchange field and the magnetocrystalline anisotropy field.

The simulation results shown in Chapter 4, where the anisotropy energy was obtained as a function of sample rotation, indicate the position of the easy, medium and hard axes for the three different crystal orientations, {100}, {110} and {111}. These results corroborate the torque curves obtained from VSM measurements, shown in Chapter 3, giving a degree of confidence in the experimental results and helping to characterize the principal characteristics of the angular variation indicated by the torque curves, namely the position of the principal magnetocrystalline anisotropy axes of symmetry. The simulation results thus further help in interpreting the angular dependence, due to anisotropy, of the magnetoelectric effect.

This model is not sufficiently advanced to fully reproduce all of the features of the torque magnetometry measurements shown in chapter 3 due to representing the samples as single crystals at 0 K. Thermal effects could be introduced to the model by using the Landau-Lifshitz-Bloch (LLB) equation in place of the LLG.

The simulation is also used to simulate an M-H curve accurately reproducing the coercivity values seen in experiment, which also compares well with literature values. The remanence in the model is significantly greater than in experiment, due to incorrect representation of the grain structure of the real sample. This could be improved by using a larger and more complex simulated sample. This would however greatly increase computation time.

Another limitation of the current model is the lack of real-time strain effects. An applied strain can be represented by an effective field, but the deformation caused by the rotation of magnetic moments, which is the cause of magnetostriction, can not be represented. It is proposed that a micro-magnetomechanical model be developed with the aim of combining it with ferroelectric modelling techniques to produce a full micro-magnetolectric model.

The main study of the anisotropy of the magnetoelectric effect is presented in Chapter 5 and it is here that the peak product parameter is developed and discussed. This chapter begins with the hysteresis loops of the polycrystalline nickel ferrite, which compare well with literature. We then go on to present the ME coupling as a function of sample rotation, focussing first on the effect of varying the applied DC magnetic bias field. This results in a distinct peak in the ME coupling signal, described by the optimum field ( $H_{DC-peak}$ ) and the maximum

ME coupling signal ( $V_{me-peak}$ ). It is shown, by comparison to a phenomenological model, that the product of these two values is proportional to the saturation magnetostriction, which can be determined theoretically. When this “Peak Product” is compared with the theoretical magnetostriction good agreement with the shape for the NFO\_100 sample is shown, with a biaxial response aligned with the magnetic anisotropy axes as expected. There is significant disagreement quantitatively but the model used assumes a linear and one-to-one coupling with the piezoelectric layer, which is unlikely to be true in the experimental samples.

The NFO\_111 sample, expected to be isotropic, shows little variation in the peak product. There is a slight uniaxial anisotropy in the peak product of the NFO\_111 sample suggesting a slight misalignment of the crystallographic. The agreement of the measured response in the NFO\_110 sample to theory is significantly worse than in the other two samples. This is most likely due to damage to the sample, which acts to reduce the magnetostriction in the direction of the medium axis of the sample.

These results show that it is possible to utilise the crystallographic texture of a material to tune the ME coupling response of devices. In particular it is possible to reduce the optimum bias field while maintaining a high maximum ME coupling. Combining this with self-biased ME composites may lead to functional, high response ME devices that require no bias field. It is important to note however, that due to inherent connection between the saturation magnetostriction and the optimum bias field, as expressed by the peak field

parameter, using materials with larger saturation magnetostriction may have detrimental effects when pursuing low-bias fields.

The presence of the damaged sample is unfortunate, further work in this area would have to focus on acquiring results from a complete set of 3 samples to help verify the “peak product” theory. In doing so, it is not necessary that nickel ferrite is used so a comparative material could be chosen. Ideally this material would have positive magnetostriction, so that it expands under the influence of a magnetic field, and positive magnetocrystalline anisotropy constants, which would mean that it exhibits  $\langle 100 \rangle$  easy axes instead of  $\langle 111 \rangle$ . It would also be useful to repeat similar ME measurements on textured thin films, as most of the applications for ME composites are being developed using thin films it is important to determine whether the effects presented here are still present at the micro-scale or if they become “swamped” by other contributions.

After this there are two possible directions in which this work could be advanced. The first is to investigate the combination of textured magnetic layers and textured piezoelectric layers in bilayer composites. For example, if a device utilises a uniaxial anisotropy of the piezoelectric layer to enhance its performance, there is little reason why a favourable alignment of the magnetic layer should not be utilised to further enhance the ME coupling.

The second avenue is to investigate the effect that a crystallographically textured magnetic layer has on the converse ME effect and the anisotropy of the converse magnetoelectric effect. This would be similar to work by Pertsev and Kohlstedt [9] wherein they utilise an electric-field-induced strain to alter the anisotropy energy of a biaxial magnetic layer to induce magnetisation switching.

## References

1. Ma, J., et al., *Recent Progress in Multiferroic Magnetolectric Composites: from Bulk to Thin Films*. *Advanced Materials*, 2011. **23**(9): p. 1062-1087.
2. Yan, Y.K., et al., *Giant energy density in 001 -textured Pb(Mg<sub>1/3</sub>Nb<sub>2/3</sub>)O<sub>3</sub>-3-PbZrO<sub>3</sub>-PbTiO<sub>3</sub> piezoelectric ceramics*. *Applied Physics Letters*, 2013. **102**(4).
3. Yang, Y.T., et al., *Electric field mediated non-volatile tuning magnetism in CoPt/PMN-PT heterostructure for magnetolectric memory devices*. *Journal of Applied Physics*, 2016. **119**(7).
4. Robisch, V., et al., *Pushing the detection limit of thin film magnetolectric heterostructures*. *Journal of Materials Research*, 2017. **32**(6): p. 1009-1019.
5. Palneedi, H., et al., *Status and Perspectives of Multiferroic Magnetolectric Composite Materials and Applications*. *Actuators*, 2016. **5**(1).
6. Fiebig, M., *Revival of the magnetolectric effect*. *Journal of Physics D-Applied Physics*, 2005. **38**(8): p. R123-R152.
7. Ryu, J., et al., *Magnetolectric properties in piezoelectric and magnetostrictive laminate composites*. *Japanese Journal of Applied Physics Part 1-Regular Papers Short Notes & Review Papers*, 2001. **40**(8): p. 4948-4951.
8. Cavill, S.A., et al., *Electrical control of magnetic reversal processes in magnetostrictive structures*. *Applied Physics Letters*, 2013. **102**(3).
9. Pertsev, N.A. and H. Kohlstedt, *Resistive switching via the converse magnetolectric effect in ferromagnetic multilayers on ferroelectric substrates*. *Nanotechnology*, 2010. **21**(47).
10. B.D., C. and G. C.D., *Introduction to Magnetic Materials*. 2nd ed. 2009: John Wiley & Sons Inc.
11. Mallinson, J.C., *The Foundations of Magnetic Recording*. 2nd ed. 1993: Academic Press Limited.
12. Goldman, A. and SpringerLink, *Modern ferrite technology*. 2nd ed. ed. 2005, New York, NY: Springer. -.
13. Perron, H., et al., *Structural investigation and electronic properties of the nickel ferrite NiFe<sub>2</sub>O<sub>4</sub>: a periodic density functional theory approach*. *Journal of Physics-Condensed Matter*, 2007. **19**(34).
14. Luders, U., et al., *Enhanced magnetic moment and conductive behavior in NiFe<sub>2</sub>O<sub>4</sub> spinel ultrathin films*. *Physical Review B*, 2005. **71**(13).

15. Smith, A.B. and R.V. Jones, *Magnetostriction in Nickel Ferrite and Cobalt—Nickel Ferrite*. Journal of Applied Physics, 1966. **37**(3): p. 1001-1002.
16. Jiles, D., *Introduction to Magnetism and Magnetic Materials*. 3rd ed. 2016.
17. Chikazumi, S., *Physics of Ferromagnetism*. 2nd Ed. ed. International series of monographs on physics. 1997: Oxford University Press.
18. Craik, D.J., *Magnetism: principles and applications*. 1995: Wiley.
19. Elliott, S.R., *The physics and chemistry of solids*. 1998, Chichester: Chichester : Wiley.
20. Kittel, C., *Introduction to Solid state Physics*. 8th ed. 2005: John Wiley & Sons.
21. Röntgen, W.C., *Ueber die durch Bewegung eines im homogenen elektrischen Felde befindlichen Dielectricums hervorgerufene electrodynamische Kraft*. Annalen der Physik, 1888. **271**(10): p. 264-270.
22. Astrov, D.N., *The Magnetoelectric Effect in Antiferromagnetics*. Soviet Physics, 1960. **11**(3).
23. Astrov, D.N., *Magnetoelectric Effect in Chromium Oxide*. Soviet Physics, 1961. **13**(4).
24. Folen, V.J.R.G.T.S., E W, *Anisotropy of the Magnetoelectric Effect in Cr2O3*. Physical Review Letters, 1961. **6**.
25. Rado, G.T.F., V J, *Observation of the Magnetically Induced Magnetoelectric Effect and Evidence for Antiferromagnetic Domains*. Physical Review Letters, 1961. **7**.
26. Tang, C.P. and C.J. Lu, *Strong self-biased magnetoelectric charge coupling in a homogenous laminate stack for magnetic sensor*. Journal of Alloys and Compounds, 2016. **686**: p. 723-726.
27. Lekha, C.S.C., et al., *High voltage generation from lead-free magnetoelectric coaxial nanotube arrays and their applications in nano energy harvesters*. Nanotechnology, 2017. **28**(5).
28. Kosub, T., et al., *Purely antiferromagnetic magnetoelectric random access memory*. Nature Communications, 2017. **8**.
29. Zhou, Y., C.H. Woo, and Y. Zheng, *Magneto-Electric Coupling in a Multiferroic Tunnel Junction Functioning as a Magnetic-Field-Effect Transistor*. IEEE Transactions on Nanotechnology, 2012. **11**(1): p. 77-81.
30. Fetisov, Y.K. and G. Srinivasan, *Electric field tuning characteristics of a ferrite-piezoelectric microwave resonator*. Applied Physics Letters, 2006. **88**(14).

31. Vopsaroiu, M., j. Blackburn, and M. Cain, *A new magnetic recording read head technology based on the magneto-electric effect*. Journal of Physics D-Applied Physics, 2007. **40**: p. 5027-5033.
32. Vopson, M.M., *Theory of giant-caloric effects in multiferroic materials*. Journal of Physics D-Applied Physics, 2013. **46**(34).
33. Tishin, A.M., et al., *A review and new perspectives for the magnetocaloric effect: New materials and local heating and cooling inside the human body*. International Journal of Refrigeration-Revue Internationale Du Froid, 2016. **68**: p. 177-186.
34. Lowman, C.E., *Magnetic recording*. 1972, New York ; (Maidenhead): New York ; Maidenhead : McGraw-Hill.
35. Vopson, M.M., *Fundamentals of Multiferroic Materials and Their Possible Applications*. Critical Reviews in Solid State and Materials Sciences, 2015. **40**(4): p. 223-250.
36. Kyung, C.M., *Nano Devices and Circuit Techniques for Low-Energy Applications and Energy Harvesting*. 2015: Springer Netherlands.
37. Ryu, J., et al., *Ubiquitous magneto-mechano-electric generator*. Energy & Environmental Science, 2015. **8**(8): p. 2402-2408.
38. Annapureddy, V., et al., *A pT/root Hz sensitivity ac magnetic field sensor based on magnetoelectric composites using low-loss piezoelectric single crystals*. Sensors and Actuators a-Physical, 2017. **260**: p. 206-211.
39. Gao, J.Q., et al., *Comparison of noise floor and sensitivity for different magnetoelectric laminates*. Journal of Applied Physics, 2010. **108**(8).
40. Li, M.H., et al., *Enhanced Sensitivity and Reduced Noise Floor in Magnetoelectric Laminate Sensors by an Improved Lamination Process*. Journal of the American Ceramic Society, 2011. **94**(11): p. 3738-3741.
41. Fang, C., et al., *Equivalent magnetic noise reduction at high frequency range due to polarized direction optimization in Terfenol-D/Pb(Mg<sub>1/3</sub>Nb<sub>2/3</sub>)O<sub>3</sub>-PbTiO<sub>3</sub> magnetoelectric laminate sensors*. Journal of Magnetism and Magnetic Materials, 2017. **423**: p. 106-110.
42. Thiele, C., et al., *Influence of strain on the magnetization and magnetoelectric effect in La(0.7)A(0.3)MnO(3)/PMN-PT(001) (A=Sr,Ca)*. Physical Review B, 2007. **75**(5).
43. Zhang, Y., et al., *Large reversible electric-voltage manipulation of magnetism in NiFe/BaTiO<sub>3</sub> heterostructures at room temperature*. Journal of Physics D-Applied Physics, 2010. **43**(8).

44. Li, Z., et al., *A simple method for direct observation of the converse magnetoelectric effect in magnetic/ferroelectric composite thin films*. Journal of Applied Physics, 2011. **110**(9).
45. Guo, Z., et al., *Electric field-induced multi-jump magnetic switching*. Journal of Alloys and Compounds, 2017. **703**: p. 431-436.
46. Han, Y.M., F. Wang, and K.L. Zhang, *A novel magnetoelectric memory cell based on bilayer ferroelectric films of (1-x) Ba(Zr<sub>0.2</sub>Ti<sub>0.8</sub>)O<sub>3</sub> - x(Ba<sub>0.7</sub>Ca<sub>0.3</sub>TiO<sub>3</sub>)*. Journal of Materials Science-Materials in Electronics, 2016. **27**(7): p. 7374-7378.
47. Han, Y.M., et al., *Electric Field Control of Magnetism in 0.7 Ba(Zr<sub>0.2</sub>Ti<sub>0.8</sub>)O<sub>3</sub> -0.3(Ba<sub>0.7</sub>Ca<sub>0.3</sub>TiO<sub>3</sub>)-Fe<sub>70</sub>Ga<sub>30</sub> Films*. Nanoscience and Nanotechnology Letters, 2016. **8**(9): p. 782-784.
48. Han, Y.M., et al., *Fabrication and characterization of a magnetoelectric memory cell of 50Ba(Zr<sub>0.2</sub>Ti<sub>0.8</sub>)O<sub>3</sub>-50Ba(0.7)Ca(0.3)TiO(3)/Fe<sub>70</sub>Ga<sub>30</sub>*. Materials Letters, 2016. **170**: p. 192-195.
49. Liu, Q., et al., *Study of mechanical-magnetic and electromagnetic properties of PZT/Ni film systems by a novel bulge technique*. Journal of Magnetism and Magnetic Materials, 2017. **423**: p. 90-97.
50. Peng, B., et al., *Deterministic Switching of Perpendicular Magnetic Anisotropy by Voltage Control of Spin Reorientation Transition in (Co/Pt)<sub>3</sub>/Pb(Mg<sub>1/3</sub>Nb<sub>2/3</sub>)O<sub>3</sub>-PbTiO<sub>3</sub> Multiferroic Heterostructures*. Acs Nano, 2017. **11**(4): p. 4337-4345.
51. Wang, Z.G., et al., *Magnetoelectric Assisted 180 degrees Magnetization Switching for Electric Field Addressable Writing in Magnetoresistive Random-Access Memory*. Acs Nano, 2014. **8**(8): p. 7793-7800.
52. Vopson, M., *Email Communication*. 2013.
53. Lisfi, A., et al., *The power of torque magnetometry: defect induced switching in hexaferrite nano-structures*. Nanotechnology, 2014. **25**(41).
54. Cornia, A., D. Gatteschi, and R. Sessoli, *New experimental techniques for magnetic anisotropy in molecular materials*. Coordination Chemistry Reviews, 2001. **219**: p. 573-604.
55. Sollis, P.M., et al., *EXPERIMENTAL AND THEORETICAL-STUDIES OF TRANSVERSE SUSCEPTIBILITY IN RECORDING MEDIA*. Ieee Transactions on Magnetics, 1992. **28**(5): p. 2695-2697.
56. Schmidlin, F., P.R. Bissell, and J.A. Gotaas, *Measurement of texture in magnetic recording media using a biaxial vibrating sample magnetometer*. Journal of Applied Physics, 1996. **79**(8): p. 4746-4748.

57. Sharrock, M.P., *ANISOTROPY AND SWITCHING BEHAVIOR OF RECORDING MEDIA - COMPARISON OF BARIUM FERRITE AND ACICULAR PARTICLES*. Ieee Transactions on Magnetics, 1990. **26**(1): p. 225-227.
58. Foner, S., *The vibrating sample magnetometer: Experiences of a volunteer*. Journal of Applied Physics, 1996. **79**(8): p. 4740-4745.
59. Bernards, J.P.C., *Design of A Detection Coil System for A Biaxial Vibrating Sample Magnetometer and Some Applications*. Review of Scientific Instruments, 1993. **64**(7): p. 1918-1930.
60. R.S. Tebble, D.J.C., *Magnetic Materials*. 1st ed. 1969: Wiley Interscience.
61. Bourn, S., et al., *Development of a Method to Identify in-Plane Anisotropy Axes in Soft Magnetic Materials Using a Standard Vibrating Sample Magnetometer*. Ieee Transactions on Magnetics, 2015. **51**(11).
62. Barandiaran, J.M., et al., *Distribution of the Magnetic-Anisotropy in Amorphous-Alloys Ribbons*. Ieee Transactions on Magnetics, 1989. **25**(5): p. 3330-3332.
63. Dubuget, V., et al., *Magnetic Anisotropy Dispersion With Exchange Energy in Soft Ferromagnetic Thin Films*. Ieee Transactions on Magnetics, 2010. **46**(5): p. 1139-1142.
64. Xue, D., X.L. Fan, and C.J. Jiang, *Method for analyzing the in-plane uniaxial anisotropy of soft magnetic thin film*. Applied Physics Letters, 2006. **89**(1).
65. Fan, X.L., et al., *An approach for researching uniaxial anisotropy magnet: Rotational magnetization*. Journal of Applied Physics, 2007. **102**(12).
66. Garcia, J., et al., *Magnetic anisotropy and magnetostriction in nanocrystalline Fe-Al alloys obtained by melt spinning technique*. Journal of Magnetism and Magnetic Materials, 2014. **372**: p. 27-32.
67. Brown, W.F., *Micromagnetics*. Interscience tracts on physics and astronomy. 1963: Interscience Publishers.
68. Odom, B., et al., *New measurement of the electron magnetic moment using a one-electron quantum cyclotron*. Physical Review Letters, 2006. **97**(3).
69. Gilbert, T.L., *A phenomenological theory of damping in ferromagnetic materials*. IEEE Transactions on Magnetics, 2004. **40**(6): p. 3443-3449.
70. Lepadatu, S., *Interaction of magnetization and heat dynamics for pulsed domain wall movement with Joule heating*. Journal of Applied Physics, 2016. **120**(16).
71. Craik, D., *Mangetism Principles and Applications*. 1995: John Wiley & Sons.

72. Newell, A.J., W. Williams, and D.J. Dunlop, *A GENERALIZATION OF THE DEMAGNETIZING TENSOR FOR NONUNIFORM MAGNETIZATION*. Journal of Geophysical Research-Solid Earth, 1993. **98**(B6): p. 9551-9555.
73. Dantas, C.C. and A.M. Gama, *Micromagnetic simulations of spinel ferrite particles*. Journal of Magnetism and Magnetic Materials, 2010. **322**(19): p. 2824-2833.
74. Lepadatu, S., et al., *Synthetic ferrimagnet nanowires with very low critical current density for coupled domain wall motion*. Scientific Reports, 2017. **7**.
75. Iniguez, J., C. Pereira, and J. Rivas, *EFFECT OF POROSITY ON THE MAGNETIC-BEHAVIOR OF NICKEL FERRITES*. Applied Physics a-Materials Science & Processing, 1985. **36**(3): p. 159-161.
76. Yao, H., Y. Shi, and Y.-W. Gao, *A mechanical-thermo-magneto model for self-biased magnetoelectric effect in laminated composite*. Journal of Magnetism and Magnetic Materials, 2016. **401**: p. 1046-1053.

## Appendix A

### Boris Commands and Example Script

The following is a list of example commands that help to illustrate how the Boris software is operated. The part in **bold** is the main command followed by any variables required for the command. Note that Boris is case sensitive and most commands are lower case.

**addstage** settingtype ...

This adds a simulation stage. Simulation stages may have sub-stages (steps), e.g. a field sequence. Stopping condition is the same for each step. Available stopping conditions:

mxh : normalized largest torque in the entire mesh (e.g. 1e-4 is typical)

iter : number of iterations

time : time in seconds

nostop : no stopping condition

**addmodule**

This adds a simulation module. Simulation modules typically correspond to effective field terms. The current set of modules can be displayed using the **listmodules** command.

**mesh** nx ny nz nx, ny  $\geq 2$ , nz  $\geq 1$  integers

Set mesh size in number of cells. Should enter values which are integer powers of 2 (nz = 1 is a special case, 2D simulation), otherwise the entered values will be increased to the next power of 2.

**savedatafile** [directory\]filename

Set file for saving data. If path included it will also set working directory.

**savedataset** startstage endstage savestages savesteps itersave timesave

Set data saving frequency for stages starting from startstage to endstage (-1 to apply to end of list). Set to save at end of each stage, at end of each step, at end of a number of iterations and/or fixed time interval.

**setk1** K1

Set K1 anisotropy constant in  $\text{J/m}^3$ .

**setk2** K2

Set K2 anisotropy constant in  $\text{J/m}^3$ .

**dp\_load** filename col1 arrcol1 ...

Load data columns from filename, set at least one pair of col, arrcol. Col is the column in the data file, arrcol is the internal array column. This ranges from 0 to 9.

**dp\_save** filename col1 ...

Save data processing arrays in given file. New file made, overwriting any previous file with same name. Enter at least 1 column number (array number). This ranges from 0 to 9.

**dp\_sequence** start end steps col

Generate a sequence of numbers from start to end in number of steps and store it in col.

Below is the script used to generate the hysteresis curve shown in Figure 44.

```
delstage 0
reset
addmodule anicubi
loadmesh circle_small 0
addstage Hxyz_seq 1e5 0 0 -1e5 0 0 100 mxh 2e-5
setk1 -10000 45 0
setk2 -1 135 0
savedatafile Hyst_110.txt
plotdata ha 0 0
plotdata avm 0 1
newplot 0 1
savedataset 0 -1 0 1 0 0
run
```

# Publication

# Development of a Method to Identify in-Plane Anisotropy Axes in Soft Magnetic Materials Using a Standard Vibrating Sample Magnetometer

Steven Bourn<sup>1</sup>, Tim Mercer<sup>1,3</sup>, Phil Bissell<sup>1</sup>, and Melvin Vopson<sup>2</sup>

<sup>1</sup>Jeremiah Horrocks Institute for Mathematics, Physics and Astronomy,  
University of Central Lancashire, Preston PR1 2HE, U.K.

<sup>2</sup>Faculty of Science, University of Portsmouth, Portsmouth PO1 3QL, U.K.

<sup>3</sup>Department of Physics, University of Liverpool, Liverpool, L69 7ZE, U.K.

**A method of identifying in-plane anisotropy axes in soft magnetic materials has been developed using an in-field-only measurement technique. The method is based on an extended bi-axial vibrating sample magnetometer (VSM) technique that simulates the torque on a sample; giving rise to equivalent torque curves that are comparable with those determined directly using a torque magnetometer. Testing of the new methodology was carried out on magnetically soft and multi-axial nickel ferrite textured films deposited with various crystal orientations. The results compare well with the accepted bi-axial VSM technique, identifying the same in-plane anisotropy directions and relative easy and hard axes from the in-field measurement alone. This means that these characteristics could be determined using a standard VSM measuring magnetization in the field direction as long as it is fitted with a rotating sample stage.**

**Index Terms**—Angular dependence, easy and hard axes, in-plane anisotropy axes directions, soft magnetic materials, torque magnetometry, vibrating sample magnetometry (VSM).

## I. INTRODUCTION

**K**NOWLEDGE of the anisotropic behavior of magnetic materials is important in the characterization of soft and hard materials and development of an understanding of their characteristics. For example, García *et al.* [1] have studied the relation of anisotropy to magnetostriction in nanocrystalline melt spun Fe–Al alloys before and after annealing. Provided the hard axis direction is known, Dubuget *et al.* [2] and Barandiaran *et al.* [3] have shown a method of characterizing the anisotropy field distribution by measurements along a sample's hard axis.

Torque magnetometry, which directly measures the couple acting on a sample generated by the magnetic field, is the traditional method of determining the magnetic anisotropic axes and the analysis is well documented in books and other literature [4] and is still in use [5]. An alternative is to simulate the torque on a sample using the in-field and perpendicular magnetization as a sample is rotated and measured using a bi-axial vibrating sample magnetometer (VSM). Although these magnetometers are now available in many laboratories, they are not universally available and many studies are still restricted to the in-field direction.

Torque measurements are especially useful in characterizing the in-plane easy and hard axes in soft magnetic samples. We have been using a bi-axial VSM to simulate the torque measurements and to identify the easy and hard axes of multi-axial textured magnetically soft nickel ferrite NiFe<sub>2</sub>O<sub>4</sub> films deposited with various crystal orientations, and by measuring the in-field and transverse magnetizations during rotation of the sample.

Manuscript received March 20, 2015; revised May 2, 2015; accepted May 11, 2015. Date of publication June 5, 2015; date of current version October 22, 2015. Corresponding author: T. Mercer (e-mail: tmercer1@uclan.ac.uk).

Digital Object Identifier 10.1109/TMAG.2015.2435365

During these studies, we have identified a relation between the in-field and transverse magnetizations involving a phase shift, which indicates that it is possible to determine the direction and type of in-plane anisotropy axes in these materials from the in-field magnetization alone. This means that these characteristics could be determined using a standard VSM (measuring magnetization in the field direction) providing a rotating sample stage is fitted to it. While Xue *et al.* [6] and Fan *et al.* [7] have developed rotational in-field methods, these are based on the theory of uniaxial anisotropy energy and require fitting of the theory to their experimental data in order to determine the parameters that include the axis type (easy or hard) and direction in their uniaxial samples. In contrast, our proposed method is not limited to uniaxial samples and only requires a simple and direct data analysis to obtain the axis type and direction on fully soft films that have closed magnetization loops along their easy axes.

In this paper, we describe our bi-axial VSM measurements on soft nickel ferrite samples and show the relation between in-field and transverse measurements and how the anisotropy axis types and directions can be determined from the in-field measurement alone. While we will continue to use bi-axial measurements, this analysis may be useful to researchers who only have in-field measurements available in their laboratories.

## II. EXPERIMENTAL METHODOLOGY

### A. Samples and Experimental Setup

Thick NiFe<sub>2</sub>O<sub>4</sub> (NFO) polycrystalline films of ~1.25 mm and with known crystallographic orientation [8] were used in this paper. The films had been textured along a favored direction so that a sample annotated as say NFO\_100 refers to orientation parallel to a plane of the form {100}. The samples had been fabricated as discs of diameter ~8 mm to ensure their

uniformity of shape (with respect to the applied field and pick-up coils of the VSM) as a function of angular rotation in the measurement plane.

Magnetic characterization was carried out using a University of Central Lancashire built in-house 10 kOe bi-axial VSM. It includes precision control of the sample position that is used to effectively eliminate any precession that could otherwise occur during sample rotation.

### B. Extending the Conventional Bi-Axial VSM Methodology in Order to Lessen the Effects of Saturation

In general, by consideration of the torque per unit volume,  $L = \mathbf{M} \times \mathbf{H}$ , experienced by a sample of magnetization  $\mathbf{M}$  in an applied field  $\mathbf{H}$  then a bi-axial VSM provides a convenient method for determination of the couple that would otherwise act on the sample in the conventional direct measurement technique. From the bi-axial geometry of the pick-up coils, with one set parallel to the in-field direction and the other transverse in the same measurement plane, then the component of  $\mathbf{M}$  in-field will generate zero torque and the general equation reduces to

$$L = M_{\perp} H \quad (1)$$

where  $M_{\perp}$  is the perpendicular magnetization obtained from the transverse coil set. Plotting this equivalent torque as a function of sample rotation simulates the torque curves obtained by direct measurement and is thereby an accepted method for the determination of anisotropy axes in magnetic materials.

A known limitation of the bi-axial method is that when maximum torque is achieved as a sample approaches saturation, then  $M_{\perp}$  is being reduced to a minimum (and tending to zero) due to nearly all of the vector sample moment  $\mathbf{m}$  being pulled into the applied field direction. In our study, on soft samples with saturation fields of about 1.5 kOe, we have been routinely using a modified methodology, whereby a series of simulated rotational torque curves has been generated at decreasing field steps. In each case, the sample is saturated while static and the field then reduced to a value lower than the previous step before rotation takes place. In this manner, a distinctive repeat pattern is observed as shown in Fig. 1 for the NFO\_100 sample.

Here, the sample was initially saturated at 10 kOe for each curve prior to rotation in the non-saturating range 0.6–0.2 kOe. From this, a series of common intercepts with the abscissa is observed, with the crossing points that have a positive gradient spaced 90° apart at 68°, 158°, 248°, and 338°, respectively. Likewise, a set of common crossing points with a negative gradient are also spaced 90° apart, starting at 23° and leading to alternate negative and positive gradient intercepts spaced 45° apart. This is consistent with one set of perpendicular bi-axial anisotropy easy axes orientated at 45° with respect to a second set of perpendicular bi-axial hard axes. The terms easy and hard refer to the relative strengths, in respect of either anisotropy energies or anisotropy fields, of these axes compared with one another. In this sense, one of the bi-axial sets can be thought of as being harder than the other set, or alternatively that one set is easier. It should be noted for

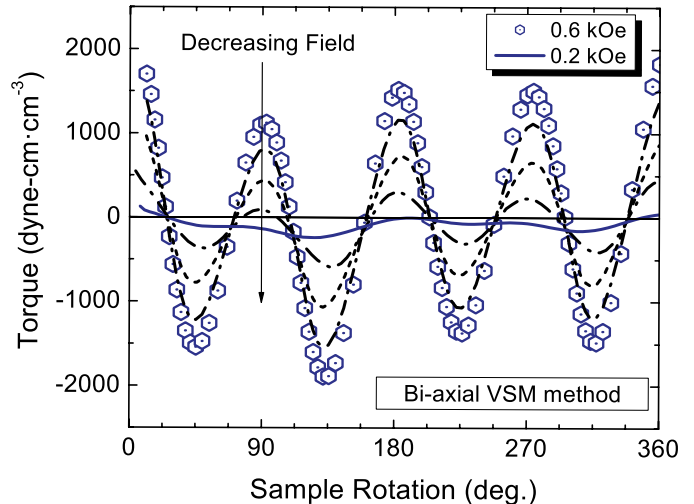


Fig. 1. Torque curves derived from the transverse magnetization of the NFO\_100 sample. The sample is initially saturated before the field is reduced to the required value. A measurement of the moment is made every 4°. The intercepts with the abscissa with positive and negative gradients indicate the hard and easy axes of the sample, respectively. Each axis is separated from the previous by approximately 45° as expected from the theory.

these soft materials, where the magnetization will tend to zero at small and decreasing fields, that the features in the torque curve flatten out and disappear as the torque also tends to zero. This can be observed in the 0.2 kOe curve of Fig. 1.

The results for the NFO\_100 sample of Fig. 1 compare well with other nickel ferrite samples measured by direct torque magnetometry [9] giving the expected easy and hard axes at the negative and positive gradient intercepts, respectively, and the subsequent bi-axial anisotropy in the  $\langle 111 \rangle$  easy directions and the  $\langle 100 \rangle$  hard directions expected for this orientation of a cubic crystal in the plane of the disk [10]. This gives confidence in our extended bi-axial VSM method and leads to the development of a technique for using the in-field magnetization alone.

## III. DEVELOPMENT AND TESTING OF THE METHODOLOGY FOR USING IN-FIELD MAGNETIZATION ONLY

### A. In-Field Methodology Development

Consider first a saturated sample in a large applied field that is significantly above the switching field distributions in any of the in-plane directions. If the sample is now rotated through a full 360°, the vector moment  $\mathbf{m}$  will always be switched along the in-field direction.

If the field is now reduced to some value below the upper limits of a switching field distribution and is rotated to an angle  $\theta$  with respect to the in-field direction, it will have a net vector moment that no longer lies parallel to the applied field. This is because  $\mathbf{m}$  now contains both switched and un-switched components instead and while the switched component will stay switched in-field, the un-switched component will rotate with the sample at  $\theta$  resulting in a net vector moment at an angle  $\phi$  to the parallel direction.

From simple trigonometry and the magnitude of the moment  $m$  we know that the transverse component of the moment measured in the transverse pick-up coil set of the

VSM is simply  $m_{\perp} = m \sin \phi$  and that the signal from the in-field coil set yields the parallel component  $m_{\parallel} = m \cos \phi$ . This suggests that it may be possible to derive the transverse moment needed for simulated torque curves from the in-field signal of a standard VSM, as

$$\frac{dm_{\parallel}}{d\phi} = -m \sin \phi = -m_{\perp}. \quad (2)$$

However, this is only applicable if the angle  $\phi$  is known.

If we now consider the effects of the decreasing field method on our mixed system of switched and un-switched components, it is convenient to think of this as a system of anisotropic particles with a distribution of switching fields that are aligned along the various anisotropic axes of the sample. Starting from the limit of saturation, when all the particles are switched under rotation into the parallel direction of  $\theta = \text{zero}$ , the reduction of applied field leads to an increase in the un-switched particles at the expense of the switched ones. As the un-switched particle moments are not held in the parallel direction, they begin to rotate with the sample, becoming ever more closely aligned with the sample rotation angle at each decreasing field step. The combination of the relative decrease in the parallel magnetization component at the same time as the increase in the rotational magnetization component means that the vector moment is now tending to the direction of  $\theta$  such that as  $\phi \rightarrow \theta$ , then (2) becomes valid as a means of simulating torque curves by differentiation of the parallel signal used in standard VSM instruments.

It should be noted that for measurements on soft materials with negligible hysteresis, the technique becomes limited at the small field end due to the drop toward zero of the magnetization signal in these samples at that point.

### B. Testing of the Methodology Using In-Field Rotation Curves

The results of applying the methodology to the in-field rotation curves of the NFO\_100 sample are shown in Fig. 2. The curves compare well with those of the bi-axial method of Fig. 1, reproducing all the essential features to show two sets of perpendicular bi-axial anisotropy directions  $45^{\circ}$  apart.

While these results are encouraging, a better test was provided using a NFO\_110 sample that has a more complex anisotropy. In this case, the sample was expected to have three sets of axes, with one set classed as relatively easy, the other medium, and the final set hard [10].

The in-field (parallel) curves of magnetization as a function of sample rotation are shown in Fig. 3 for the NFO\_110 disk. As such, they can be thought of as the raw data that could be obtained from a standard VSM fitted with an inexpensive rotational stage. Repeating patterns can be observed, such as the two troughs of approximately the same depth at  $158^{\circ}$  and  $338^{\circ}$ . The results of differentiating the curves of Fig. 3 are shown in Fig. 4, where they are displayed as data points to allow comparison with the lines of the bi-axial method that are also shown in the same plot. The two data sets compare well with the curves crossing the  $x$ -axis at the same points and with all the finer features of the bi-axial method, such as the relative amplitude of the peaks, apparently using the new methodology.

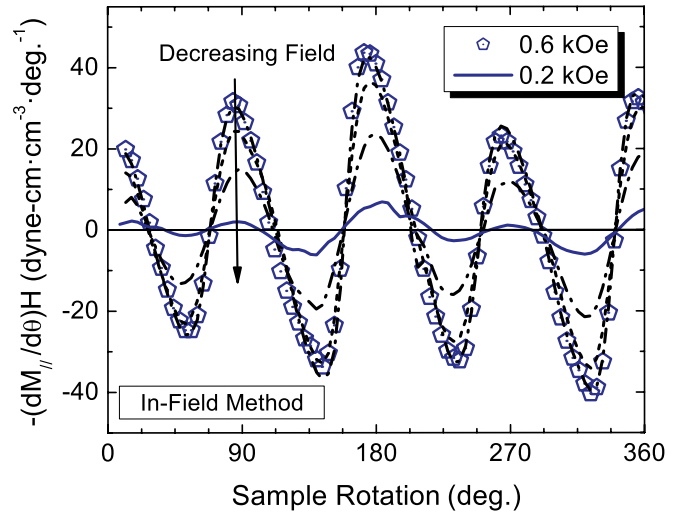


Fig. 2. Torque curves derived from the in-plane magnetization of the NFO\_100 showing good agreement with the bi-axial method of Fig. 1 for the position of the intercepts with the abscissa. This gives confidence in the new method as a means of identifying the hard and easy axes of a material. Note the loss of definition at small fields.

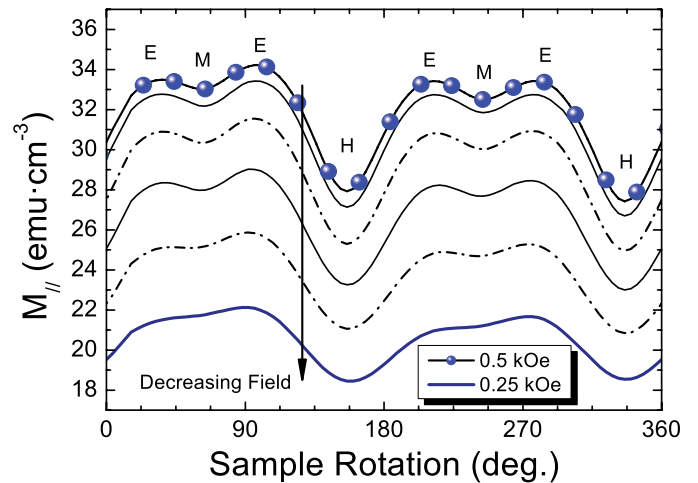


Fig. 3. In-field magnetization as a function of sample rotation for the NFO\_110 sample. The sample is initially saturated before the field is reduced to the required value. The turning points are labeled *E* for easy axis, *M* for medium axis, and *H* for hard axis.

Again, these crossing points show the positions of the anisotropy axes within the plane of the sample. In addition, inspection of the standard VSM data of Fig. 3 shows the means of classifying their relative hardness or easiness. This is due to the different saturating fields that occur at different sample orientations. For example, if the sample is orientated with an easy axis parallel to the applied field, it will have a lower saturating field than the same sample with its hard axis also rotated into the field direction. Hence, as our reducing field step methodology takes place below saturation, this ensures that for a given field, the easy axis magnetization is at a higher value than that of the harder axis. This is because the easy axis is closer to the saturation point at that field step when compared with that of the harder axis.

Application of this classification methodology to the data of Fig. 3 shows that the highest peaks (marked as *E*)

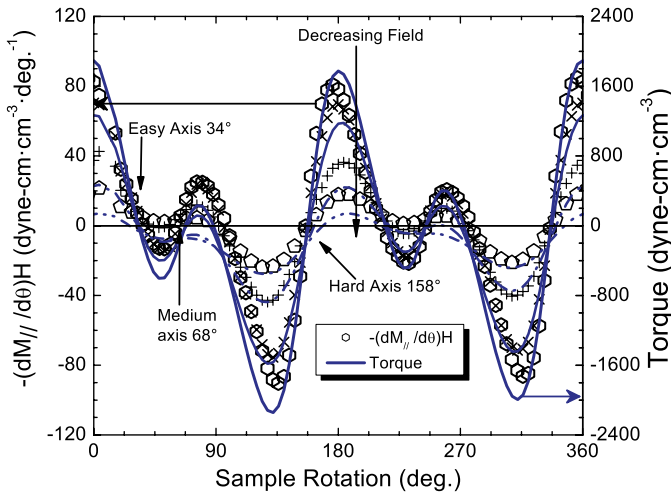


Fig. 4. Comparison of the in-field method (data points) with the bi-axial VSM (lines) for the NFO\_110 sample. The good agreement of the intercepts with the abscissa and the relative amplitude of the peaks gives confidence in the applicability of the new method.

occur at four crossing points of Fig. 4 at around  $34^\circ$ ,  $98^\circ$ ,  $210^\circ$ , and  $280^\circ$ , with just the first one marked easy to avoid clutter. It should be noted that the uncertainty in the positions is limited by the  $4^\circ$  resolution of the rotation steps used.

The first of two medium and two hard axes have also been identified in Fig. 4 from the respective set of intermediate and low moment turning points of Fig. 3 (marked as  $M$  and  $H$ , respectively). For a cubic crystal orientated parallel to the  $\{110\}$  plane, these axes can be mapped to the  $\langle 100 \rangle$ ,  $\langle 110 \rangle$ , and  $\langle 111 \rangle$  directions. Closer analysis of the anisotropy axes shows that the hard axes along  $\langle 100 \rangle$  and the medium axes along  $\langle 110 \rangle$  are spaced  $90^\circ$  apart, but that the easy axes at  $\langle 111 \rangle$  are not at  $45^\circ$  to either. This is consistent with an imperfect cubic lattice of slightly unequal lattice parameters that can sometimes be a result of strain in the texturing process of film growth.

It should be noted that a lower field-step increment of 40 Oe was needed for the NFO\_110 sample of Fig. 4 compared with the 100 Oe increment of the NFO\_100 sample of Fig. 2. This was expected due to the more complex anisotropy of the  $\{110\}$  plane that requires the vector moment direction to be as close as possible to the sample rotation in order to generate the equivalent transverse moment response of the bi-axial method. Simply reducing the field to lower values to increase the number of un-switched components starts to have a negative effect in soft materials because of the drop off of the magnetization signal toward zero at low fields. Hence, an optimum or sweet point using the new methodology needs to be found between these competing factors. Experimentally this was done by initially using the 100 Oe

field increments of the NFO\_100 sample over a wide range. This resulted in most of the curves being jagged and with no consistency in the, relative size, shape, and number of the peaks and troughs across the applied field range. The next step involved choosing the smoothest grouping of curves in the set that also had the most consistent features. For the NFO\_110 sample, this occurred between 500 and 300 Oe, with these values used to define a narrower field range and smaller field-step increments until all the curves were smooth and consistent in terms of features, as shown in Fig. 4.

A methodology has been developed that would allow the classification and direction of anisotropy axes in soft magnetic materials to be determined using the in-field measurements of a standard VSM fitted with a relatively simple and inexpensive rotational stage. In this manner, the technique reproduces the same simulated torque curves that are associated with more complicated and costly bi-axial VSM instruments.

#### ACKNOWLEDGMENT

The work of S. Bourn was supported by a Jeremiah Horrocks Institute studentship. The authors would like to thank Dr. S. Lepadatu of the Jeremiah Horrocks Institute for the useful discussions.

#### REFERENCES

- [1] J. A. García *et al.*, "Magnetic anisotropy and magnetostriction in nanocrystalline Fe-Al alloys obtained by melt spinning technique," *J. Magn. Mater.*, vol. 372, pp. 27–32, Dec. 2014.
- [2] V. Dubuget, S. Dubourg, P. Thibaudeau, and F. Duverger, "Magnetic anisotropy dispersion with exchange energy in soft ferromagnetic thin films," *IEEE Trans. Magn.*, vol. 46, no. 5, pp. 1139–1142, May 2010.
- [3] J. M. Barandiaran, M. Vazquez, A. Hernando, J. Gonzalez, and G. Rivero, "Distribution of the magnetic anisotropy in amorphous alloys ribbons," *IEEE Trans. Magn.*, vol. 25, no. 5, pp. 3330–3332, Sep. 1989.
- [4] B. D. Cullity and C. D. Graham, *Introduction to Magnetic Materials*, 2nd ed. New York, NY, USA: Wiley, 2009.
- [5] A. Lisfi, S. Pokharel, W. Morgan, G. Warren, and M. Wuttig, "The power of torque magnetometry: Defect induced switching in hexaferrite nano-structures," *Nanotechnology*, vol. 25, no. 41, 2014, Art. ID 415702.
- [6] D. Xue, X. Fan, and C. Jiang, "Method for analyzing the in-plane uniaxial anisotropy of soft magnetic thin film," *Appl. Phys. Lett.*, vol. 89, no. 1, 2006, Art. ID 011910.
- [7] X. Fan, D. Xue, C. Jiang, Y. Gong, and J. Li, "An approach for researching uniaxial anisotropy magnet: Rotational magnetization," *J. Appl. Phys.*, vol. 102, no. 12, 2007, Art. ID 123901.
- [8] M. Vopsaroiu, M. Stewart, T. Fry, M. Cain, and G. Srinivasan, "Tuning the magneto-electric effect of multiferroic composites via crystallographic texture," *IEEE Trans. Magn.*, vol. 44, no. 11, pp. 3017–3020, Nov. 2008.
- [9] A. I. Drokina, N. I. Sudakov, S. S. Gendeleev, E. M. Kondrat'ev, and L. I. Ryabinkina, "On the magnetocrystalline anisotropy of nickel-iron ferrites," *Soviet Phys. J.*, vol. 8, no. 5, pp. 109–114, 1965.
- [10] K. Yosida and M. Tachiki, "On the origin of the magnetic anisotropy energy of ferrites," *Prog. Theoretical Phys.*, vol. 17, no. 3, pp. 331–359, 1957.